PROCEEDINGS OF THE ANTENNA APPLICATIONS SYMPOSIUM HELD AT URBANA ILLINOIS ON 19-21 SEPTEMBER 1984 VOLUME 1(U) ILLINOIS UNIV AT URBANA SEP 84 RADC-TR-85-14-VOL-1 F/G 9/5 AD-8153 257 1/3 UNCLASSIFIED NL ė1----<u>-</u>-



MICROCOPY RESOLUTION TEST CHART NATIONAL BUREAU OF STANDARDS-1963-A

DTIC FILE COPY

RADC-TR-85-14, Vol I (of two) In-House Report January 1985



PROCEEDINGS OF THE 1984 ANTENNA APPLICATIONS SYMPOSIUM

Sponsored by
ELECTROMAGNETIC SCIENCES DIVISION
ROME AIR DEVELOPMENT CENTER
HANSCOM AFB, BEDFORD MASS. 01731
AIR FORCE SYSTEMS COMMAND

APPROVED FOR PUBLIC RELEASE: DISTRIBUTION UNLIMITED

ROME AIR DEVELOPMENT CENTER Air Force Systems Command Griffiss Air Force Base, NY 13441



This report has been reviewed by the RADC Public Affairs Office (PA) and is releasable to the National Technical Information Service (NTIS). At NTIS it will be releasable to the general public, including foreign nations.

RADC-TR-85-14, Volume I (of two) has been reviewed and is approved for publication.

APPROVED:

JOHN K. SCHINDLER

Chief, Antennas & RF Components Branch

Electromagnetic Sciences Division

APPROVED:

ALLAN C. SCHELL, Chief

Dela C. Schul

Electromagnetic Sciences Division

FOR THE COMMANDER:

JOHN A. RITZ
Acting Chief, Plans Office

If your address has changed or if you wish to be removed from the RADC mailing list, or if the addressee is no longer employed by your organization, please notify RADC (EEAA) Hanscom AFB MA 01731. This will assist us in maintaining a current mailing list.

Do not return copies of this report unless contractual obligations or notices on a specific document requires that it be returned.

SECURITY CLASSIFICATION OF THIS PAGE		/			
REPORT DOCUMENTATION PAGE					
18. REPORT SECURITY CLASSIFICATION Unclassified		1b. RESTRICTIVE MARKINGS			
28. SECURITY CLASSIFICATION AUTHORITY		3. DISTRIBUTION/AVAILABILITY OF REPORT Approved for public release:			
26. DECLASSIFICATION/DOWNGRADING SCHED	ULE		ion unlimited	•	
4. PERFORMING ORGANIZATION REPORT NUM	BER(S)	5. MONITORING ORGANIZATION REPORT NUMBER(S)			
RADC-TR-85-14 Volume I					
6a NAME OF PERFORMING ORGANIZATION	6b, OFFICE SYMBOL (If applicable)	78. NAME OF MONITORING ORGANIZATION			
Rome Air Development Center	EEA				
6c. ADDRESS (City, State and ZIP Code)		7b. ADDRESS (City, State and ZIP Code)			
Hanscom AFB Massachusetts 01731		<u> </u>			
86. NAME OF FUNDING/SPONSORING ORGANIZATION	8b. OFFICE SYMBOL (If applicable)	9. PROCUREMENT INSTRUMENT IDENTIFICATION NUMBER			
Rome Air Development Center	EEA	<u> </u>			
Sc. ADDRESS (City, State and ZIP Code)		10. SOURCE OF F			
Hanscom AFB Massachusetts 01731		PROGRAM ELEMENT NO.	PROJECT NO.	TASK NO.	WORK UNIT NO.
11. TITLE (Include Security Classification) Process 1984 Antenna Applications Symm		62702F	4600	14	01
12. PERSONAL AUTHOR(S)	JUSTAN				
					
In-house 13b. TIME C	то	14. DATE OF REPORT (Yr., Mo., Dey) 15. PAGE COUNT 282			
16. SUPPLEMENTARY NOTATION Volume I 2/5 through 686. Daniel T. McGrath, Contract Mc	consists of pag onitor (RADC/EEA	es 1 through)	n 274; Volume	II consists	of pages
17. COSATI CODES	18. SUBJECT TERMS (C	ontinue on reverse i	necessary and identi	fy by block number)	1
FIELD GROUP SUB. GR.	Phased array an Millimeter wave			rip antennas ; or antennas ;	
19 ARSTRACT (Continue on reverse if necessary sho	Millimeter wave Near-field ante		nents	•	'/
The Proceedings of the 1984 Antenna Applications Symposium is a collection of state-of-the-art papers relating to phased array antennas, millimeter wave antennas, microstrip and conformal antennas, reflector antennas, and near-field antenna measurement techniques.					
C Visit Sir		QUALITY INSPECTED	cession For IS GRAEI C TAB maounced	trib alla	
20. DISTRIBUTION/AVAILABILITY OF ABSTRACTURE OF ABSTRACTURE OF ABSTRACTURE OF AME AS RPT.		21. ABSTRACT SE		CATION A	Dist.
22a. NAME OF RESPONSIBLE INDIVIDUAL	Q DITCUSERS C	Unclassified 22b. TELEPHONE NUMBER 22c. OFFICE SYMBOL			
Daniel T. McGrath, Capt, USAF		(Include Area	Code)		
DD SORM 1472 00 ADD		(617) 861-4	W.36	RADC/EEA	

PREFACE

The Antenna Applications Symposium, held at the University of Illinois' Robert Allerton Park, was cosponsored by Rome Air Development Center's Electromagnetic Sciences Division (RADC/EEA), Hanscom AFB, MA and the University of Illinois, Urbana, IL under contract F19628-84-M-0002.

Contents

Volume I

Key	note: "New Antenna Technology," W. T. Patton	1
	Wednesday, September 19, 1984	
	Session I	
	Arrays	
1.	"Considerations for Millimeter Wave, Monolithic Phased Arrays," D. H. Schaubert, D. M. Pozar, K. S. Yngvesson and R. W. Jackson	g
2.	"The Design of a Thermally Efficient 1:256 Ku-Band Feed Network for a MMIC Phased Array," C. A. Hancik, D. E. Heckaman and E. J. Bajgrowicz	37
3.	"Characterization of MMIC Devices for Active Array Antennas," J. Smetana E. Farr and R. Mittra	57
4.	"Waveguide Slot Array with ${\rm Csc}^2\theta$ Cos θ Pattern," J. J. Erlinger and J. R. Orlow	83
5.	"Sheet Metal Waveguide Forming Technique," P. K. Park and S. E. Bradshaw	113
6.	"Considerations for Extending the Bandwidth of Arrays Beyond Two Octaves," G. J. Monser	123

Contents

Session II

Microstrip Antennas and Lenses

7.	"Microstrip Monopulse Dipole Array," W. Miccioli, J. Toth, N. Sa and M. Lewis	149
8.	"Theory and Experiment for Infinite Microstrip Arrays," S. M. Wright and Y. T. Lo	171
9.	"Circularly Polarized Microstrip Antennas," Y. T. Lo, B. Engst and R. Q. H. Lee	197
10.	"Radiation and Scattering Performance of Microstrip Antennas Using Exotic Substrates," J. J. H. Wang	219
11.	"A High-Efficiency, Low-Phase Error Waveguide Lens for a Transform Feed Antenna," D. T. McGrath	235
12.	"Computer-Aided Bifocal Dielectric Lens Antenna Design for MM Wave Application," S. Y. Peng	257
	Volume II	
	Thursday, September 20, 1984	
	Session III	
	Analysis, Measurements and Auxiliary Devices	
13.	"A Moment Method Solution to Spiral Antenna Radiation," P. Skinner and A. J. Terzuoli	275
14.	"Characterization of Dumbbell Slots in Rectangular Waveguide by Method of Moments," P. K. Park and I. P. Yu	291
15.	"The Effect of Quantization on the Dynamic Range of Adaptive Processors," A. R. Cherrette, J. F. O'Connor and D. C.D. Chang	297
16.	"Antenna Phase Center Movement in UHF Radio Positioning Systems," J. M. Tranquilla and S. R. Best	311
17.	"Approach to a Suitable Directional Antenna for UHF Radio Positioning Applications," J. M. Tranquilla and S. R. Best	341
18.	"Four Band Radar Augmentation System for High Performance Targets," H. B. Sefton, Jr	365
19.	"Design and Error Analysis for the WR10 Thermal Noise Standard," W. C. Daywitt	393

Contents

Session IV

Reflector Antennas

20.	"Constrained Overlapping Feed Arrays for Contiguous Contour Beam Reflector Antennas," V. Galindo-Israel, Y. Rahmat-Samii, W. Imbriale, H. Cohen and R. Cagnon	419
21.	"AUSSAT Ku-Band Space Antenna Subsystem," E. C. Ha, L. G. Clouse, K. A. Simmons, K. Clausing, M. D. Harwood and M. J. Glaser	449
22.	"Controlled Surface Distortion Effects," D. Jacavanco	479
23.	"Null Generation by Phase Perturbations in an Aperture," M. D. Rudisill and A. J. Terzuoli	503
24.	"Analysis of the Cross-Polarization Performance of Alternative Csc ² Doubly Curved Reflector Antenna Geometries-Preliminary Results," T. F. Carberry	517
	Friday, September 21, 1984	
	Session V	
	Near-Field Techniques	
25.	"Probe Correction for Near-Field Antenna Measurements," A. D. Yaghjian	549

25.	"Probe Correction for Near-Field Antenna Measurements," A. D. Yaghjian	549
26.	"Optimum Probe Design for Near Field Scanning of Ultralow Sidelobe Antennas," K. R. Grimm	589
27.	"Case Study of Sample Spacing in Planar Near-Field Measurement of High Gain Antennas," R. J. Acosta and R. Q. Lee	613
28.	"Comparison of Measured and Calculated Mutual Coupling in the Near Field Between Microwave Antennas," C. F. Stubenrauch and M. H. Francis	621
29.	"Prediction of Low Sidelobe Antenna Performance in the Presence of Large Scatterers Using RF Field Probe Techniques," J. Wojtowicz, R. Konapelsky, J. Havrilla, R. Vogelsang and K. Ramsey	643
30.	"Extension of Plane-Wave Scattering-Matrix Theory of Antenna-Antenna Interactions to Three Antennas: A Near-Field Radar Cross Section Concept," M. A. Dinallo	665

New Antenna Technology

Willard T. Patton RCA Government Systems Division

I am very pleased though somewhat surprised at being asked to set the keynote for this 1984 Antenna Applications Symposium. I am pleased because I have enjoyed this symposium for over 20 years. In fact, I tended bar here in 1960 and 1961. I was surprised because it has usually been the practice at this symposium to have a representative of one of the Government labs, our customers, state where he feels the needs for antenna technology lie. This then provides those of us in industry and at the universities with direction for the development of technology to satisfy those needs. This keynote will not be that.

Why me? Alan Schell responded to this question by stating that my position as Chairman of the Antenna and Propagation Society's New Antenna Technology Committee has made me ideally qualified to deliver a 20 to 30 minute address. He may have overlooked the fact that the ability to give a keynote address is not a prerequisite for the chairmanship of an AP Adcom Committee, and is not in the job description. I am nonetheless honored, and as I have said before, pleased to have this opportunity to address this segment of the antenna design community this morning.

The topic, then, is New Antenna Technology, the issues and the trends. Later, perhaps during the breaks, you may be good enough to tell me how the APS can serve you better in this area. One of the issues in this arena is the relationship between antenna applications and antenna technology. This is the issue which makes New Antenna Technology an appropriate topic for this meeting. For the purpose of this discussion, we will define an antenna application to be an electromagnetic radiating device designed to satisfy a specific set of system performance requirements. On the other hand, the term antenna technology encompasses the totality of practical antenna applications, components, fabrication methods, and testing technology. Under this somewhat narrow definition less than half the papers at this symposium are applications papers, but most if not all of the papers on technology are derived in support of a specific application. In a sense, the antenna application is old news, a problem solved, on equipment built. What makes an application exciting is the technology that it demonstrates, and the technology that it shows to be practical. The application may also have fostered new technology which will find its way into yet other applications. In this way, an antenna applications symposium is an excellent vehicle to bring new antenna technology to practicing antenna engineers.

If we view the application as one boundary of antenna technology, then, at its other boundary, lies science in which the performance of the antenna becomes an end in itself, with only vague notions about possible applications. Not too much further along the boundary of antenna technology, we also find those antenna capabilities of great promise that await technological developments in other areas. The whole field of digital beamforming antennas is an excellent example.

Another issue in the area of New Antenna Technology is the blurring of the boundary between the antenna and the system of which it is a part. In fact, it was a concern for this issue that caused APS past President Bob Mailloux to establish the New Antenna Technology Committee. The official function of this committee is to make the latest antenna technology more readily available to Antenna and Propagation Society membership. The unofficial purpose for the committee is to maintain and strengthen the position of the Antenna and Propagation Society in those areas in which the boundary between the antenna and the system is becoming blurred.

Several areas have been targeted by the APS New

Antenna Technology Committee for special treatment that will
initially result in special issues of the <u>Transactions</u>. The
first of these special issues, to be edited by Bill Gabriel,
is on the subject of adaptive and digital beamforming
antennas. It deals with the boundary between the antenna and
the signal processing functions of a system. The second

special issue, to be edited by Ron Stockton, is on integrated antenna technology. It deals with the boundary between the antenna transmitter and receiver functions of a system. Both of these issues might be considered to be application oriented. The third special issue, to be edited by Dick Johnson, is on near field antenna measurement systems. It might be considered pure antenna technology but its implementation usually is a major system in its own right, a system valued at seven figures not counting pennies. The publication rate for these special issues will be one per year starting in 1985. If these are well received and accomplish their purpose, we plan to continue with topics like Millimeter Wave Antenna Technology and Spaceborne Antenna Systems.

I would like to deviate now from the focus of the New Antenna Technology Committee. The central issue of the antenna profession as reflected here and in the APS transactions is simply the development of new antenna technology. That development is usually accomplished by taking advantage of emerging technology in an effort to satisfy increasingly demanding system requirements.

Perhaps the greatest single force in the development of antenna technology in the past two decades has been the computer and computer technology. We are most familiar with the computer in its role as a tool for antenna analysis. The computer simplifies the analysis of antenna patterns, facilitates the computation of current

distributions and antenna impedances, and optimizes reflector contours. The modern term for this role is Computer-Aided Design.

Another way the computer has had an impact on antenna technology is through facilitating measurements of antenna properties and at the same time improving their accuracy. This impact is expressed at the component level in the automatic network analyzer, and at the antenna system level in the near field antenna analyzer. When I started working in this field, a measurement of antenna gain with an accuracy of plus or minus half a dB was considered good. In this age of Computer-Aided Testing and communications satellites, millions of dollars can depend upon the measurement of one tenth of a dB of antenna pattern performance. We are also beginning to see the benefits of Computer-Aided-Manufacturing in reduced antenna costs and improved antenna performance characteristics.

The greatest impact of computer technology on antenna technology is embodied in the phased array antenna. Certainly it benefits from CAD-CAT-CAM as have other modern antennas. More significantly, the use and benefits of a phased array antenna depend upon the computer for control and data management.

I will use a phased array antenna, currently in serial production, to illustrate the continuing interaction between application and technology. The independent research and development leading to the development of this phased

array antenna was begun in 1967. This work used the newly available Automatic Network Analyzer extensively. The engineering development model, begun in 1970, was tested in a computer controlled far-field range. In 1975, the planar near field technology being developed at the National Bureau of Standards, the University of Colorado, and elsewhere was applied. This technology was extended to perform beamformer alignment under computer control for this antenna application.

In 1980, changing requirements led to the definition of a second generation system with substantially improved performance. The phased array antenna was assigned a major part of the required performance improvement. Better antenna performance requires better control of the amplitude and phase of the aperture distribution. Specifically, the requirements for the new antenna dictate that a two thousand by three monopulse beamforming network replace one with only sixty-eight by three ports. Achieving the required precision economically required the application of CAD-CAT-CAM technology.

It required the direct application of digital technology to store and apply the phase alignment data, and it required the development of new antenna technology to obtain that phase alignment data. The near-field antenna system test facility, built to acquire precise phase alignment data, uses processing algorithms, which I described here in 1981, to provide resolution to the level of the

individual elements in the array. The scanner also uses extensive laser metrics and data correction techniques specifically developed to fill the needs of this antenna system.

This is just one example of the way in which the antenna application responds to technology, and the way in which it inspires the development of technology. Your experience, and the reports of those who follow, will provide others examples.

Finally, let me remind you that Webster's New Collegiate Dictionary says that a symposium is, "a formal meeting at which several specialists deliver short addresses on a topic or on related topics, ... a social gathering at which there is free interchange of ideas ... from the Greek word sympenein: to drink together." I know you will find that this occasion fulfills the definition admirably.

CONSIDERATIONS FOR MILLIMETER WAVE,

MONOLITHIC PHASED ARRAYS

D.H. Schaubert, D.M. Pozar, K.S. Yngvesson, and R.W. Jackson

Department of Electrical and Computer Engineering

University of Massachusetts

Amherst, MA 01003

Abstract

Some candidate elements for millimeter wave, monolithic phased arrays are discussed. Results of analytical and experimental investigations of printed antennas on high permittivity substrates are presented and discussed in relation to EHF array performance. Scan impedance and blindness are evaluated by analysis and experiment. Methods for interfacing active devices such as FETs with candidate array elements are also discussed.

1.0 Introduction

There is a wide variety of applications ranging from communications to remote sensing that will benefit from the realization of monolithic millimeter wave arrays. However, that realization will require the solution of a number of difficult problems. In this paper, progress is reported in two major areas of investigation: monolithic elements and arrays, and active devices in monolithic transmission lines. The paper reports both analytical and experimental results, some of which are complete and some of which are preliminary.

In the area of array elements, the study includes dipoles and patches on grounded substrates and dipoles and slots on semi-infinite substrates. For all of these configurations a method of moments formulation was used to compute the input impedance of single elements and validated by measurements of isolated elements and elements in waveguide simulators. The scan blindness that must be considered for grounded substrates does not occur on semi-infinite substrates, which also enhance the radiation in the direction of the high permittivity medium.

In the area of active devices for monolithic circuits, work has begun to integrate FETs with appropriate transmission lines. FET oscillators have been fabricated in microstrip circuits by using discrete components. These oscillators were injection locked to a local oscillator and their outputs were used to feed a

microstrip patch antenna. This circuit is a building block for a spatial combining array and its performance in small arrays is being investigated. For slot antennas, coplanar waveguide (CPW) might be used for the feed circuit and we have begun a study of slot antennas fed by CPW and of FET amplifiers in CPW. Preliminary results will be presented.

2.0 Monolithic Array Elements and the Array Environment

Printed antennas on a grounded substrate of GaAs have been considered as a building block for monolithic EHF phased arrays. These elements are naturally suited to the environment of monolithic circuits and they possess many characteristics that make them desirable. However, it is a significant technological leap from microwave radiators on ϵ_r^2 2.5 substrate to complete arrays with amplifiers, oscillators and phase shifters on ϵ_r^2 13 substrate. A number of problems, including surface waves, substrate area and transmission line losses, have already been encountered and it is likely that our present concepts of the best monolithic configuration will be altered by work that is now in progress.

In this section, several candidate elements are described and some of their important characteristics are studied. The results

provide a basis for comparison of element performance in the monolithic array environment.

2.1 Types of Elements

This paper considers four types of elements; 1) dipoles on a grounded substrate, 2) patches on a grounded substrate, 3) dipoles on a semi-infinite substrate, and 4) slots on a semi-infinite substrate. The elements on grounded substrates are familiar from microwave frequencies, 1 but their characteristics on thicker substrates of higher permittivity is not yet known. The elements on semi-infinite substrates are useful for applications where a high permittivity plano-convex lens is bonded to the unclad side of the substrate. 2 They may also offer some advantage in obtaining a partially unidirectional element without the menacing surface wave of a grounded substrate.

Other types of elements that may be useful for monolithic systems but that are not studied in this paper include printed dipoles with superstrates, ³ electromagnetically coupled dipoles or patches, ^{4,5} and microstrip or stripline fed slots. ⁶

2.2 Input Impedance of Monolithic Elements

The input impedance of a monolithic element can be calculated by using the method of moments to solve the appropriate integral

equation. Two difficulties arise; 1) an accurate characterization of the currents on the element and the feed structure may be difficult to obtain with a small number of expansion modes and 2) the calculation of matrix elements requires numerical evaluation of double infinite integrals of the Sommerfeld type. The first difficulty requires judicious modeling of the structure and also usually forces us to accept solutions that are not as general or as accurate as we might like. The second difficulty is usually solved by cleverness and brute computation. Several useful results for microstrip patches and dipoles have appeared recently. 3,7,8,9 They are based on the use of the correct Green's function for the grounded slab and they contain surface wave effects.

Some results of Pozar's analysis 10 are shown in Figures 1 and 2. The resonant resistance of a microstrip patch and of a center-fed half-wave (first resonance) and a full-wave (second resonance) printed dipole are shown versus substrate thickness. Note that the full-wave dipole resistance is in hundreds of ohms. The importance of surface waves is illustrated by Figure 2, which shows the efficiency of radiation defined as the ratio of space-wave power to space plus surface-wave power. The dramatic effect of higher permittivity is illustrated by the differences between Figures 2a and 2b.

The input impedances of dipoles and slots on a semi-infinite substrate have been calculated 11 by using a method similar to that described above for microstrip elements. One notable difference is

the absence of any surface waves. Typical results for the input impedances of slots and dipoles (Fig. 3) are shown in Figure 4. The curves labelled as Booker's relation were obtained from the formula given in the figure with ε_e equal to the average dielectric constant (ε_e = (ε_r +1)/2). It is interesting to note how closely these curves agree with the more rigorous calculations, even though the antennas are not truly dual structures.

The isolated element impedances described above are useful for understanding element and array behavior, but mutual coupling between array elements can have a devastating effect on scanning array performances. 12, 13 The analysis described for single elements can be extended to infinite periodic arrays of elements by using Floquet techniques. This has been done and the input impedance of an array of printed dipoles on a relatively thick $(0.06\lambda_{\Delta})$ substrate has been calculated as a function of scan angle. The magnitude of the reflection coefficient for scanning in three planes is shown in Figure 5. The element spacing is $0.5\lambda_0$ in a square grid and the dipole length of $0.156\lambda_0$ is chosen for resonance at broadside scan. A waveguide simulation for a rectangular grid array with relatively large spacing (0.0443m) in the Eplane was fabricated to test the theory. Measured and calculated results are shown in Figure 6. The substrate here is very thick and this example serves as a test of the theory and not a practical design.

Similar calculations have been performed for arrays of microstrip patches, 15 and for arrays of dipoles and slots on semi-infinite substrates. Some typical results are shown in Figures 7-9. In Figures 8 and 9, the beam in air scans from 0° to 90° while the beam in the dielectric scans from 180° to 163.77° , which is the critical angle $\theta_{\rm c}$. Scan angles between 90° and $\theta_{\rm c}$ result in no beam in the air region.

One weakness in the present analytical formulation for patch antennas is that a simplified model is used for the feed-to-patch connection region. This model is known to be accurate for thin, low-permittivity substrates, but it does not accurately predict the input impedance of patches on electrically thick substrates. The simplified model is probably adequate for a 20-CHz array, but may not be adequate for a 40-CHz array.

2.3 Radiation Patterns of Monolithic Elements

The radiation pattern of a printed element can be calculated once the current on the element is known. The radiation patterns of microstrip dipoles and patches on high permittivity substrates are essentially the same as for these elements on the low permittivity substrates commonly used at microwave frequencies, except that the E-plane pattern is slightly broadened due to the fact that the element is shorter on the high permittivity substrate. Another

exception occurs when the substrate becomes thick enough that significant power goes into surface waves (see Fig. 2). In that case, scattering of surface wave power can significantly alter the observed radiation pattern.

Calculated radiation patterns¹¹ for dipole and slot elements on semi-infinite dielectrics of various permittivities are shown in Figure 10. The dipole patterns exhibit an E-plane null and an H-plane bulge at the critical angle in the dielectric. These features are not present in the slot patterns because the ground plane effectively isolates the dielectric from the air. Another important feature of both the slot and dipole patterns is the enhancement of radiated power density in the dielectric. For a single element, the power density at $\theta=180^{\circ}$ is $\epsilon_r^{3/2}$ times that at $\theta=0^{\circ}$. This effect may be useful if an appropriate means of matching for power transfer from the dielectric into air can be devised.

3.0 Active Devices and Their Coupling to Antenna Elements

In order to complete the concept of a monolithic array, active devices for amplifiers, mixers, and phase shifters must be connected to the radiating elements. This will require the use of appropriate transmission lines. For elements on a grounded substrate, microstripline is a natural choice, but a balanced two-conductor line over ground can also be used for balanced radiators such as dipoles. Other types of transmission lines that guide

the power along the ground-plane surface are slotline and coplanar waveguide. Some possible means of connecting elements to these types of lines are illustrated in Figure 11.

An important factor to consider is loss in the feed network. By using published values for the attenuation in microstriplines on GaAs¹⁷ and following the calculations of James et al¹⁸, the maximum gain of printed arrays with corporate feeds can be found. Assuming an element gain of 6 dB, a square array of size L x L, and an average feed line length of 1.5L, the maximum gain obtainable from an array on 4-mil GaAs is about 20 dB in the 20 to 40 GHz range. Increasing the array size beyond about 14 cm at 20 GHz results in lower gain because feedline losses offset antenna gain from increased aperture. The use of a 10-mil substrate offers about 30 dB gain, but problems caused by surface waves and related effects are worsened. Another alternative, which is natural for integrated arrays, is to offset feedline losses with amplifiers located throughout the network.

3.1 Receiver Array Considerations

It is likely that the transmit and receive functions will be performed by separate arrays. This allows optimization of each function. For receiver arrays in the lower millimeter wave frequencies, the first active element will probably be a FET preamp. MESFETs already have a lower noise figure than mixer receivers at

substrate. Also, failure of a few modules should not have a catastrophic effect on array performance.

One of the key problems associated with spatial combining is the ability to phase lock a number of transmitters. Injection locking of FET oscillators has been demonstrated 20, but the phased array application requires that there be no uncertainty in the phase of the oscillator output. To investigate this problem, a two element array with injection-locked FET oscillators has been fabricated (Fig. 13). This array is being tested to determine if a reliable beam can be formed and steered by controlling the phase of the locking signal.

4.0 Summary

Several considerations for monolithic millimeter wave phased arrays have been discussed. Four types of radiating elements for grounded substrates and semi-infinite substrates have been analyzed. Experimental results have verified the analyses for several of these elements, but accurate and efficient models for the feed region of antennas on thick substrates are needed. Microstrip elements have been found to perform similarly to their microwave counterparts as long as the substrates are electrically thin. Thicker substrates lead to a variety of pattern and impedance effects.

Arrays of microstrip dipoles and patches have been analyzed and the active impedance and scan blindness phenomena examined. Arrays on semi-infinite substrates do not have a blindness within the region corresponding to visible space in air, but wide angle impedance matching is needed to transfer the radiated power from the dielectric into air. Also, these arrays radiate a significant amount of power in the backward direction, which must be properly handled.

Potentially useful configurations for active devices are being studied. Preliminary evaluations are encouraging and work is continuing.

This work was supported by RADC Electromagnetic Sciences Division, Hanscom AFB, under contract number F19628-84-K-0022.

References

- 1. D.C. Chang, ed. (1981), Special Issue on Printed Circuit Antennas, IEEE Trans. Ant. Prop., AP-29 (No. 1).
- 2. D.B. Rutledge, D.P. Neikirk and D.P. Kasilingam (1983), Integrated Circuit Antennas, in Infrared and Millimeter Waves Series, Vol. 11, K.J. Button, Ed., Academic Press, New York.
- 3. D.R. Jackson and N.G. Alexopoulos (1984), Superstrate (cover) Effects on Printed Circuit Antennas, Proc. IEEE AP-S Sym. Boston: 563-565.
- 4. P.B Katehi and N.G. Alexopoulos (1984) A Generalized solution to a Class of Printed Circuit Antennas, Proc. IEEE AP-S Sym. Boston: 566-568.
- 5. H.G. Oltman and D.A. Huebner (1981) Electromagnetically Coupled Microstrip Dipoles, <u>IEEE Trans. Ant. Prop.</u> AP-29 (No. 1): 151-157.
- 6. K. Arkind, private communication.
- 7. D.M. Pozar (1982), Input Impedance and Mutual Coupling of Rectangular Microstrip Antenna, IEEE Trans. Ant. Prop. AP-30 (No. 6): 1191-1196.
- 8. I.E. Rana and N.G. Alexopoulos (1981), Current Distribution and Input Impedance of Printed Dipoles, <u>IEEE Trans. Ant. Prop.</u> AP-29 (No. 1):99-105.

- 9. P.B. Katehi and N.G. Alexopoulos (1983), On the Effect of Substrate Thickness and Permittivity on Printed Circuit Antennas, IEEE Trans. Ant. Prop. AP-31 (No. 1):34-39.
- 10. D.M. Pozar (1983), Considerations for Millimeter Wave Printed Antennas, IEEE Trans. Ant. Prop. AP-31 (No. 5):740-747.
- 11. M. Kominami, D.M. Pozar and D.H. Schaubert (1984), Printed Dipole and Slot Antennas on Semi-Infinite Substrates, Proc. IEEE AP-S Sym. Boston: 559-562.
- 12. G.H. Knittel, A. Hessel and A.A. Oliner (1968), Element Pattern Nulls in Phased Arrays and Their Relation to Guided Waves, Proc. IEEE 56 (No. 11):1822-1836.
- 13. R.J. Mailloux (1972), Surface Waves and Anomalous Wave Radiation Nulls on Phased Arrays of TEM Waveguides with Fences, IEEE Trans. Ant. Prop. AP-20 (No. 2):160-166.
- 14. D.M. Pozar and D.H. Schaubert (1984), Scan Blindness in Infinite Phased Arrays of Printed Dipoles, IEEE Trans. Ant. Prop. AP-32 (No. 6).
- 15. D.M. Pozar and D.H. Schaubert (1984), Analysis of an Infinite Array of Rectangular Microstrip Patches with Idealized Probe Feeds, IEEE Trans. Ant. Prop., to appear, October 1984.
- 16. K.S. Yngvesson, T.L. Korzeniowski, R.H. Mathews, P.T. Parrish and T.C.L.G. Sollner (1982) Planar Millimeter Wave Antennas with Application to Monolithic Receivers, SPIE Proc. 337, Millimeter Wave Technology.
- 17. R.S. Pengelly (1982), Microwave Field Effect Transistors, Research Studies Press, also R.A. Pucel (1981), Design

Considerations for Monolithic Microwave Circuits, <u>IEEE Trans</u>.

Micro. Th. Tech. MTT-29.

- 18. J.R. James, P.S. Hall and C. Wood (1981), Microstrip Antenna Theory and Design, IEE Electromagnetic Wave Series 12, Peter Peregrinus Ltd.
- 19. A. Cappello and J. Pierro (1982), A 22-24 GHz Cryogenically Cooled Low-Noise FET Amplifer in Coplanar Waveguide, <u>Dig. IEEE MTT</u> Sym. Dallas.
- 20. Y. Tajima and K. Mishima (1979) Transmission-Type Injection Locking of GaAs Shottky Barrier FET Oscillator, <u>IEEE Trans. MTT MTT-27</u> (No. 5):386-391.

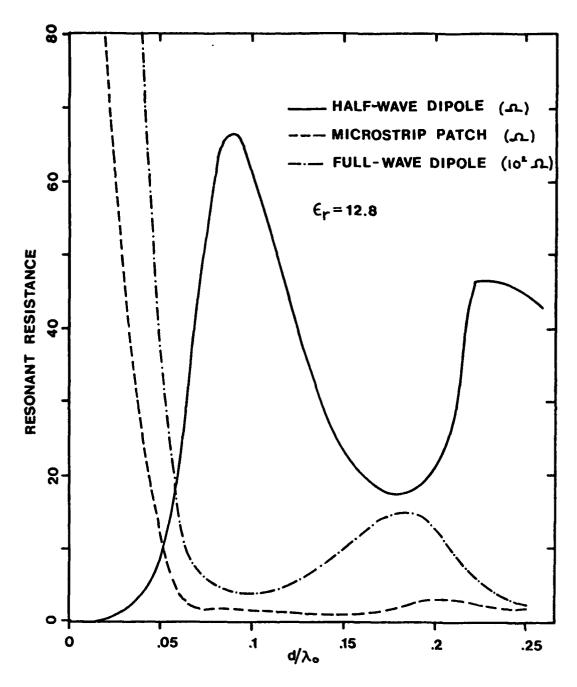
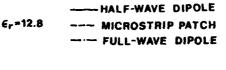
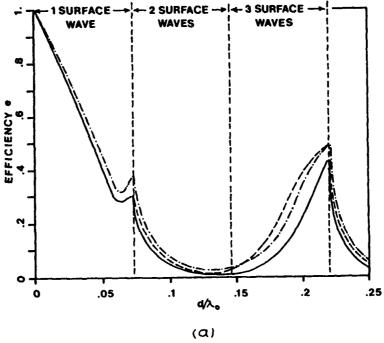


Figure 1. Input resistance of resonant microstrip patch and dipoles (half-wave and full-wave) on substrate $\epsilon_r = 12.8$ of thickness d. Dipoles are center fed and patch is fed at a point L/4 from edge. Patch width is 0.3 $\lambda_{\rm O}$.





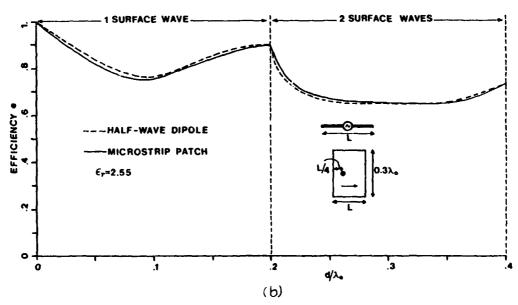


Figure 2. Efficiency due to surface wave excitation by printed dipoles and patches. Patch width is $0.3\lambda_0$. (a) ϵ_r =12.8 (b) ϵ_r =2.55.

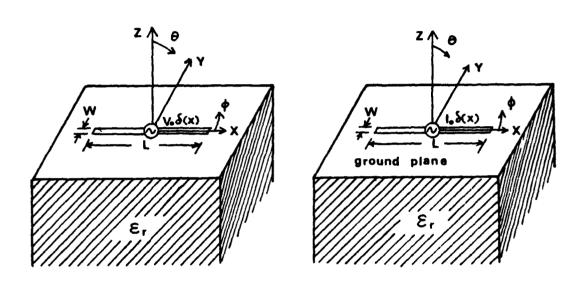


Figure 3. Antennas on semi-infinite substrate. (a) Printed dipole (b) Slot.

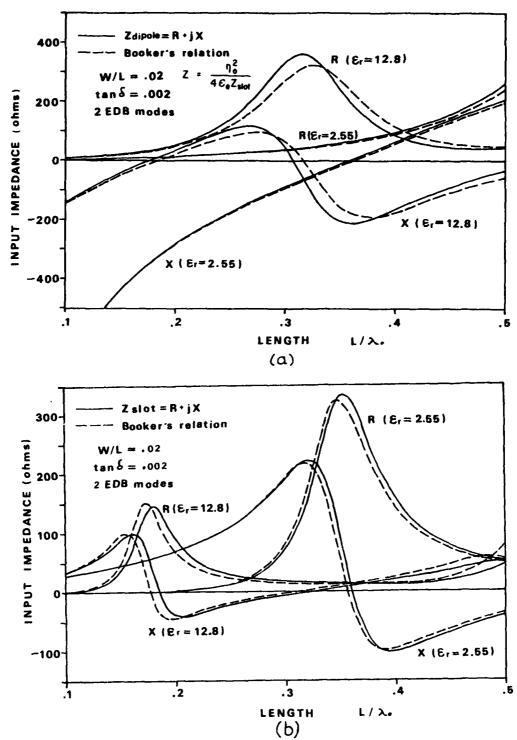


Figure 4. Calculated input impedance. (a) Printed dipole (b) Slot.

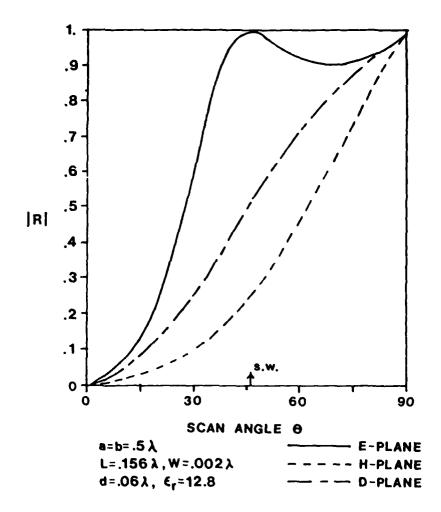


Figure 5. Calculated scan characteristics of infinite array of microstrip dipoles on $\varepsilon_{\rm p}$ =12.8 substrate for scanning in E, H and D planes. Reflection coefficient is calculated with respect to broadside input impedance, Z_b=9.3+j0.3.

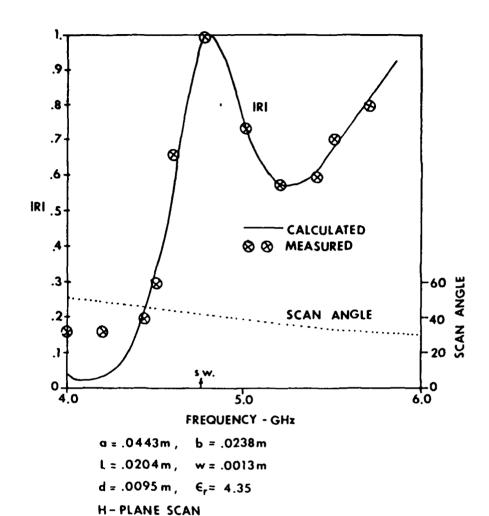


Figure 6. Measured and calculated active reflection coefficient (with respect to 50Ω) of infinite array of dipoles on thick substrate. Measured results are from waveguide simulation using monopoles.

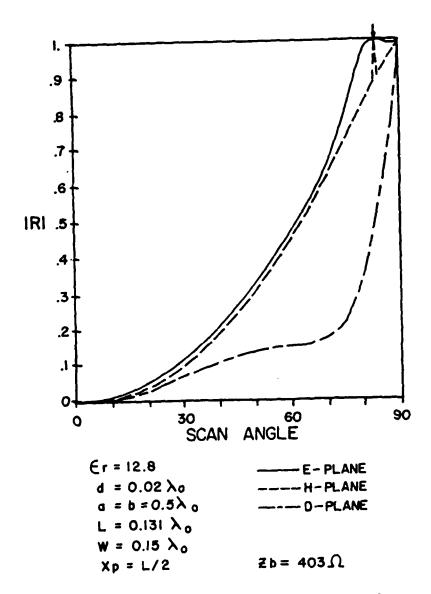
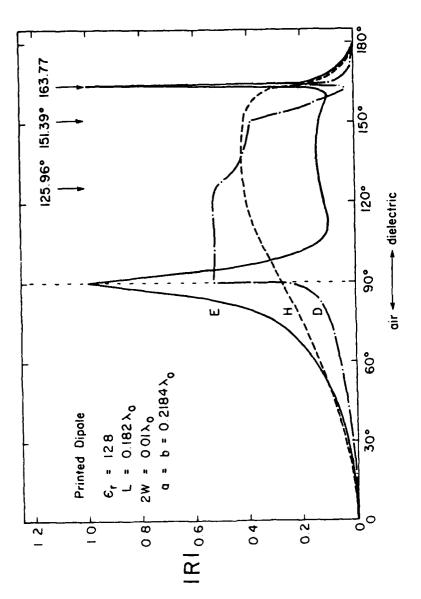


Figure 7. Calculated scan characteristics of infinite array of microstrip patches in square grid with spacing equal $0.5\lambda_0$.



SCAN ANGLE, 0

Figure 8. Calculated scan characteristics of infinite array of printed dipoles on semi-infinite substrate. 163.7 is critical angle and 125.9 and 151.4 are grating lobe boundaries in D plane.

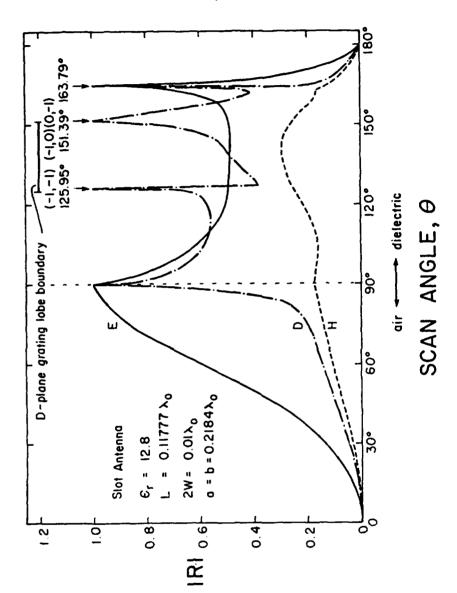
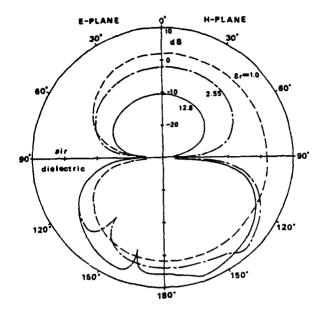


Figure 9. Scan characteristics of infinite array of slots on semi-infinite substrate. Array grid has same spacing as that of Figure 8.



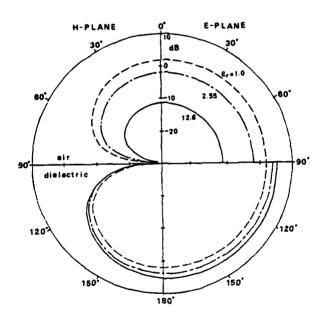


Figure 10. Power patterns of resonant elements. (a) Printed dipole (b) Slot.

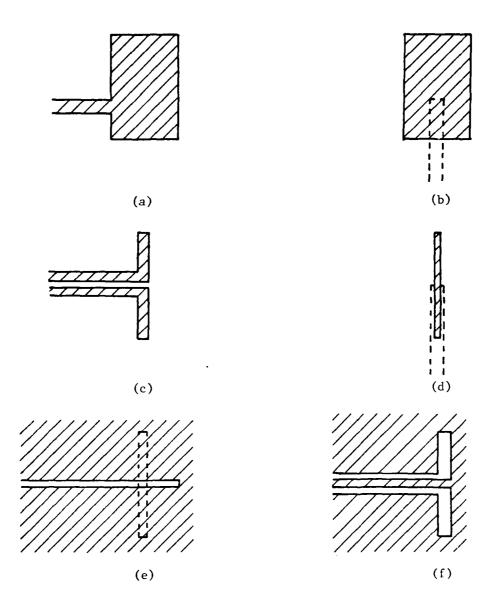


Figure 11. Some possible transmission line and element configurations for integrated structures. (a) Microstripline and patch. (b) Electromagnetically coupled (EMC) microstripline and patch. (c) Printed two-conductor line and dipole. (d) EMC dipole. (e) Slotline and dipole. (f) CPW and slot.

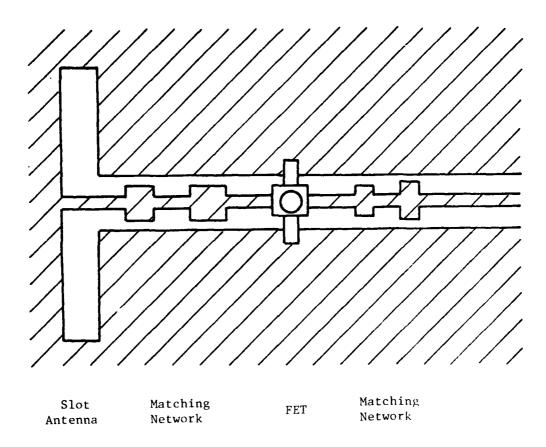


Figure 12. Proposed configuration for FET preamp connected to slot radiator by $\ensuremath{\mathsf{CPW}}$.

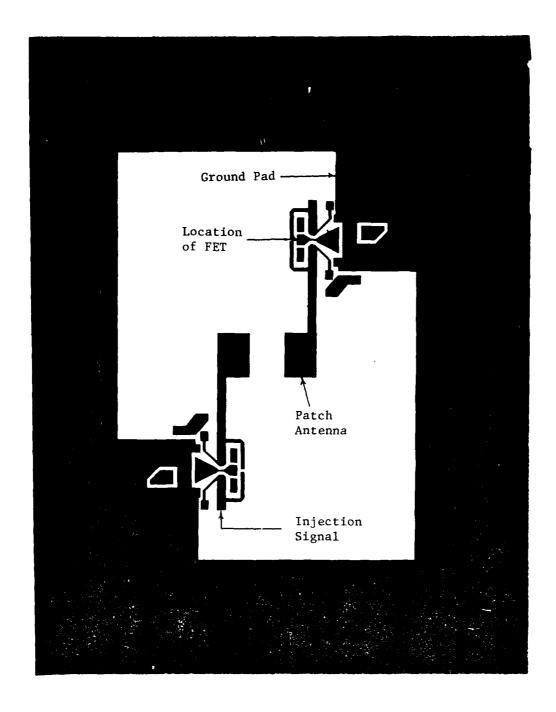


Figure 13. Photolithographic mask for injection-locked oscillators and antennas.

THE DESIGN OF A THERMALLY EFFICIENT 1:256 KU-BAND FEED NETWORK FOR A MMIC PHASED ARRAY

C. A. Hancik, D. E. Heckaman, E. J. Bajgrowicz
Harris Government Aerospace Systems Division
P. O. Box 94000
Melbourne, Florida 32902

1984 Symposium on Antenna Applications
September 19-21, 1984
Allerton Park
Monticello, Illinois

THE DESIGN OF A THERMALLY EFFICIENT 1:256

KU-BAND FEED NETWORK FOR A MMIC PHASED ARRAY*

C. A. Hancik, D. E. Heckaman, E. J. Bajgrowicz

Harris Government Aerospace Systems Division

ABSTRACT

A thin, thermally transparent, 1:256 corporate feed network for use in a GaAs MMIC Ku-Band phased array antenna has been designed. The network will be realized using a recently developed RF transmission medium called CHANNELINE. CHANNELINE consists of a core of TFE coated copper wire placed in a channel routed through a heat exchanging metal structure which composes the backside of the array. This unique packaging arrangement conserves both volume and weight while simultaneously allowing the rapid transfer of internally generated heat. The network is comprised of a 1:4 waveguide to CHANNELINE divider, four 1:16 microstrip/CHANNELINE dividers, and sixty-four 1:4 microstrip dividers. The final 1:4 divider is colocated in the module with the GaAs MMIC elements. This network is expected to realize better than 15 dB of return loss with less than 1.3 dB insertion loss over an 8% bandwidth. Finally, the current status of array hardware is presented.

^{*}This work is sponsored by Harris GASD, Melbourne, Florida

Table I. Ku-Band Phased Array

PRELIMINARY DESIGN GOALS

1.	R/T Mode	:	Half Duplex, 100% Tx Capability
2.	RF Bandwidth	:	8% at Ku-Band
3.	Tx Power	:	1.0 watt per element
4.	Input RF Rx Drive Power	:	0.1 watt
4. 5.	Noise figure	:	4.0 dB
	Array geometry	:	256 elements, triangular lattice
	Phase/Amplitude control	:	16 bit complex weight
	LNA burn-out	:	0.1 watt per element, up to 40 GHz
9.	Polarization	:	RHCP
	Scan angle	:	EL + 60°, AZ + 60°
	Control feed technology		High speed serial data
	Update rate	:	10000/sec
	DC Power available	:	1.3 kW
	Environment	:	100% Relative Humidity, radome
	Cooling		Forced convection, air or liquid
	Platform		F-15, F-16
			-

Introduction

At this writing, aerospace phased array antenna opportunities exist throughout the UHF, microwave, and millimeter wave frequency bands. From the Global Positioning System (GPS) at 1.2 GHz to Milstar at 44 GHz, phased arrays are being applied to solve today's airborne communication problems.

These efforts, coupled with the growing interest in monolithics, spawned an internally funded technology development project: To design and develop a controlled high performance monolithic phased array. Ku-Band was selected for the center frequency. This choice represents a compromise between the UHF band, which does not lend itself to monolithics technology, and millimeter wave band, in which MMIC technology is yet underdeveloped. The Ku-Band also allows the design to incorporate conventional hybrid technology as well. Table I lists the set of preliminary design specifications for this research and development array.

Conceptual Design

The conceptual array is illustrated in Figure 1. The two hundred and fifty-six (256) circular elements which comprise each subarray are arranged in a square shape with each row being offset one-half element from surrounding rows. This triangular lattice of elements is preferable to a square one for several reasons. Classic analysis shows that equivalent gain and scan angle can be achieved

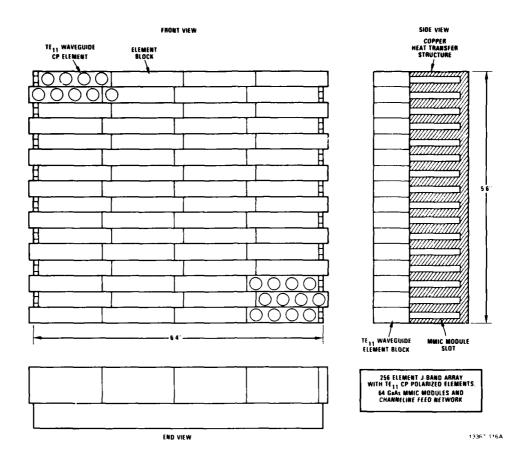


Figure 1. Front, Side and End Views of the Array

CROSS SECTION OF CHANNELINE ASSEMBLY

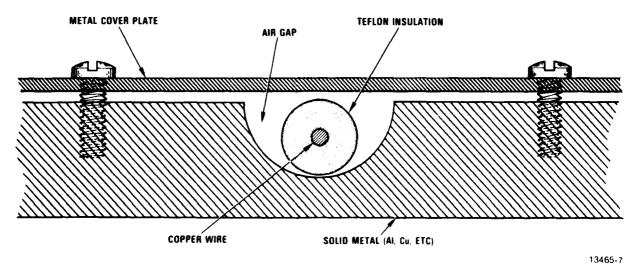


Figure 2. CHANNELINE Cross Section with Exaggerated Air Gap and Loose Cover Plate

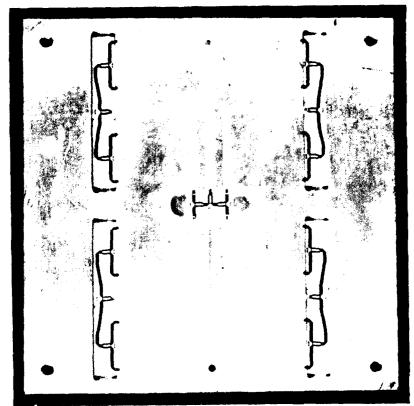
with 16% fewer elements¹. In arrays requiring several subarrays of this type (e.g., a 4096 element array composed of 16 subarrays), significant cost, weight, and volume reduction is realized. The concept of modular packaging is incorporated to permit quick and easy repair or replacement of any 4-element block or 256 element subarray.

In the event of a "stand-alone" application, a more circular array face would be used to aid sidelobe performance.

RF Corporate Feed Network

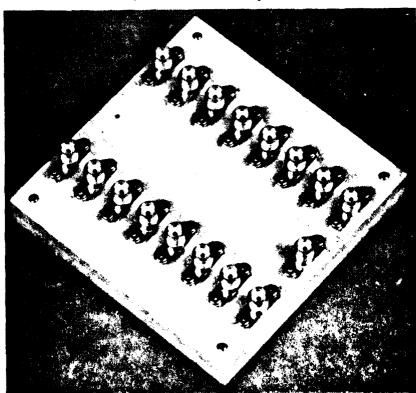
Presently, GaAs FET and MMIC technology is sufficiently advanced to allow the transmit array to operate at 15 GHz with a 100% duty cycle and one watt (1 W) of radiated power per element. For a 256 element array, approximately 1 kW of power would be generated within the array, most of it in the MMIC module and power amplifier directly behind the radiating structure. This configuration is shown in the side view of Figure 1. Since the array measures a mere eight inches (8.0") on a side, it must be capable of dissipating at least 15.6 W/in².

The problem, then, is how to conduct the heat away from the RF circuitry and into a heat exchanger on the backside of the array. Typically, the corporate feed network or beam former is located between the heat source and desired sink. Regardless of the type of feed network used, (i.e., microstrip, stripline, or waveguide) thermal conduction is impeded. The solution: A microstrip and coaxial transmission line feed network realized using



84-0642C

Figure 3a. Front View of CHANNELINE 1:16 Divider Assembly (Backside of Array)



84-0645C

Figure 3b. Back View of CHANNELINE Assembly (Aperture side of Array)

a recently developed RF transmission medium called CHANNELINE.

CHANNELINE consists of a single strand of TFE coated copper wire placed in a channel routed through a heat exchanging metal structure which composes the underside of the array. A cross-sectional view of this structure is shown in Figure 2. This structure supports quasi-TEM mode wave propagation. Note the air gap around the Teflon insulation near the cover. It is this gap that causes the dielectric medium to be slightly inhomogeneous, which in turn prevents it from supporting pure TEM waves².

The CHANNELINE connects the miniature precision thin film microstrip divider circuits located in cavities hollowed out of a thermally conductive backplane. Five 1:4 uncompensated Wilkenson dividers comprise the 1:16 assembly. Figure 3a depicts a frontal view of the assembly, while Figure 3b shows the output ports of this breadboard model. By using CHANNELINE transmission lines as the primary interconnection media within the array backplane, thermal efficiency is realized. Furthermore, CHANNELINE provides attenuation versus cross-sectional area performance comparable to waveguide without the interconnection headaches typically caused by the lack of available volume near the array face. This arrangement allows maximum use of the lower loss CHANNLELINE (0.03 dB/cm at 15 GHz) and minimum use of the higher loss per unit length microstip. The result is that approximately 88% of the divider structure is left available for unimpeded heat transfer. Circuit performance characteristics are shown in Figure 4.

1:16 CHANNELINE/MICROSTRIP POWER DIVIDER ASSEMBLY

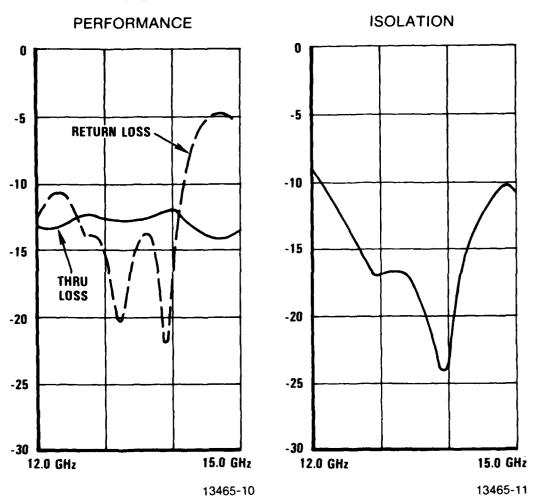


Figure 4.

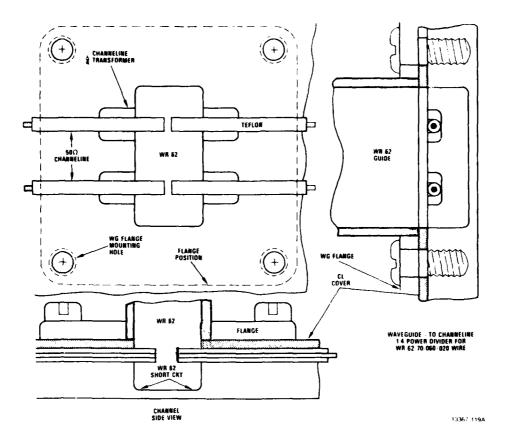
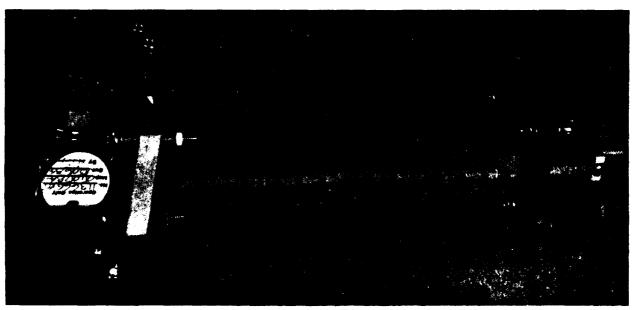


Figure 5.



84-1013CMR-2-5

Figure 6.

In the event of the 256 element assembly being a subarray of a larger antenna, the initial waveguide feed would interface with waveguide power divider prior to the CHANNELINE split. Because efficient heat transfer is accomplished at the subarray level, the longer runs required in a corporate feed network for the larger array can be built in full size waveguide for minimum attenuation. Primary amplitude taper, if required, could be incorporated in the waveguide splitter.

The corporate feed network for the 256 element array begins with a 1:4 waveguide to CHANNELINE divider. It is similar to a standard waveguide-to-coaxial adapter with the addition of a coaxial reactive 1:4 power divider. A cross-sectional view is shown in Figure 5. Impedance matching is accomplished by properly positioning the probes within the guide and/or by the use of quarter wavelength transformers in CHANNELINE.

A scale model breadboard was built at 10.5 GHz using WR 90 waveguide and 0.141 inch semi-rigid coaxial cable to simulate CHANNELINE. This model did not have the quarter wavelength matching transformers, rather, impedance matching was achieved by probe positioning only. As shown in Figure 6, a sliding waveguide short circuit was used to tune the transition. Insertion loss, return loss and isolation versus frequency for the circuit configuration are given in Figures 7 and 8. Although an optimum design has not been realized, these waveguide power divider experiments have

WAVEGUIDE TO CHANNELINE 1:4 DIVIDER PERFORMANCE

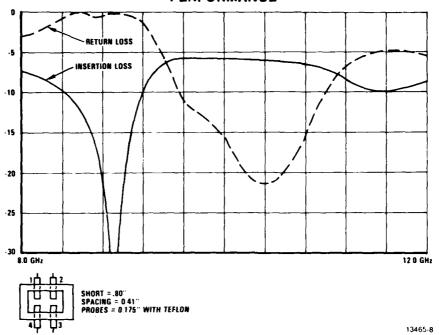


Figure 7.



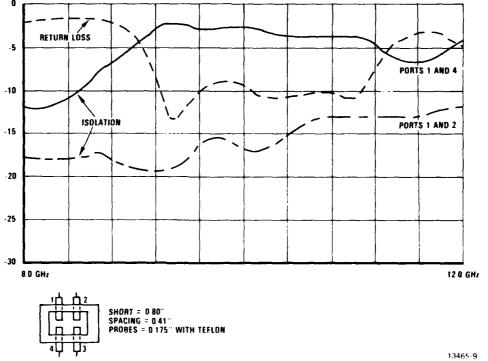


Figure 8.

demonstrated the feasibility of a simple, low loss waveguide to CHANNELINE 1:4 divider for the array-to-waveguide I/O interface.

The final 1:4 microstrip divider is colocated with the GaAs MMIC and housed in a Kovar module. There it is perpendicular to the thermal path, thus, it does not restrict heat flow.

In summary, the entire 1:256 feed network is comprised of A) a 1:4 waveguide to CHANNELINE divider, with <u>each</u> of its four CHANNELINES running to B) a 1:16 thermally efficient microstrip/CHANNELINE assembly whose 64 output ports each feed C) a final 1:4 divider which precedes the GaAs MMIC circuitry and the final radiating element. This rather complicated arrangement is clearly illustrated in Figure 9.

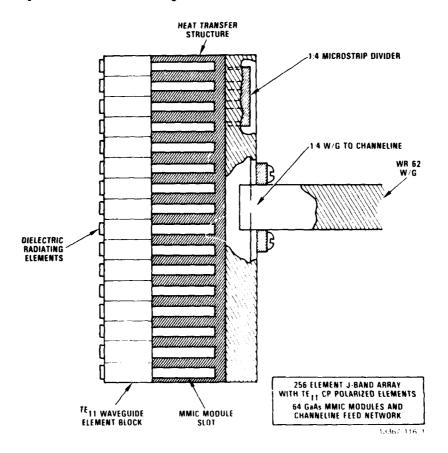


Figure 9.

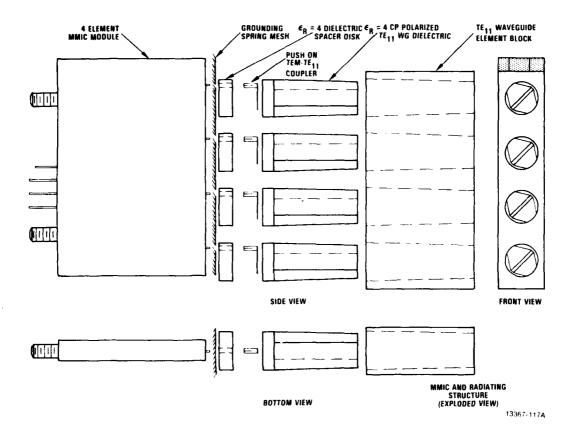


Figure 10.
WAVEGUIDE EXCITATION STRUCTURE

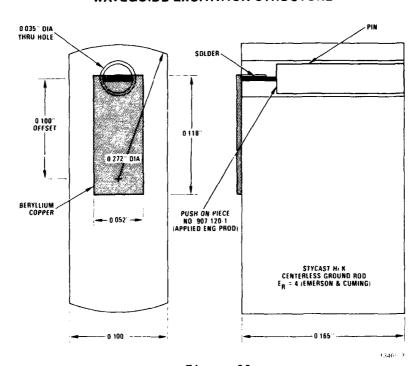


Figure 11.

Waveguide Radiation Element

The MMIC, radiation element, and circular waveguide block are shown in the exploded view of Figure 10. The actual radiating structure is shown in Figure 11. The circular waveguides have a coaxial pin launch at the module end. The cavity is filled with a dielectric transformer at the waveguide to free space interface. These "plug-in" dielectric radiating elements can be designed to produce either a linearly or circularly polarized antenna (Figure 12). An element test fixture using a 50 ohm glass-to-metal seal with an SMA push-on connector was developed to simulate the MMIC module/waveguide interface while testing the dielectric elements. Figure 13 is a photograph of this fixture with a linearly polarized element installed. The glass/metal seal is under the SMA launch.

RADIATING PIECE FOR CIRCULAR POLARIZATION

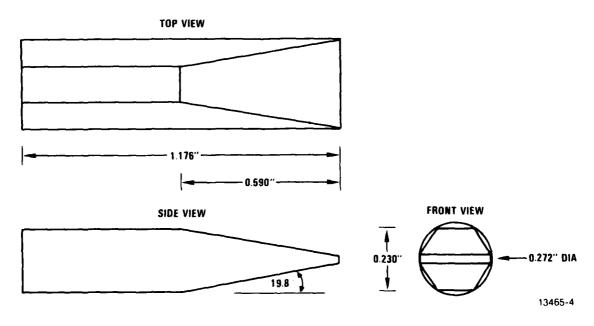
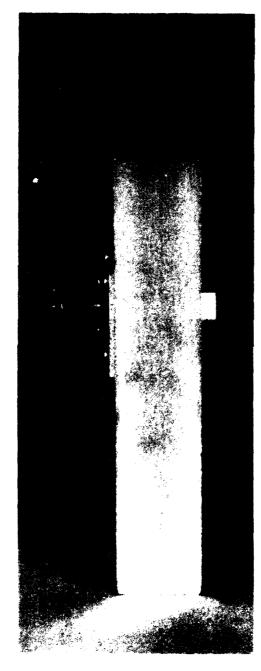


Figure 12.



84-1013CMR-1-2

Figure 13. Radiating Element Test Fixture with Linearly Polarized Element Installed

GaAs MMIC

The monolithic section of this phased array is also currently under development. A conceptual design is shown in Figures 14 and 15. The microstrip 1:4 divider passes the RF signal into a monolithic complex weight which feeds a GaAs FET power amplifier. In the receive mode, the incoming signal would encounter an LNA prior to being weighted and combined. On the digital side, a subgigabit rate serial control line made of miniature (Zo = 75 ohm) CHANNELINE is run into each module. This line feeds a high speed serial-to-parallel demultiplexer which also resides in the module. In this way, control wiring is minimized and precious area is conserved. These circuits, housed in a Kovar box, will perform all signal amplitude and phase control. They will also generate most of the heat which must be dissipated.

Initial thermal analysis indicates that the metal (copper or aluminum) comb/CHANNELINE heat transfer structure can be sufficiently cooled with either forced convection of air (if a finned heat sink is incorporated) or liquid (with no finned sink required). "Sufficiently cooled" may be defined as keeping the internal module temperature at less than 100°C. Electrically, this represents a viable operating temperature. Mechanically, it also ensures that the cooling liquid will not boil since the external wall of the structure must, by definition, be cooler than the internal comb and therefore operate at less than 100°C.

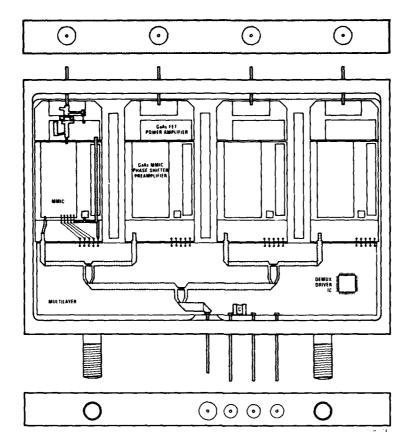


Figure 14.

KU-BAND ARRAY MONOLITHIC MODULE

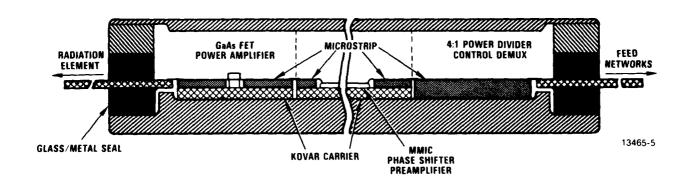


Figure 15.

Conclusion

Phased arrays are in demand because of their versatility.

GaAs MMIC's are also on the rise due to their size, weight,

performance, and power consumption aspects. The mating of the two

is a natural step in the progression towards smaller, lighter, and

leaner phased arrays. Monolithic LNA's, FET power amplifiers, phase

shifters, and complex weights, placed directly behind the antenna

aperture, can greatly improve overall performance. Packaging

technology must keep pace.

The design status of a 1:256 Ku-Band feed network has been presented. The assembly employs a newly developed RF transmission medium called CHANNELINE. Its size and thermal properties make it ideal for conserving both volume and weight while simultaneously allowing the rapid dissipation of internally generated heat. By blending this technology with existing hybrid and waveguide approaches, the heat transfer and packaging problems associated with small, high power, MMIC controlled phased arrays may be more readily overcome.

REFERENCES

Skolnik, Merrill I. (1970) <u>Radar Handbook</u>, McGraw-Hill, New York, p. 11-19

Paul, Clayton R. and Nasar, Syed A. (1982) <u>Introduction To Electromagnetic Fields</u>, McGraw-Hill, New York, p. 335

CHARACTERIZATION OF MMIC DEVICES FOR ACTIVE ARRAY ANTENNAS

Jerry Smetana NASA Lewis Research Center 21000 Brookpark Road Cleveland, Ohio 44135

Everett Farr and Raj Mittra
University of Illinois
Department of Electrical and Computer Engineering
1406 W. Green St.
Urbana Illinois 61801

Abstract

It has become evident from NASA's active array technology development activities that more attention to the characterization of MMIC devices is needed. Having been fabricated using lithographic techniques, the MMIC has some inherently reproducible RF characteristics. NASA is currently sponsoring studies by the University of Illinois to investigate certain aspects of MMIC interconnectivity. These investigations are expected to contribute to a data base that will lead to providing for reproducible test results by the user as well as the manufacturer.

Some considerations are proposed that lead to preserving the inherently reproducible characteristics of the MMIC. It is highlighted that at frequencies greater than 20 GHz, the transition from the MMIC device to other transmission media must be an accurate RF match. It is proposed that the RF match is sufficiently critical to include the transition as part of the delivered MMIC package.

The model for analyzing several transitions will be presented. This model consists of a succession of abrupt discontinuities in printed circuit transmission lines. The analysis of these discontinuities is achieved with the Spectral Galerkin technique, to generate the modes; and mode matching, to generate the generalized S-parameters of the individual discontinuities. Preliminary results achieved with this method are presented.

This paper concludes that special efforts should be coordinated by the active array antenna industry toward standardization of MMIC packaging and characterization.

1. Introduction

NASA is currently supporting technological development of fixed and scanning spot beam antenna systems at 20 and 30 GHz using monolithic microwave integrated circuit (MMIC) devices for active apertures. The approach is to develop the technology for the 20 GHz transmit antenna, then develop the 30 GHz receive antenna technology, finally combining the two technologies into a 30/20 GHz system.

Figure 1 shows two typical configurations of (a) Multiple Fixed Spot Beam Antenna; and (b) Multiple Scanning Spot Beam Antenna Systems. The advantages of using MMIC modules in spacecraft antenna systems were discussed at the 1982 Antenna Applications Symposium¹. In summary, the advantages are

- * Solid state power amplifiers (with distributed amplification)
- * Reliability through graceful degradation
- * Electronic beam steering
- * Phase and amplitude weightings for optimum performance
- * Dynamic reflector illumination control (as a function of scan angle)
- * FET switching (faster and more power conservative than PIN diode or ferrite switches)
- * Potential for lower weight and cost.

In order to provide sufficiently high power (for operation in geostationary orbit) and effective illumination control, arrays with a large number of radiation elements (100 to 1000) may be required. In such large arrays where dynamic phase and amplitude controls will be implemented, it is important to accurately characterize the module. It is also important that after they are characterized (on a network analyzer, for example), their performance is the same as for the array antenna. At

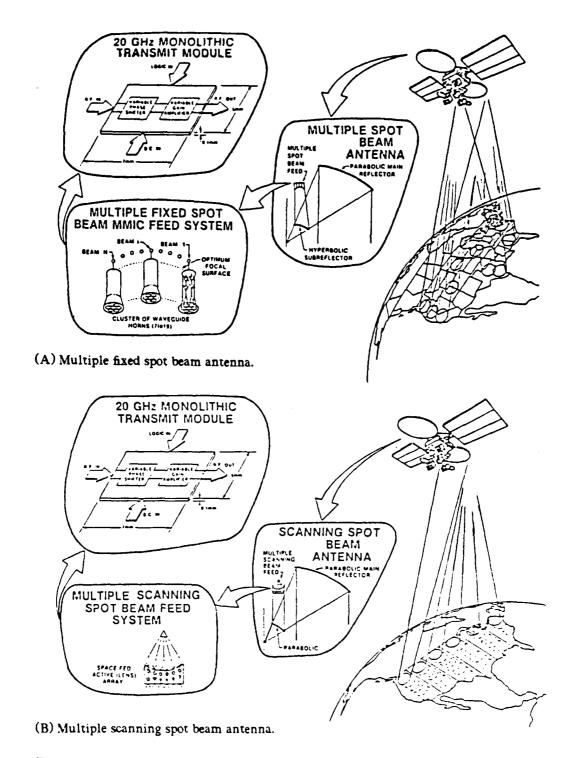


Figure 1. $30/20~\mathrm{GHz}$ satellite communications antenna systems.

frequencies greater than 20 GHz, the RF matching of the MMIC chip to a test station, as well as to the array antenna, is critical. Furthermore, when an array antenna is large, the multitude of long bias and control lines may be vulnerable to dispersion, crosstalk, or distortion from reflected pulses.

2. MMIC Interconnectivity

Figure 2 illustrates the functional components of an MMIC and summarizes its interconnectivity. Three aspects of the interconnectivity are considered: the RF connection, the long DC or logic lines, and the heat transfer. This paper will focus on the importance of the RF connection. NASA is currently sponsoring studies on MMIC transitions under Grant NAG3-420 with the University of Illinois. Some results on the analysis of these transitions will be presented in the second half of this paper.

The MMIC having been fabricated with lithographic techniques can be expected to have some inherently reproducible RF characteristics. It is of great interest to preserve this reproducibility. In order to achieve this, one needs to provide a good transition or matching network at the RF input and output. In addition, some consideration must be given to the environment around the chip. For example, when MMIC chips have different sizes, the shielding around them can produce a variety of mismatched conditions. This paper will discuss some considerations in the design of transitions and the packaging of MMIC chips in terms of their impact on the characterization of MMIC modules.

3. Characterization of MMIC Devices

It is important that there be an understanding between the MMIC

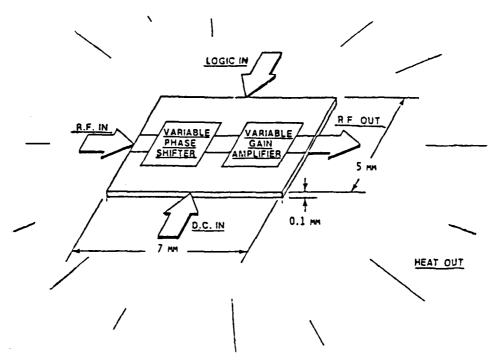


Figure 2. MMIC interconnectivity.

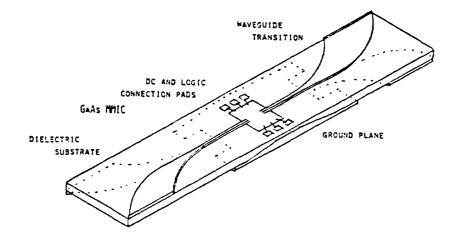


Figure 3. Typical packaging configuration.

manufacturer and the user about all the conditions of the MMIC testing, in order to avoid disagreement between the results. In addition, it is important that in its final mode of operation (an array antenna, for example), the MMIC has the same characteristics as it did in testing.

At frequencies greater than 20 GHz, the required matching is so critical that, it is proposed, all of the matching should be included as part of the MMIC packaging. It suggests first of all that, since the MMIC device has a printed circuit type of RF input and output, it should be mounted on a printed circuit substrate. To preserve the reproducible RF characteristics of the MMIC, a pair of matching transitions from the chip to the substrate is needed. While Figure 3 suggests a microstrip transmission line, the stripline or coplanar waveguide, for example, is also available.

One of the areas of MMIC packaging that will create a mismatch is the step change in the thickness of the chip and the substrate. The chip is typically 0.1 to 0.125 millimeters (mm), while the substrate may be 0.5 to 1.5 mm thick. The two factors that determine the thickness of the substrate are heat dissipation and structural integrity. Both factors tend to increase the thickness. The presence of via-hole grounding tends to make the chip thinner. Figure 3 suggests a tapered ground plane as one solution to eliminating the step change. Another solution is to use the coplanar waveguide, which does not require a ground plane. Both solutions, however, present some difficulties, and more studies on trade-offs are needed to develop the best transition.

Another area that must be considered in the chip-to-substrate transition is the step change in the dielectric constant. A GaAs MMIC may have a relative dielectric constant of 12.3, while a variety of substrates available may have relative dielectric

constants from 2.2 to 11.7. The material selected will most likely have the higher dielectric constant, unless there are thermal considerations. High-powered MMIC devices may require substrates with high thermal conductivities (such as boron nitride or berylium oxide, for example). The second half of this paper will present a more detailed analysis of step discontinuities.

Another consideration in the design of the module is that large gaps and long inductive leads must be avoided. In most cases, the MMIC device will be characterized on a network analyzer, which has waveguide or coaxial connectors. In addition, for many applications (such as an active array of horns, for example), the MMIC device may have to be mounted in a waveguide or coaxial module. It then becomes necessary to include a second pair of transitions to match the substrate to the waveguide or coaxial line. Figure 3 shows a typical solution using the Van Heuven² microstrip-to-waveguide transition. Other waveguide transitions are being used, such as the ridged waveguide and the stripline. Figure 4 shows the three typical transitions mentioned above.

Figure 3 shows pads for connecting DC and logic lines. These are proposed for inclusion as part of the delivered package. Clearly, the MMIC device will be mounted in 3 or 4 test jigs or modules between fabrication and its final application. A place where DC and logic lines can be disconnected and reconnected is needed.

Not shown in Figure 3, but an important consideration and inclusion, is the hermetic seal. A cover over the MMIC device of dielectric material (probably the same as the substrate) is needed to protect the chip from a humid or contaminated atmosphere. The cover must provide good isolation between the RF input and output lines.

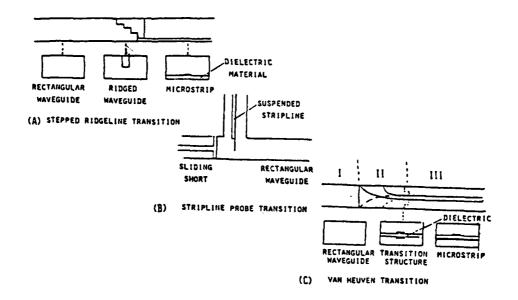


Figure 4. Typical substrate-to-waveguide transitions.

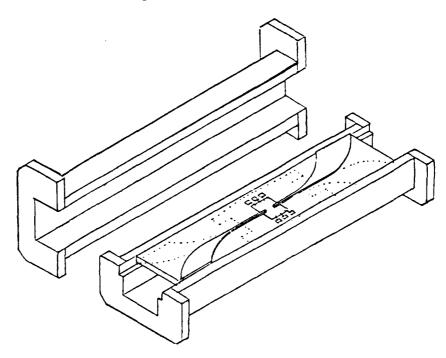


Figure 5. Typical MMIC environment.

In summary, the proposed MMIC package should include:

- Printed circuit substrate
- * Transition from chip to substrate
- * Transition from substrate to waveguide (or coaxial line)
- * Tapered ground plane
- * DC and logic line connection pads
- * Hermetic seal.

To be avoided or minimized are:

- * Step discontinuities
- * Large gaps
- * Long inductive leads.

Figure 5 shows that, having fabricated the MMIC package of Figure 3, it can be mounted in an easily fabricated housing. This housing can serve as a test jig as well as a module in an array antenna or any other waveguide circuit. When the MMIC package is mounted in the center of the waveguide, the waveguide is in the cut-off mode and the propagation is confined to the microstrip mode. The MMIC, therefore, can be easily installed into an identical environment at several test stations as well as its final operating location.

The University of Illinois and some in-house efforts at the NASA Lewis Research Center are expected to develop a data base on transitions and MMIC packaging. This data base can then be used by the MMIC industry, with some inputs of their own, to develop reproducible techniques for the characterization of MMIC devices.

The following sections describe a model for analyzing several transitions.

4. Introduction to the Analysis

In order to determine which of the various transitions shown in Figure 4 are most likely to fulfill the requirements outlined earlier in this paper, one would like to have the ability to analyze these configurations for insertion and return loss. If the S-parameters of these configurations can be determined, it should then be possible to design a configuration which has a relatively low insertion loss. The remainder of this paper will be devoted to developing the analytical tools one needs in order to characterize these transitions.

One problem that occurs with great frequency in the analysis of these transitions is an abrupt change in cross section of the printed circuit. An example of this is shown in Figure 6. In this figure, a fin-line is tapered in steps to become a rectangular waveguide. Thus, one may think of this transition as a succession of abrupt discontinuities in the printed circuit. If one can determine the S-parameters of each of these abrupt discontinuities, then it should be possible to cascade them together in a manner which will yield a low loss transition.

Abrupt printed circuit discontinuities may take a number of forms. The theory which is developed is general for many different types of discontinuities, as will be discussed later. For the present, however, it is necessary to begin by studying the most simple example of this discontinuity one can find. This turns out to be an abrupt change in the strip width of a shielded microstrip. A cross section of uniform shielded microstrip is shown in Figure 7, and a discontinuity in the strip width is shown in Figure 8. By studying this structure, it is hoped that the tools necessary to study a

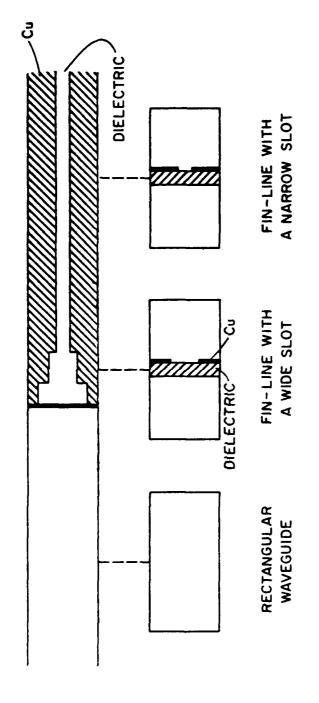


Figure 6. Transition between fin-line and rectangular waveguide.

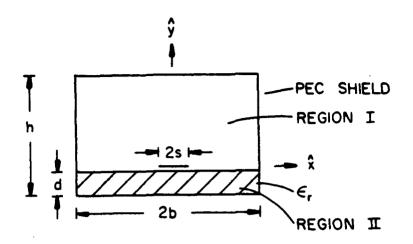


Figure 7. Cross section of shielded microstrip.

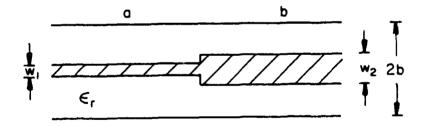


Figure 8. Top view of a discontinuity in the strip width on a microstrip.

more realistic transition, such as the fin-line stepped taper shown previously in Figure 1, will be developed.

The method to be used in the analysis of abrupt discontinuities involves mode matching in the plane of the discontinuity. In order to achieve this, one begins by generating the dominant and first few higher-order modes in each of the two microstrip lines. Next, one matches the tangential electric and magnetic field components in the plane of the discontinuity. Finally, one calculates the mode coefficients, which yield Sparameters and equivalent circuits of the discontinuity.

The study begins now with the analysis of the uniform microstrip.

5. Analysis of a Uniform Microstrip

The first step in the analysis of a uniform microstrip involves finding a Green's function which relates currents on the strip to the electric fields at all other points in the cross section of the line. This is accomplished by solving a two dimensional Helmholtz equation in regions I and II

$$\left(\nabla^2 + k_i^2\right) \begin{cases} \phi_i \\ \psi_i \end{cases} = 0 \tag{1.a}$$

$$k_i = \omega \sqrt{\mu_o \, \epsilon_i} \tag{1.b}$$

$$\epsilon_i = \begin{cases} \epsilon_i & x > 0 \\ \epsilon_i \epsilon_i, & x < 0 \end{cases}$$
 (1.c)

In the above equations, i denotes the region, and ϕ_i and ψ_i are the electric and magnetic scalar potentials in each region.

It is convenient to solve the above equation in the spectral domain, so one takes the Fourier transform of all potentials and fields as

$$\hat{\phi}(n,y) = \int_{-\infty}^{\infty} \phi(x,y) e^{j\alpha_n x} dx \qquad (2a)$$

$$\phi(x,y) = \frac{1}{2b} \sum_{-\infty}^{\infty} \overline{\phi}(n,y) e^{-j\alpha_n x}$$
 (2.b)

$$\alpha_n = \frac{n\pi}{b} \tag{2.c}$$

By matching boundary conditions on the shield walls and on the center conductor, one obtains an equation of the form

$$\begin{bmatrix} \widetilde{Z}_{zz}(\alpha_n,\beta) & \widetilde{Z}_{zx}(\alpha_n,\beta) \\ \widetilde{Z}_{xz}(\alpha_n,\beta) & \widetilde{Z}_{xx}(\alpha_n,\beta) \end{bmatrix} \begin{bmatrix} \widetilde{J}_z(\alpha_n) \\ \widetilde{J}_x(\alpha_n) \end{bmatrix} = \begin{bmatrix} \widetilde{E}_z(\alpha_n,\beta) \\ \widetilde{E}_x(\alpha_n,\beta) \end{bmatrix}$$
(3)

This equation relates the current in the plane y = 0 to the electric fields in this plane. The dyadic Green's function, $\widetilde{Z}_{ij}(\alpha_n,\beta)$, consists of relatively simple expressions in terms of hyperbolic sines and cosines.

Before proceeding to the solution of this equation for β , one should first look at the methods for generalizing the above Green's function. The above method is satisfactory for configurations with one dielectric layer and one strip. But a method developed by T. Itoh³ gives a technique for generating a Green's function for structures with an arbitrary number of dielectric layers and conducting strips. His technique is called the Spectral Immitance Approach. While a detailed explanation of the technique is beyond the scope of this paper, it may be stated that the the technique involves the separation of the fields in each dielectric region into TE_y and TM_y components in the spectral domain, and the subsequent formulation of analogous transmission lines in the \hat{y} direction for the decoupled TE and TM fields. This generalization extends the applicability of the techniques presented the this paper to a large class of printed

circuits.

Next, one must find the solution to the integral equation shown in Equation (3). The solution is effected by the spectral Galerkin technique⁴, in which a moment method solution is brought about in the spectral domain. Hence, the current on the strip is expanded in terms of basis functions, which are non-zero only on the strip, as

$$J_z(x) = \sum_{i=1}^{N} c_i \frac{\cos((i-1)\pi(x/s) - 1)}{\sqrt{1 - (x/s)^2}}$$
(4.a)

$$J_{x}(x) = \sum_{i=1}^{N} d_{i} \frac{\sin(i\pi(x/s) - 1)}{\sqrt{1 - (x/s)^{2}}}$$
(4.b)

One then takes the Fourier transform of these currents and substitutes the result into Equation (3). Next, the inner product of the resulting equation is taken with the individual basis functions, and Parseval's theorem is used to eliminate the right-hand side. The resulting matrix equation may be solved by setting the determinant equal to zero and solving for β with Newton's method.

The accuracy of this method is determined by the number of basis functions and the number of spectral terms one can calculate within a reasonable amount of computer time. For the dominant mode and lower-order evanescent modes, a small number of basis functions and spectral terms is probably satisfactory. For evanescent modes of larger order, it is likely that more basis functions and spectral terms are required to achieve reasonable accuracy.

Sample calculations were carried out in order to calculate the dominant and first two evanescent modes of microstrip. These results are shown in Figure 9. One would like to compare these modes to other results, but little data are available on microstrip modes. The microstrip mode calculations that are available deal with

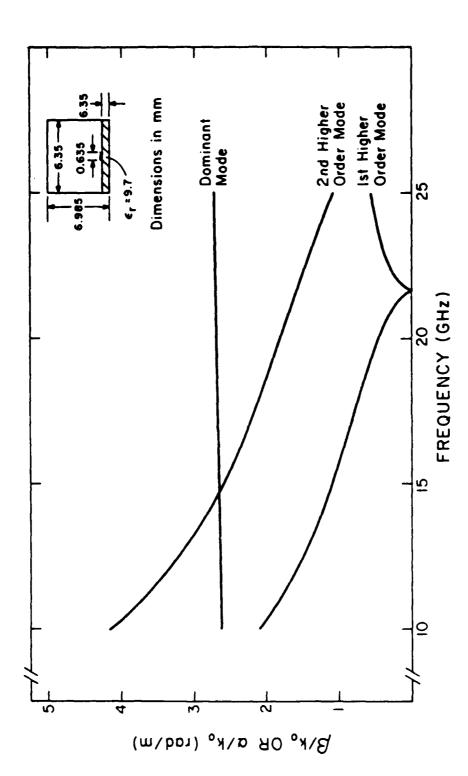


Figure 9. The dispersion characteristics of the dominant and first two even higher-order modes of microstrip. Two basis functions and 201 spectral terms were used.

propagating modes, but do not present data on evanescent modes^{5,6}. There does exist, however, one paper which presents calculations of fin-line for both propagating and evanescent modes⁷. In order to adapt our analysis to fin-line, we need only change the dyadic Green's function, \tilde{Z}_{ij} . This was done, and a dispersion curve was calculated, which is shown in Figure 10. Clearly, satisfactory agreement with the results in Reference 7 has been achieved. Since the microstrip calculation is quite similar to the fin-line calculation, it is believed that the microstrip mode calculations should also be reasonable.

Once the modes have been found and verified, the next step is to calculate the characteristic impedance of the uniform line. This is done for two reasons. First, it gives added confirmation that the dominant mode calculation is accurate. Second, it gives a first-order approximation to the input impedance at a discontinuity. This result is useful as a comparison for results obtained with the mode matching technique. Since the characteristic impedance is defined only for TEM lines, one must be careful to choose a definition of characteristic impedance which is useful experimentally. The definition most commonly chosen is the power-current definition

$$Z_o = \frac{2P}{II} \tag{5a}$$

$$P = \frac{1}{2} \operatorname{Re} \int \int E \times H' \, dx \, dy \tag{5.b}$$

$$I = \int_{-1}^{3} J_{z}(x) dx \tag{5.c}$$

An alternative definition is the voltage-current definition

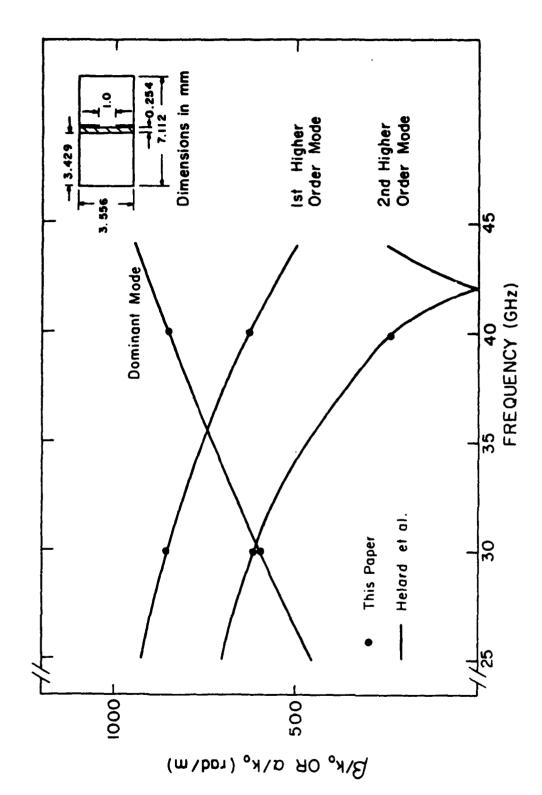


Figure 10. Dispersion curve of fin-line. Calculated with one basis function and 101 spetral terms.

$$Z_{o} = \frac{V}{I} \tag{6a}$$

$$V = -\int_{-d}^{0} E_{y}(y) \, dy \bigg|_{x=0}$$
 (6.b)

Calculations were performed with both of these definitions, and are plotted in Figure 11. They correspond very well with data already published in Reference 6.

6. Analysis of Discontinuities with Mode Matching

Among the techniques for studying waveguide discontinuities, mode matching seems one of the most promising⁸. This technique is suitable for calculating the characteristics of abrupt discontinuities, such as those in Figures 6 and 8. In addition, this method is easily adaptable to a cascade of abrupt discontinuities by using generalized S-parameters. Finally, it may be possible to model a smooth taper as a cascade of step discontinuities. Hence, the mode matching technique is capable of solving a wide variety of problems.

The mode matching technique begins by using the modes of the uniform microstrip calculated in the previous section. This involves finding the transverse fields for each mode and in each of the two waveguides,

$$\tilde{e}_{ia}(n,y) = \hat{e}_{xia}(n,y) \,\hat{x} + \tilde{e}_{yia}(n,y) \,\hat{y} \tag{7.a}$$

$$\bar{h}_{ia}(n,y) = \tilde{h}_{xia}(n,y) \,\hat{x} + \tilde{h}_{yia}(n,y) \,\hat{y} \tag{7.6}$$

where *i* denotes the mode number, and *a* denotes that we are referring to the input waveguide. Similar expressions hold for the output waveguide. At the point of the discontinuity, these transverse fields must be continuous. Enforcing this boundary

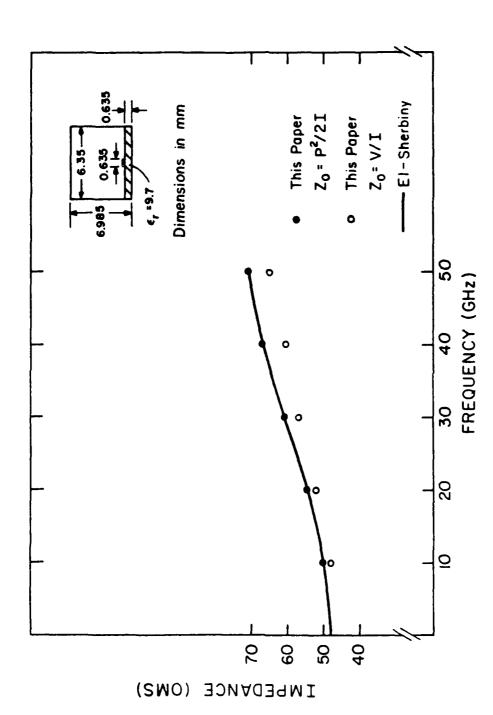


Figure 11. Characteristic impedance of microstrip using two definitions. Calculated with one basis function and 101 spectral terms.

condition, one obtains

$$(1+\rho) a_1 \bar{e}_{a_1} + \sum_{i=2}^{\infty} a_i \bar{e}_{ai} = \sum_{j=1}^{\infty} b_j \bar{e}_{bj}$$
 (8.a)

$$(1-\rho) a_1 \bar{h}_{a_1} - \sum_{i=2}^{\infty} a_i \bar{h}_{ai} = \sum_{j=1}^{\infty} b_j \bar{e}_{bj}$$
 (8.b)

where ρ is the reflection coefficient of the dominant mode, and a_i and b_j are the amplitudes of the modes in waveguides a and b, respectively. At this point, one takes appropriate inner products of Equation (8) and forms a matrix equation for ρ and for the mode coefficients a_i and b_j . Once these have been found, equivalent circuit parameters, Z_n and Y_n , are calculated as shown in Figure 12. The circuit has now been characterized completely.

When using the above method, it is necessary to find an alternate method of calculating the equivalent circuit parameters. This gives approximate values for Z_n and Y_n , against which one can compare the results derived from the mode matching technique. The only alternate method in the literature which treats this problem uses a static technique, which is valid only for lower frequencies. An example of this technique is shown in Reference 9. Therefore, a lower frequency case was chosen for the initial study, in order to be able to compare the results with other sources. If the validity of the mode matching technique can be demonstrated at lower frequencies, one may assume the technique is valid also at higher frequencies.

By calculating a low frequency case, one is able to compare the results for Z_n and Y_n to calculations made with other methods. In this case, Z_n is approximated by the normalized characteristic impedance of waveguide 2, relative to waveguide 1. The power-current definition of characteristic impedance is used, as shown in Equation (5).

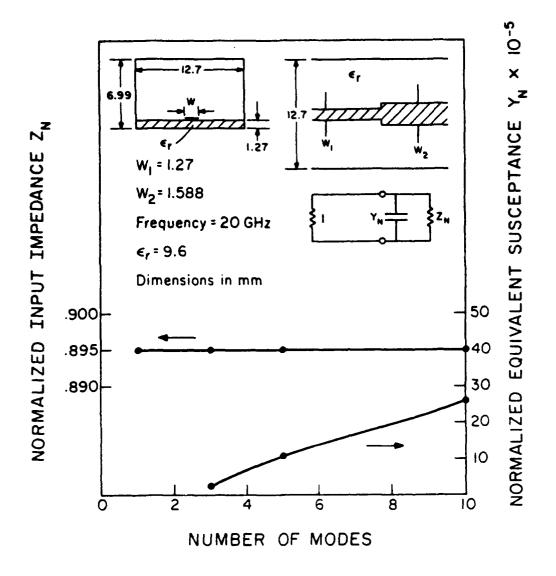


Figure 12. Variation of normalized impedance and normalized susceptance with the number of waveguide modes. Calculated with one basis function and 101 spectral terms. It is expected that $Z_n=0.985$ and $Y_n=128\times 10^{-5}$.

Furthermore, one can get an approximation to Y_n by referring to the junction capacitances calculated in Reference 12.

A sample case of a microstrip discontinuity calculation is shown in Figure 12. The equivalent circuit parameters, Z_n and Y_n , are plotted as a function of the number of waveguide modes used. The convergence of the normalized input impedance, Z_n , to its correct value has been demonstrated. The input admittance Y_n , however, seems to be dependent upon the number of modes used in each guide. It is necessary to get Y_n to converge in order to obtain the junction capacitance. It is likely that improved convergence of Y_n can be obtained by improving the efficiency of the inner product calculation, thus allowing the use of more modes in the mode matching technique.

There are many areas in this technique where additional study is needed. First, the sensitivity of the final answer to the number of spectral terms, the number of basis functions, and the number of modes used must be checked. Next, it is necessary to eliminate the dependency on the number of spectral terms used, by implementing an asymptotic form for the calculation of spectral terms of very large order. This change should reduce the computation time significantly. Finally, this technique should be applied to a variety of different structures such as those shown shown in Figures 4 and 6, and other structures useful in transitions between printed circuits and rectangular waveguides.

7. Concluding Remarks

Having been fabricated with lithographic techniques, the MMIC has inherently reproducible RF characteristics. In order to preserve the reproducibility of the MMIC and to be able to characterize MMIC devices with reproducible results, the following

considerations have been proposed: (1) mount the device on a printed circuit substrate; (2) provide an accurate transition from chip to substrate; (3) provide an accurate transition from substrate to waveguide; (4) eliminate discontinuities; (5) provide DC and logic connection pads; (6) provide a hermetic seal; and (7) include these in the delivered package. The importance of reproducible characterization by manufacturer and user was discussed.

A model for analyzing several types of transitions was described. The model involved the breakdown of transitions into a cascade of abrupt printed circuit discontinuities, whose S-parameters were determined with mode matching techniques. The initial results presented in this report demonstrate the method to be a promising one.

References

- 1. Smetana, J. (1982) Application of MMIC modules in future multiple beam satellite antenna systems, NASA Technical Memorandum 83344.
- 2. Van Heuven, J. H. C. (1976) A new integrated waveguide-microstrip transition, *IEEE Trans. Microwave Theory Tech.*, MTT-24:144-147.
- 3. Itoh, T. (1980) Spectral domain immitance approach for dispersion characteristics of generalized printed transmission lines, *IEEE Trans. Microwave Theory Tech.*, MTT-28:733-736.
- 4. Schmidt, L. and Itoh, T. (1980) Spectral domain analysis of dominant and higher order modes in fin-lines, *IEEE Trans. Microwave Theory Tech.*, MTT-28:981-985.
- 5. Mirshekar, D. and Davies, J. B. (1980) Accurate solution of microstrip and coplanar structures for dispersion and for dielectric and conductor losses, *IEEE Trans. Microwave Theory Tech.*, MTT-27:694-699.
- 6. El-Sherbiny, A. A. (1981) Accurate analysis of shielded microstrip lines and bilateral fin-lines, *IEEE Trans. Microwave Theory Tech.*, MTT-29:669-675.
- 7. Helard, M. et. al. (1983) Exact calculations of scattering parameters of a step slot width discontinuity in a unilateral fin-line, *Electron. Lett.*, 19:537-539.
- 8. El-Hennaway, H. and Schuneman, K. (1983) Impedance transformation in finlines, *IEE Proc.*, 129:342-350.
- 9. Horton, R. (1973) Equivalent representation of an abrupt impedance step in microstrip line, *IEEE Trans. Microwave Theory Tech.*, MTT-21:562-564.

WAVEGUIDE SLOT ARRAY WITH CSC² e · COS e PATTERN

John J. Erlinger and Jeffrey R. Orlow Rantec Division Emerson Electric Co. Calabasas, California

ABSTRACT

A planar array of longitudinal shunt slots in rectangular waveguides has been designed to produce a ${\rm CSC}^2~\Theta$ - ${\rm COS}~\Theta$ pattern in the E-plane and -22-dB side lobes in the H-plane. The array operates at 15 GHz.

The choice of E-plane amplitude and phase distribution, to synthesize the CSC^2 Θ • COS Θ pattern shape over the sector 8° to 50° below broadside, involved a tradeoff study. The widely used Woodward approach of superimposing a family of uniform-amplitude/uniform-progressive-phase distributions on the aperture was studied but not used in preference to a technique reported by Elliott of perturbing the roots on a Schelkunoff unit circle to obtain the desired pattern shape. Twelve roots were perturbed in a systematic way to obtain an optimum amplitude distribution with accompanying phase angles.

This paper also describes a method used to spread the resultant E-plane distribution and the H-plane Taylor distribution over a circular aperture. The mutual coupling between elements was taken into account for the design. The predicted results show good agreement with measurements.

1.0 INTRODUCTION

The typical antenna to be used for ground mapping by an airborne radar has a narrow beam in the azimuth plane, but a $CSC^2\theta$ shaped beam in elevation with θ being the angle below the aircraft axis. The ideal pattern shape, considering the display of range traces has been found to be $CSC^2\theta$. COS θ with the extent of the shaped pattern in θ space determined by the aircraft altitude and specific mapping requirements. A shaped cylindrical reflector fed by a line source, or a shaped dish fed by a point source is often used for this application with the shaping accomplished using geometrical optics. This paper discusses the design of a planar array used in place of a shaped dish with a point source feed. The major advantage of the planar array is its thin profile and lower swept volume.

The particular application required a $CSC^2 \odot \cdot COS \odot$ pattern from 8° to 50° below the aircraft axis (Figure 1) in the elevation plane (E-plane); the azimuth pattern through the beam peak was to have a 3-dB beamwidth less than 2.8° and side lobes below -22 dB. The operational frequency was 15-GHZ.

This paper discusses the method used to:

- Synthesize the CSC² ⊕ COS ⊕ pattern shape;
- Determine the total aperture distribution;
- Obtain the desired amplitude and phase on each of the radiating elements.

Test results are included for partial and full-up arrays.

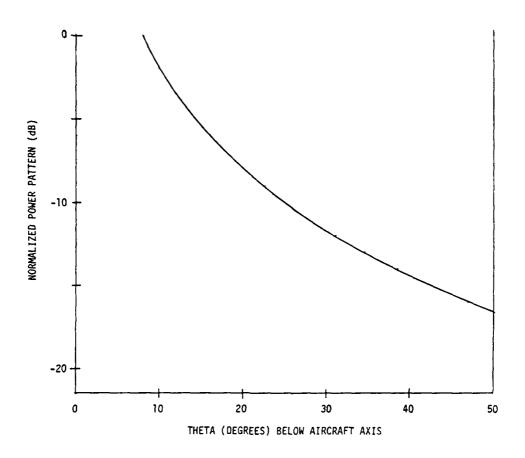


Figure 1. Desired CSC 2 θ \cdot COS θ Power Pattern

2.0 TYPE OF ARRAY

Past experience in the design and fabrication of resonant waveguide slot arrays using shunt slots in the broad wall of each radiating waveguide for pencil beam applications led quite naturally to the use of a similar concept for the ${\rm CSC}^2$ Θ • COS Θ ground-map antenna. Figure 2 is a front-view of one-half of the array. The available 21.5-inch diameter has been filled to achieve the desired 2.8-degree azimuth beamwidth and maximum possible directivity. The left and right halves of the array are fed separately; a short circuit runs vertically down the centerline of the array separating the left and right halves of each radiating waveguide. Each of the 35 radiating waveguides in one half of the array contains 7 to 18 offset shunt slots resonantly spaced $\lambda_0/2$ apart. The input to each radiating quide is a transverse slot fed as shown in Figure 3. This slot is between the radiating waveguide (level one) and the level-two phasing waveguide which consists of a length of 0.529-inch wide waveguide transforming to 0.440-inch width at the appropriate distance from the transverse slot to achieve the required relative phase between radiating waveguides. This phasing section is capable of 180° phase shift. The phasing network of level 2 is fed by the inclined series slots which are in the bottom wall of a 0.636-inch-wide waveguide on level 3 behind the radiating face. This 0.636-inch waveguide has the inclined series slots non-resonantly spaced about 201° apart and runs the

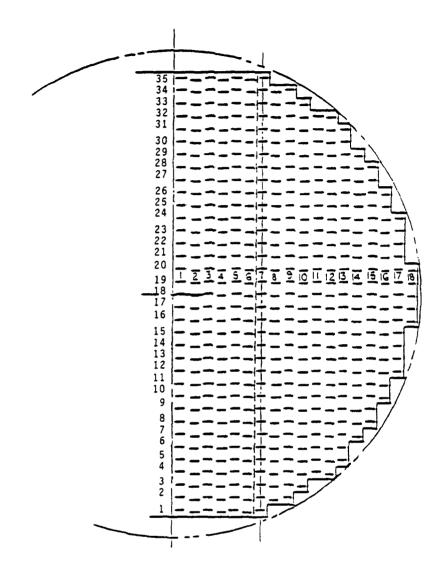


Figure 2. Array Assembly Front View

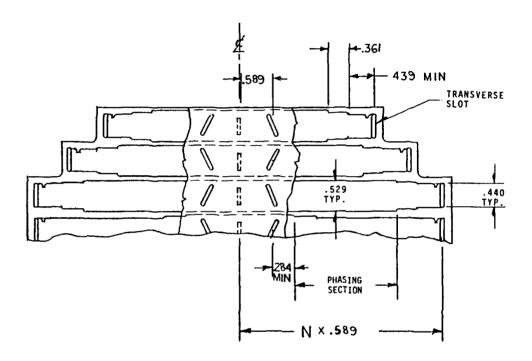


Figure 3. Phasing Network - Level 2

full length of the array with the input at the top and a termination at the bottom end of the array.

The spacing of the inclined series feed slots as shown in Figure 3 will result in 21° of progressive phase from one slot to another. Tilting the slot the opposite direction from that shown results in 180° of phase shift. This 180° together with the 180° available from the phasing section gives full 360 degree adjustment capability to achieve the required phase shift in the radiating waveguide. The impedance change from 0.529 to 0.440 inch wide waveguide in the phasing section is matched by a single-section quarter-wave transformer. The transverse slot between this section and the radiating waveguide is a 1:4 transformer between the 0.440-inch-wide waveguide impedance and the sum of the active admittances of the radiating waveguide.

As will be seen in succeeding sections of this paper, the array size was reduced from 35 x 36 elements to 26 x 36 as a result of aperture distribution considerations for the ${\rm CSC}^2$ Θ • COS Θ E-plane pattern, and finally to 26 x 34 based on the inability to obtain the desired phase in the outside columns.

3.0 SHAPED PATTERN SYNTHESIS

3.1 Woodward Pattern Synthesis

Two methods were investigated to determine the E-plane aperture distribution required to achieve the desired $CSC^2 \odot \cdot COS$ \odot shaped pattern in this plane. The first of these was suggested

by Woodward in $1947^{[1]}$. He stated that the pattern F(u) of a continuous line source of length 2a could be represented as the sum of N patterns in the form:

$$F(u) = \sum_{n=0}^{N} K_n \frac{\sin[\pi(u-n)]}{\pi(u-n)}$$
 (1)

where u is defined by:

$$u = \frac{2a}{\lambda} [\cos (90-\Theta) - \cos (90-\Theta)_{0}]$$
 (2)

with $(90-\Theta_0)$ being the pointing angle from endfire of the zeroth pattern. Each of the N patterns can be recognized as being produced by an array with uniform amplitude K_n having a uniform phase. Observing that the angle u=1 in (1) is both the first null of the n=0 pattern and the peak of the n=1 pattern, and likewise the angle u=2 is both the first null of the n=1 pattern and the peak of the n=2 pattern, it thereby becomes possible to individually determine the amplitudes K_n so that the main-beam peaks of each of the N patterns lie on the desired envelope to give null filling. This Woodward method can also be applied to a uniformly spaced linear array of discrete elements. As is seen in Figure 4, this method is applied to shaping the desired beam from Θ =-4° to Θ =38°. The peak was moved above broadside by 4° with the proviso that the antenna be tilted downward 12° to achieve the 8- to 50-degree

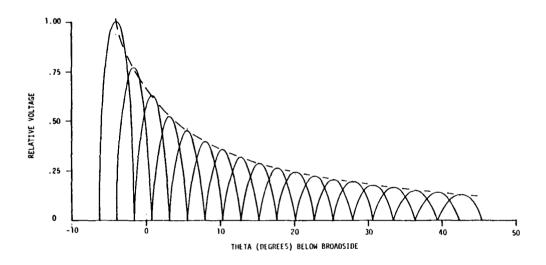
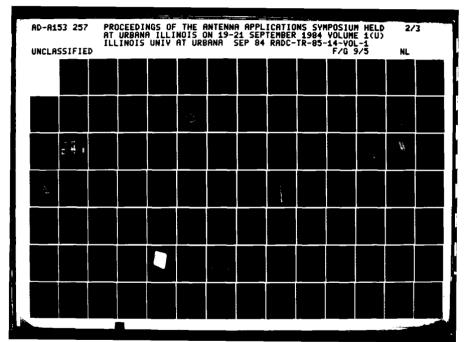


Figure 4. Nineteen Beams Used for Woodward Synthesis

shaped beam below the aircraft axis. Nineteen patterns are required to achieve the null filling over the 42° shaped-beam region. To avoid confusion, side lobes are not shown in Figure 4.

The required amplitude and phase distribution for each of the 35 elements is plotted in Figure 5. The amplitude distribution for the array is symmetrical about the centerline of the array with the elements above and below centerline being complex conjugates of one another. The amplitude curve shows that only 5 of the 35 elements in the vertical plane have amplitudes in the 0- to -10-dB range, a rather inefficient use of the aperture. quently, in the interest of having a shorter array, a study was made to determine how rapidly the antenna directivity dropped as radiating waveguides were removed from the top and bottom of the array. As seen in Figure 6, the directivity degraded very slowly for a shaped-beam antenna as the circular aperture was reduced in the shaped-beam plane. Reducing the aperture size in the E-plane would reduce weight and manufacturing complexity at a very small sacrifice in gain. Another reason for considering a smaller aperture was in the interest of reducing the amplitude taper in the Eplane somewhat below the -20.9 dB required for the Woodward distribution of Figure 4. Reducing the aperture height from 35 elements to 26 elements resulted in only 0.1 dB loss in directivity and changed the aperture amplitude distribution to that shown in Figure 7. Cutting down the aperture resulted in lowering the





MICROCOPY RESOLUTION TEST CHART NATIONAL BUREAU OF STANDARDS-1963-A

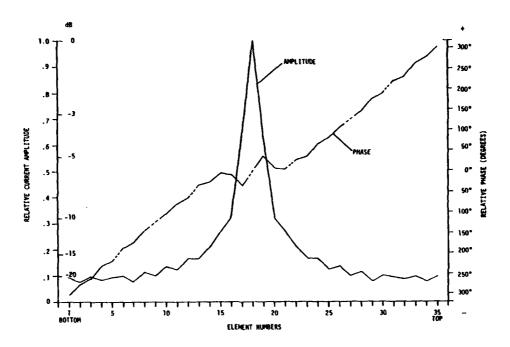


Figure 5. Amplitude and Phase for 35-Element Woodward Distribution

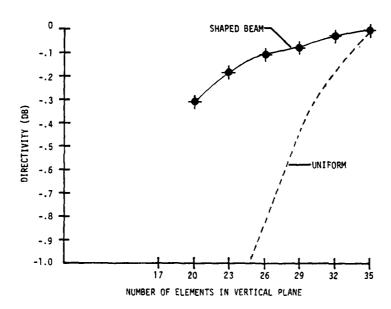


Figure 6. Antenna Directivity vs Number of Elements in the Vertical Plane

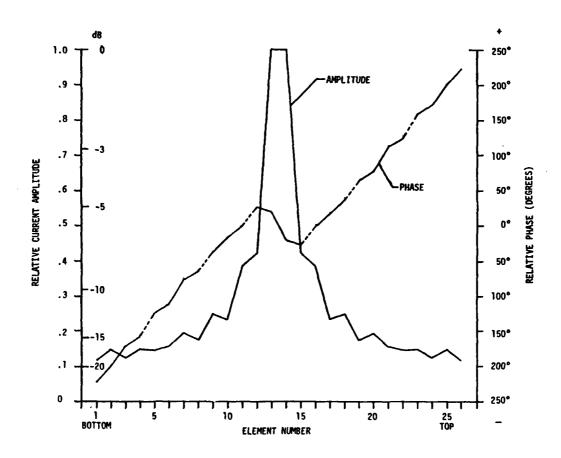


Figure 7. Amplitude and Phase for 26-Element Woodward Distribution

amplitude extremes only slightly to 18.5 dB versus 20.9 dB for the 35-element aperture. The 26-element E-plane aperture is shown in Figure 8. The outer 6-elements in the H-plane are shown with phantom lines since these elements were planned for the array but had to be eliminated for the reasons to be discussed in Section 4.0.

The peaked amplitude distribution given by the Woodward synthesis creates a very difficult feeding problem in that the center two elements in the array have nearly 60% of the power with the next two on both sides of center having about 12% and 8%, respectively, of the total power. The other 20 to 29 elements for the 26 and 35 element arrays, respectively, have only a total of about 20% of the power; the individual elements have 3.5% down to 0.7%. This power distribution cannot be achieved with sufficient accuracy by feeding from the top of the array with a traveling wave feed of inclined series slots.

In summary, the Woodward synthesis technique results in a unique amplitude and phase distribution for a given antenna pattern. The amplitude distribution is peaked at the center of the aperture, falling off very rapidly with the elements adjacent to the center pair already down 7 dB. It is a rather inefficient use of the aperture, resulting in aperture distributions nearly impossible to realize in practice because of the very low edge illumination (-18 to -21 dB). In the interest of finding an aperture distribution with a more uniform amplitude distribution, a procedure developed by Elliott^[2] was employed.

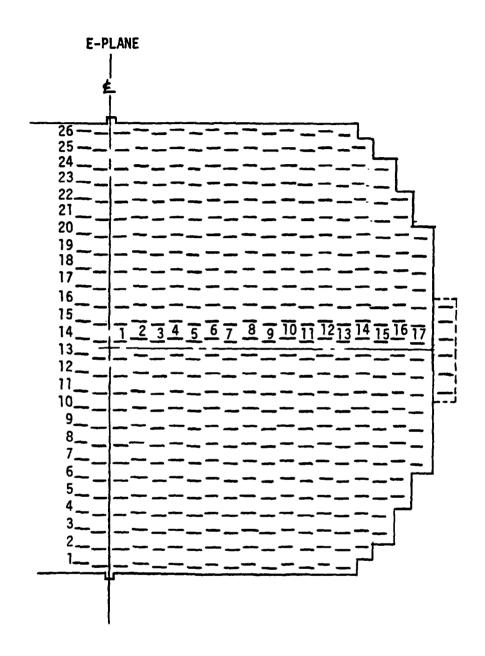


Figure 8. Front View of Array with 26 Elements in E-Plane

3.2 Elliott Pattern Synthesis

The pattern-synthesis method developed by Elliott begins with the Taylor synthesis of a sum pattern in which the height of every side lobe is individually specified [3] (see Figure 9a). In the shaped region the peaks of the main beam and the side lobes are adjusted to follow the prescribed CSC^2 θ · COS θ shaped envelope. For this case, the amplitude of the main beam and 12 side lobes were adjusted to conform to the CSC^2 θ · COS θ shape. Outside this shaped region the peaks of the lobes were adjusted to follow the side lobe falloff from a uniform aperture distribution. Since the elements are spaced greater than 0.5λ $(0.71\lambda$ for this case), the pattern begins to repeat itself when the traverse around a Schelkunoff unit circle exceeds one revolution.

After this, the roots on the Schelkunoff unit circle which lie in the shaped-beam region were displaced radially the proper amount to give null filling to the level of the envelope. Minor adjustments were then made to achieve a balanced ripple and to restore the desired side lobe typography in the nonshaped region since this was slightly disturbed by the root displacements in the shaped region. The final pattern is shown in Figure 9b.

This pattern synthesis technique had several advantages over the Woodward method. It allowed for control of the side lobe typography in the nonshaped region. Even more importantly, it offered 2^{12} distinct current distributions, all of which produced

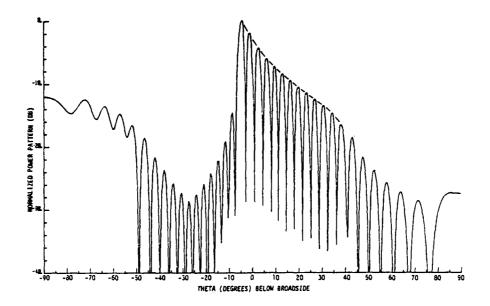


Figure 9a. Starting Pattern for 26-Element Shaped Beam Synthesis

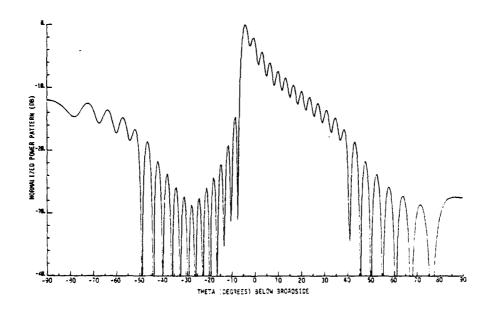


Figure 9b. Final Pattern for 26-Element Shaped Beam Synthesis

the same pattern since 12 roots were displaced radially on the Schelkunoff unit circle, and it didn't matter whether they were moved inward or outward.

Using this pattern synthesis method, 4096 different current distributions were possible. A computer search was made for the current distribution with the least amplitude variation across the aperture. The selected distribution is in Figure 10. The amplitude varies by only 9.5 dB across the aperture; it is peaked near the top of the array, making the distribution ideal for a traveling-wave feed.

4.0 H-PLANE APERTURE DISTRIBUTION

A 25-dB, n=5 Taylor linear distribution was selected for the H-plane to meet the 22-dB side lobe requirement. The H-plane aperture width could contain 36 slots within the 21.5-inch allowed diameter as was seen in Figure 2. When the elements in each of 36 vertical columns are added together for calculation of the H-plane pattern, each column must add to the amplitude required for the 25-dB Taylor distribution with each of the phase angles being the same since constant phase across the aperture is a requisite for realizing the Taylor patterns.

5.0 TOTAL APERTURE DISTRIBUTION -- MUTUAL COUPLING

The individual E- and H-plane aperture distributions were discussed in sections 3.0 and 4.0 respectively. The E-plane

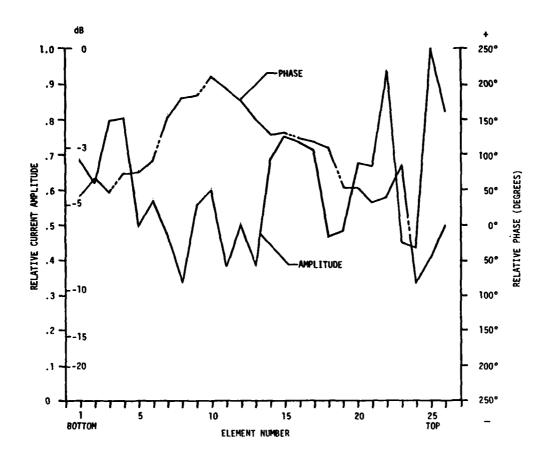


Figure 10. Amplitude and Phase for 26-Element Elliott Distribution

distribution consists of 26 discrete phasors varying wildly in both amplitude and phase (Figure 10). The H-plane is a constant-phase amplitude-tapered distribution which has been discretized for the 36 radiating slots. Thus the E- and H-plane distributions have been uniquely defined; however, the distribution in any plane between these two is not uniquely defined but at the discretion of the designer. The desired distribution would result in smooth pattern transition from the CSC^2 Θ • COS Θ in the E-plane to 25-dB Taylor in the H-plane.

For a waveguide slot array with 26 horizontal waveguides, each fed by an inclined series slot, it should be noted that each of the waveguides will radiate with uniform phase throughout its length. Each waveguide is a linear standing-wave array of $\lambda_g/2$ -spaced slots with the amplitude from each slot determined by its offset and the phase determined by the input to the array from the inclined series slot as modified by the phasing section. For example, referring to Figure 10, each of 26 slots in the top row of the array (row 26) has the relative phase of 0°, each of 36 slots in the tenth row from the bottom has the relative phase of 210.87°, and so on. This constant-phase per row is an important consideration in attempting to spread the E- and H-plane collapsed distributions throughout the aperture.

For a rectangular aperture, the amplitude distribution for each of the 26 waveguides would be 25-dB Taylor discretized over

the 36 elements in each row. For a modified circular aperture, the number of slots in each waveguide varies from 26 to 36; a 25dB Taylor distribution from each waveguide will not result in an overall 25-dB Taylor distribution in the H-plane. Consequently, the spread was done manually with three goals in mind. (1) The sum of the currents in each row must total the amplitude needed in that row to produce the ${\rm CSC}^2$ Θ • COS Θ pattern. These amplitudes are as in Figure 10. (2) The sum of the phasors in each of the 36 columns must be as close as possible to constant phase with the amplitude taper as required for the 25-dB side lobe pattern in the H-plane. (3) The spreading should be as smooth as possible in both the rows and columns. Goal number 3 is difficult in light of the fact that the required E-plane voltage amplitude distribution varied by more than 2:1 between adjacent elements, e.g., elements 24 and 25 are 53.0 and 121.8 in relative amplitude.

The manual spreading of the distribution resulted in typical phase angles of 88° for the summation of the elements in columns 1 through 13. It quickly became obvious that the 18th columns on both sides of centerline (each with 6 elements) could not be excited such that the phase angle of the summed current will be close to 88° since the phase angle for each of the six elements is between 121.45° and 193.33°. Consequently, these two outer columns were deleted from the array producing the final array size of 26 x 34 elements (Figure 8).

The total-aperture distribution was done so that the collapsed E-plane distribution precisely matches the desired distribution in Figure 10 for the ${\rm CSC}^2$ θ • COS θ pattern. The collapsed H-plane amplitude is within 3% of that desired for the Taylor distribution; the phase varies over the 14th through 17th columns by as much as 28° from being uniform. This phase deviation for the outer elements results in the pattern of Figure 11; it is still very acceptable. As will be discussed in the following paragraphs, the mutual coupling between elements required changing many of the individual element amplitudes from those originally selected to achieve a realizable design.

The offsets and lengths for each of the 832 slots were determined with account taken of external mutual coupling by using the design procedure formulated by Elliott ^[4] together with measured curves of slot conductance and slot susceptance versus resonant length (Figure 12). The curves in Figures 12 are for a single slot isolated in a ground plane. Additional data on slot conductance versus offset was also used.

A starting point for this design procedure was a selected offset and length for each slot, <u>e.g.</u>, .040-inch offset and $\lambda_{\rm g}/2$ length. Using the desired slot voltage distribution, the computation was made of the mutual-coupling contribution from each of the 416 slots in one half of the array (assuming symmetry about the vertical centerline) to each slot. The offset and length of

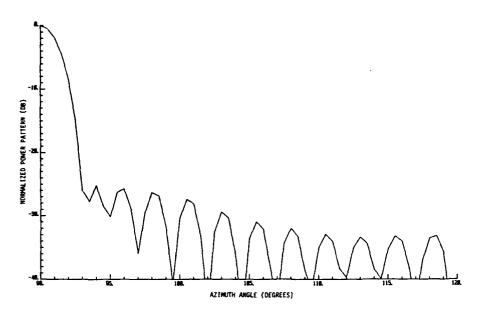


Figure 11. Calculated H-Plane Pattern for Initial Aperture Distribution

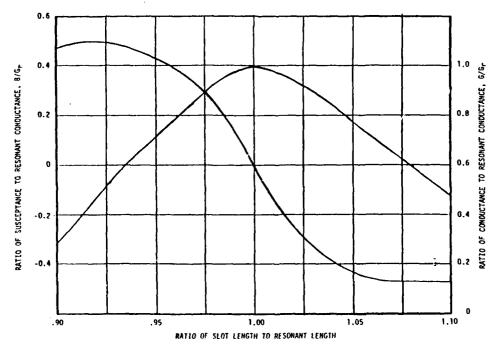


Figure 12. Normalize Self-Admittance Components for Longitudinal Shunt Slot

each slot was then adjusted to satisfy Elliott's two design equations such that the active admittance of each slot is real and the sum of the normalized active admittances in each radiating waveguide section is 4.0 for this array. This procedure was iterated because the calculated offsets and lengths did not agree with the original guess. It was necessary to cycle through this procedure of recomputing the mutual-coupling contribution to each slot and then the new offsets and lengths until the offsets and lengths for two successive iterations were within machining tolerances.

This procedure will converge quite readily for a uniform-phase pencil-beam array. However, with the wild variations in amplitude and phase across the aperture required to achieve the shaped beam, convergence becomes more difficult. A negative limit of -0.5 for the real part of the mutual coupling was set to make sure that the resultant slot admittance was positive. The imaginary part of the mutual coupling term is cancelled by making the slot length nonresonant. The limits for this term are imposed by the shape of the B/G_{0} versus L/L_{R} curve in Figure 12; the curve flattens out beyond the region -.30 < B < .32. Consequently the imaginary part of the mutual coupling term was limited to be in the range -0.32 to 0.3 to ensure that the procedure converged. The original aperture distribution was modified as the mutual coupling calculations progressed to bring the mutual coupling term

within these limits. Generally, this involved raising the voltage of an element that fell out of bounds, and then subtracting this voltage from several elements in the same row so that the distribution for the E-plane shaped beam was unchanged at the expense of a degraded H-plane distribution. The final iteration resulted in the E-plane aperture distribution precisely matching that required for the CSC^2 Θ COS Θ pattern of Figure 9b. The H-plane distribution still predicted a good -25 dB H-plane pattern comparable to that shown in Figure 11.

6.0 HARDWARE TEST RESULTS

Two separate arrays were designed, built, and tested. The first was a rectangular array 26 elements high to demonstrate the shaped beam, and 6 elements wide with a uniform H-plane distribution (Figure 13). This array served the purpose of validating the feed/phase-shifter design and the mutual coupling calculations. This array differed in concept from that described in section 2.0 in that each of the 26 radiating waveguides was end fed with the summation of the active admittances for each 6-slot waveguide equal to 1.0 + j0. Thus, with reference to Figure 3, the phasing section was moved up to level 1 and the 0.440-inch width was transformed back up to 0.529 inches and directly into the section of waveguide with the six radiating slots followed by a short circuit. The E- and H-plane patterns are shown in Figure 14.

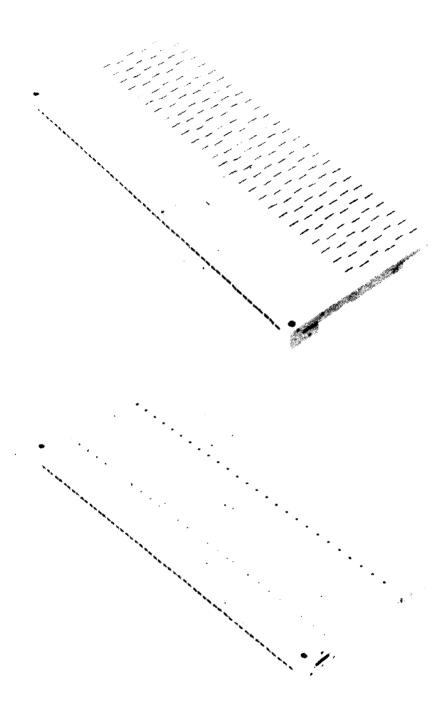


Figure 13. Front and Rear View of 26 \times 6 Array

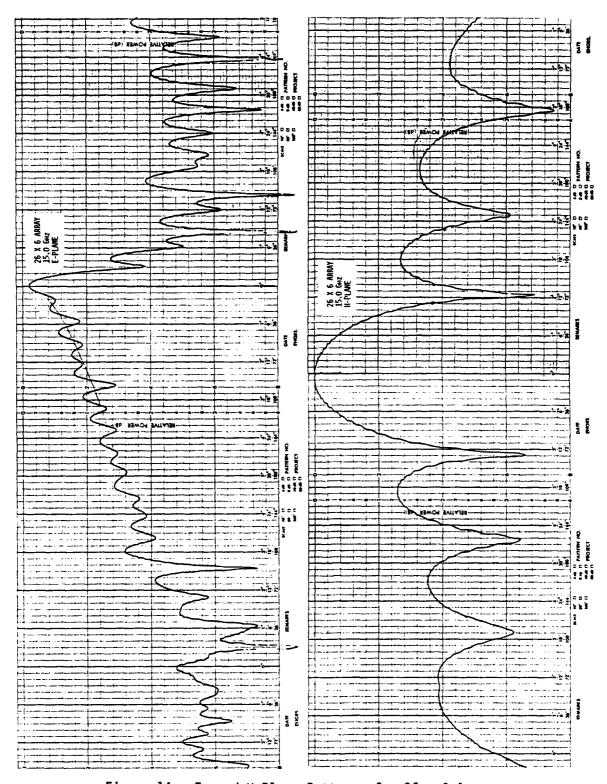


Figure 14. E- and H-Plane Patterns for 26 x 6 Array

They both agree very well with the theoretical patterns. It should be noted that these test results were taken on the asfabricated antenna. No tuning was done.

The full-up modified-circular 26 x 34 element array was then built (Figure 15). For this array, the summation of the active admittance equals 4.0 + j0 for each radiating waveguide and the impedance match between the phasing section and the radiating waveguide is accomplished by the transverse slot. The test results, without any tuning, are shown in Figure 16. These measured patterns agree well with the theoretical patterns but with some degradation in the ripple level. The 4-to-1 impedance transformation and probable inaccuracies in the 4.0 + j0 admittance value coupled with the changes introduced by these impedance mismatches on the phasing section and feed-slot coupling have resulted in increased pattern ripple.

7.0 CONCLUSIONS

A procedure has been developed for the design of a CSC² 0 • COS 0 shaped-beam planar-array antenna using a pattern synthesis technique that gives a physically realizable aperture distribution. A method was devised for blending the shaped beam distribution in the E-plane into a 25 -dB Taylor distribution in the H-plane over a circular aperture. Account was taken of mutual coupling between elements in the aperture. An end-fed rectangular array

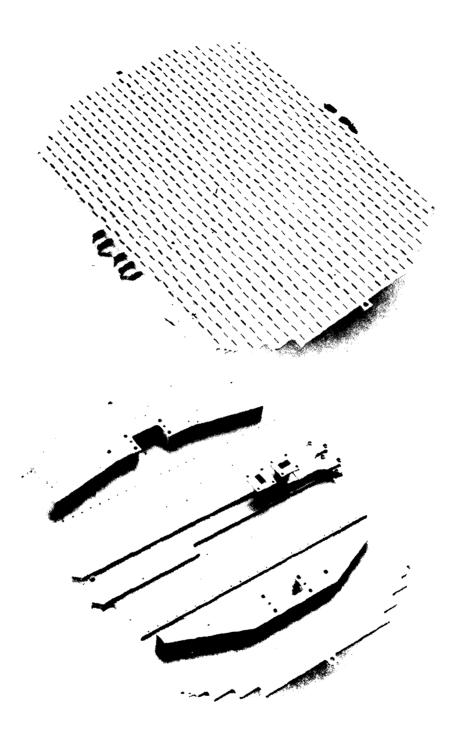
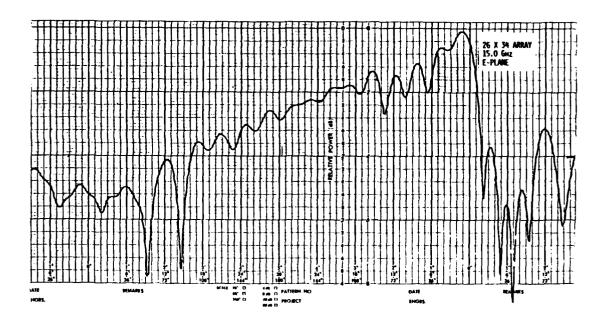


Figure 15. Front and Rear View of 26 x 34 Array



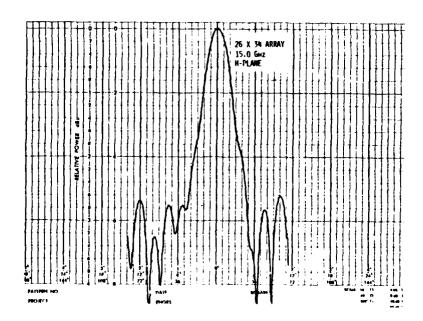


Figure 16. E- and H-Plane Patterns for 26 x 34 Array

and a circular array were both built and tested. Good agreement was demonstrated between the measured and expected results.

REFERENCES

- Woodward, P. M. (1947) A method of calculating the field over a plane aperture required to produce a given polar diagram, J.I.E.E., pt. IIIA, 93:1554-1558.
- Elliott, R. S. (1982) Improved pattern synthesis for equispaced linear arrays, <u>Alta Frequenza</u>, 51:296-300.
- 3. Elliott, R. S. (1981) <u>Antenna Theory and Design</u>,
 Prentice-Hall Publishing Co., Englewood Cliffs, New
 Jersey, Chapter 5.
- 4. Elliott, R. S. (1983) An improved design procedure for small arrays of shunt slots, <u>IEEE Transactions on</u> <u>Antennas and Propagation AP-31 (No. 1):48-53.</u>

SHEET METAL WAVEGUIDE FORMING TECHNIQUE

P.K. PARK AND S.E. BRADSHAW

HUGHES MISSILE SYSTEMS GROUP, CANOGA PARK, CA

ABSTRACT

A 30 element shunt slot array (30 db sidelobes, x-band) was designed analytically and fabricated by a sheet metal waveguide forming technique. This technique starts with a ten mil copper sheet which is then photo-etched completely through for slots and half way through (5 mils) for bend lines. Then this photo etched copper sheet is bent into waveguide with a couple of simple mandrels. The last procedure is to apply solder paste to the seams and heat in an oven.

The analytic design process adjusts the slot length and offset of each slot while including the effect of external mutual coupling until the desired aperture distribution and impedance match are achieved. Tested results show that the cost effective sheet metal waveguide forming technique is a viable technique.

30 db Sidelobe Shunt Slot Array Design

A design theory for small slot arrays has been described by Elliott and Kurtz [1][2][3] in which, for a given aperture distribution and match, the length and offset of each slot in the array can be claculated in the presence of mutual coupling. As indicated in [1], when significant mutual coupling is present, the self admittances required in small array design will be primarily associated with non resonant slot lengths. Therefore, the complex self-admittances of rectangular shunt slots in waveguide were evaluated by the moment method and curve fitted for use in the design program shown in Figure 1. Low cost mutual expression [4] was used in this design. The summary of the 30 element array (30 db Chebyscheff sidelobe taper) design is tabulated in Table 1.

Sheet Metal Waveguide Forming Technique

This technique starts with a ten mil copper sheet which is then photo etched completely through for slots and half way through (5 mils) for bend lines as shown in Figure 2. Better registration of the series/ series coupling slot relative to the radiating shunt slots was obtained by etching them on the same sheet. Then this photo etched copper sheet is bent into waveguide with a couple of simple mandrels as shown in Figure 3. The last procedure is to apply solder paste to the seams and heat in an oven. Special mandrel in Figure 3 was used to hold those waveguides together while they are in an oven. The 30 element array formed by this technique is shown in Figure 4.

The E-plane and H-plane patterns are shown in Figure 5. Tested results show that the cost effective sheet metal forming technique is a viable technique. This sheet metal waveguide forming technique can be extended to any type of sheet metal provided there is welder for the corresponding metal.

References

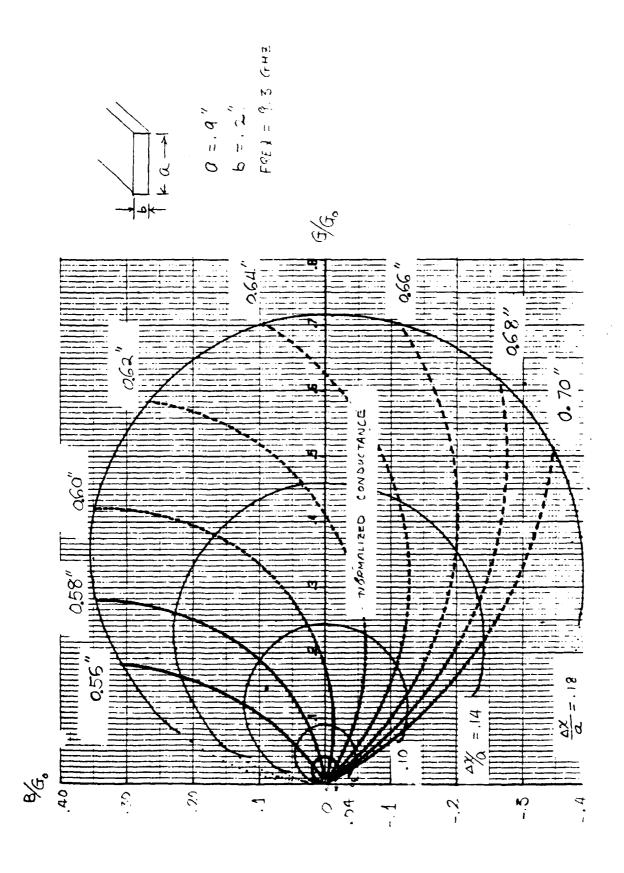
- R. S. Elliott, "An improved design procedure for small arrays of shunt slots," IEE Trans. on Ant and Propagat., vol. AP-31 No.1 Jan. 1983 pp 48-53.
- R. S. Elliott and L. A. Kurtz, "The design of small slot arrays,"
 IEEE Trans on Ant. and Propagat. vol. AP-26 No. 2, March 1978
 pp 214-219.
- 3. C. W. Westerman, V. L. Harrington and P. K. Park, "Analytic design of conformal slot arrays," IEEE Trans on Ant. and Propagat., vol. AP-31, No. 4, July 1983.
- 4. P. K. Park, "Mutual Admittance between Slots on a plane," 1984

 IEEE International Symposium Digest Vol. 1, pp 393-396.

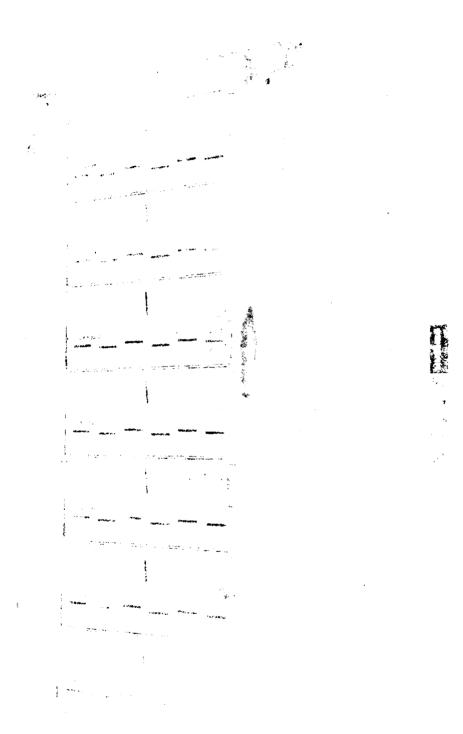
TABLE 1. SUMMARY OF 30 ELEMENT ARRAY DESIGN

SLOT SLOT SLOT SUM ADMITTANCE SUM ADM
1 1 0.025 0.625 0.094 0.094+J 0.000 0.046+J 0.000 0.015+J=0.00 2 1 -0.070 0.622 0.218 0.218+J 0.000 0.297+J 0.000 0.138+J=0.04 3 1 0.099 0.652 0.319 0.319+J 0.000 0.630+J 0.000 0.227+J=0.12 4 1 -0.108 0.639 0.319 0.319+J 0.000 0.675+J 0.000 0.323+J=0.08 5 1 0.064 0.635 0.218 0.218+J 0.000 0.276+J 0.000 0.097+J=0.05
2 1 -0.070 0.622 0.218 0.218+J 0.000 0.297+J 0.000 0.138+J-0.04 3 1 0.099 0.652 0.319 0.319+J 0.000 0.630+J 0.000 0.227+J-0.12 4 1 -0.108 6.639 0.319 0.319+J 0.000 0.675+J 0.000 0.323+J-0.08 5 1 0.064 0.635 0.218 0.218+J 0.000 0.276+J 0.000 0.097+J-0.05
3 1 0.099 0.652 0.319 0.319+J 0.000 0.630+J 0.000 0.227+J-0.12 4 1 -0.108 6.639 0.319 0.319+J 0.000 0.675+J 0.000 0.323+J-0.08 5 1 0.064 0.635 0.218 0.218+J 0.000 0.276+J 0.000 0.097+J-0.05
4 1 -0.108 6.639 0.319 0.319+J 0.000 0.675+J 0.000 0.323+J-0.08 5 1 0.064 0.635 0.218 0.218+J 0.000 0.276+J 0.000 0.097+J-0.05
5 1 0.064 0.635 0.218 0.218+J 0.000 0.276+J 0.000 0.097+J-0.05
- 6 1 -0 000 0 114 0 004 0 004+10 000 0 053+10 000 0 000+1-0 00
6 1 -0.029 0.614 0.094 0.094+J 0.000 0.053+J 0.000 0.023+J-0.00 THE ADMITTANCE OF BRANCHLINE 1 IS: SUM = 1.976+J 0.000
THE COUPLING COEFFICIENT INTO BRANCHLINE 1 IS 0.146
THE COOPEING COEFFICIENT INTO BRANCHEINE 1 15 0.140
1 2 0.030 0.604 0.227 0.227+J 0.000 0.055+J 0.000 0.028+J-0.00
2 2 -0.071 0.609 0.525 0.525+J 0.000 0.295+J 0.000 0.152+J-0.00
3 2 0.102 0.632 0.768 0.768+J 0.000 0.632+J 0.000 0.294+J-0.06
4 2 -0.107 0.625 0.768 0.769+J 0.000 0.660+J 0.000 0.339+J-0.01
5 2 0.048 0.616 0.525 0.525+J 0.000 0.288+J 0.000 0.138+J-0.02
5 2 -0.030 0.598 0.227 0.227+J 0.000 0.055+J 0.000 0.029+J-0.00
THE ADMITTANCE OF BRANCHLINE 2 IS: SUM = 1.984+J 0.000
THE COUPLING COEFFICIENT INTO BRANCHLINE 2 IS 0.352
1 3 0.032 0.597 0.296 0.296+J 0.000 0.058+J 0.000 0.032+J 0.00
2 3 -0.071 0.609 0.684 0.684+J 0.000 0.298+J 0.000 0.155+J-0.00
3 3 0.107 0.627 1.000 1.000+J 0.000 0.660+J 0.000 0.338+J-0.00
4 3 -0.107 0.627 1.000 1.000+J 0.000 0.660+J 0.000 0.338+J-0.02
5 3 0.071 0.609 0.684 0.684+J 0.000 0.298+J 0.000 0.155+J=0.00
6 3 -0.032 0.597 0.296 0.297+J 0.000 0.058+J 0.000 0.032+J 0.00
THE ADMITTANCE OF BRANCHLINE 3 IS: SUM = 2.031+J 0.000
THE COUPLING COEFFICIENT INTO BRANCHLINE 3 IS 0.458
THE COUPLING COEFFICIENT INTO BRANCHLINE 3 15 0.438
1 4 0.030 0.598 0.227 0.227+J 0.000 0.055+J 0.000 0.029+J-0.00
2 4 -0.068 0.617 0.525 0.526+J 0.000 0.289+J 0.000 0.138+J-0.02
3 4 0.107 0.625 0.768 0.768+J 0.000 0.660+J 0.000 0.339+J-0.01
4 4 -0 102 0.632 0.768 0.768+J 0.000 0.632+J 0.000 0.294+J-0.06
5 4 0.071 0.609 0.525 0.525+J 0.000 0.296+J 0.000 0.153+J-0.00
8 4 -0 030 0.604 0.227 0.227+J 0.000 0.055+J 0.000 0.028+J-0.00
THE ADMITTANCE OF BRANCHLINE 4 IS: SUM = 1.985+J 0.000
THE COUPLING COEFFICIENT INTO BRANCHLINE 4 IS 0.352
1 5 0 029 0.614 0.094 0.094+J 0.000 0.053+J 0.000 0.023+J=0.00
2 5 -0 064 0.635 0.218 0.218+J 0.000 0.276+J 0.000 0.097+J-0.05
3 5 0 108 0.639 0 319 0.319+J 0.000 0.675+J 0.000 0.323+J-0.08
4 5 -0.099 0.652 0 319 0.318+J 0.000 0.629+J 0.000 0.226+J-0.12
5 5 0 070 0.622 0.218 0.218+J 0 000 0.297+J 0.000 0.138+J-0.04
6 5 -0 025 0.625 0.094 0.094+J 0.000 0.046+J 0.000 0.015+J-0.00
THE ADMITTANCE OF BRANCHLINE 5 IS: SUM = 1,975+J 0.000
THE COUPLING COEFFICIENT INTO BRANCHLINE 5 IS 0. 146

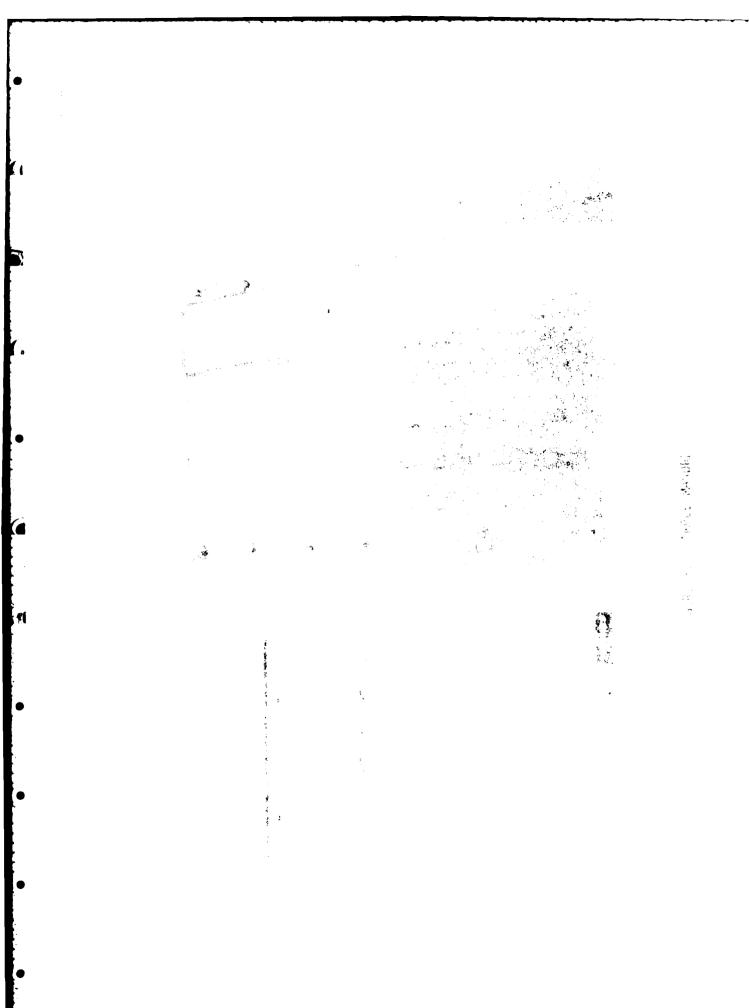
THE TOTAL INPUT IMPEDANCE IS: SUM = 1.001+J 0.000

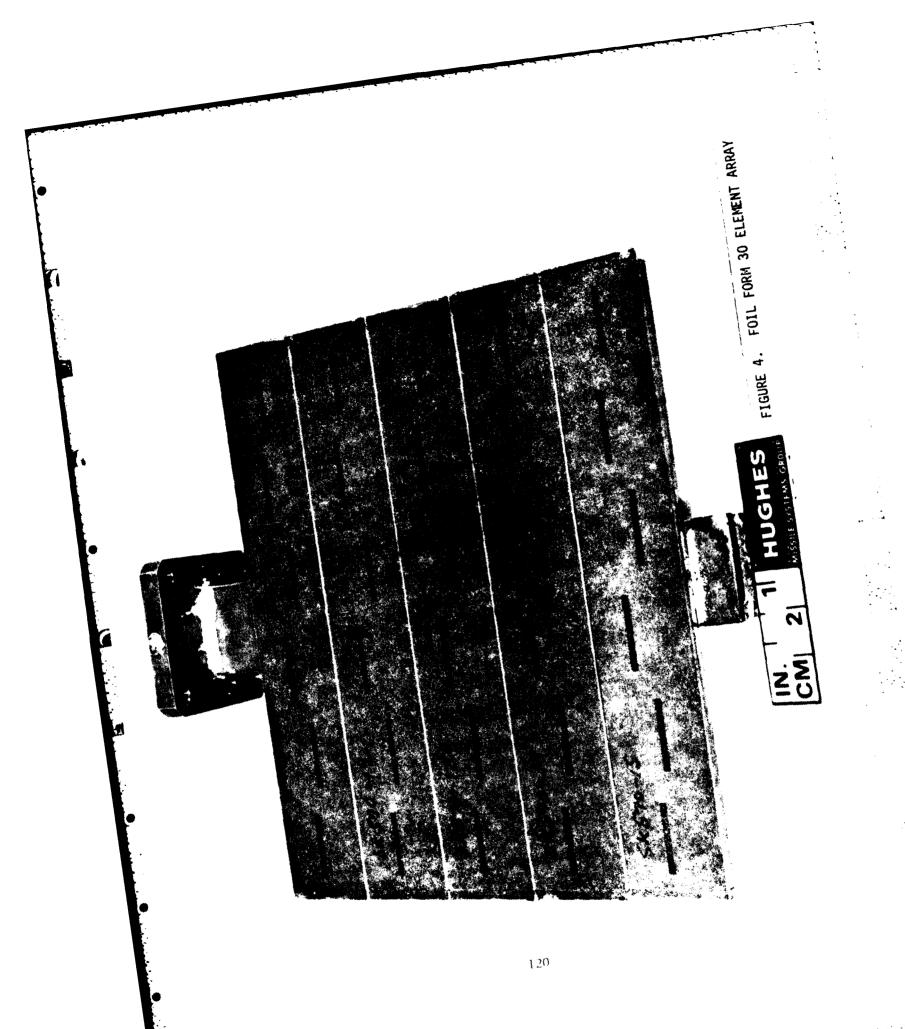


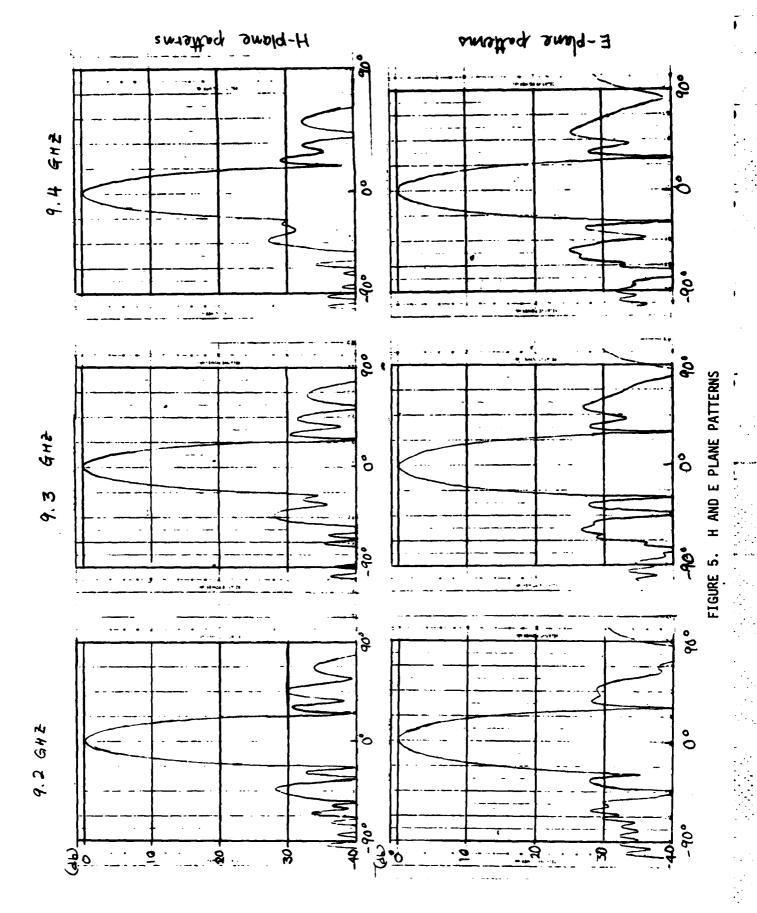
IN THEWES NORMA! 17ED SLOT LEJKATU "29" COMPUTE SLOT SELF ADMITIATE VERTUS AND SLOT OFF SET FIGURE 1



F148 (1980) (1991) (1981)







CONSIDERATIONS FOR EXTENDING THE BANDWIDTH OF ARRAYS BEYOND TWO OCTAVES

By: George Monser
Consulting Engineer

Raytheon Company
Electromagnetic Systems Division
6380 Hollister Avenue
Goleta, California 93117

19-21 September 1984

1984 ANTENNA APPLICATIONS SYMPOSIUM

Sponsored by:

USAF, Rome Air Development Center, Electromagnetic Sciences Division and Univ. of Illinois, Department of Electrical Engineering, Electromagnetics Laboratory
Monticello, Illinois

CONSIDERATIONS FOR EXTENDING THE BANDWIDTH OF ARRAYS BEYOND TWO OCTAVES

By:

GEORGE J. MONSER

SUMMARY

This paper presents a summary of array-element characteristics for a wide-band, dual-polarized, array where the extension in bandwidth is achieved by extending the lower frequency limit.

Array-element behavior over the lower part of the band is described in detail. A lower frequency limit of operation is advanced based on element mismatch loss and efficiency. It is then shown that low active VSWR and good efficiency can be achieved over a two octave band.

1.0 INTRODUCTION

Array designs are typically limited to approximately one octave; the upper limit is determined by a preference to avoid grating lobes, and the lower frequency is selected on the basis of element efficiency.

2.0 ELECTRICALLY SMALL ARRAY ELEMENTS

Figure 1 shows a planar array of N x N elements spaced in center-to-center 0.5 wavelengths. Thus, the dimensions allotted each element are 0.5×0.5 wavelengths. For elements of this size, good efficiency can be achieved (80 percent or higher based on mismatch loss and no dissipative loadings). As the frequency is lowered to one-half the initial value, the element space shrinks to 0.25×0.25 wavelengths and efficiency decreases by 30 to 40 percent.

In characterizing behavior (based on mismatch loss), it is important to remember that three mismatches are of interest as follows:

- 1. Isolated-element VSWR
- 2. Embedded-element (passive) VSWR
- 3. Drive-element (active) VSWR

Isolated element VSWR is used for the efficiency consideration. However, the role of passive and active VSWR and coupling between elements needs consideration. Under some circumstances, good active VSWR can be achieved by cancellation of passive VSWR by coupling as will be illustrated later.

3.0 ARRAY-ELEMENT BEHAVIOR BELOW FI.OW

Figure 2 shows isolated element gain behavior versus wavelength expressed in fractions of a wavelength for different candidate array elements.

Model A is a ridge-loaded horn element with an E-plane aperture of 0.358 inch and an H-plane dimension of 2.25 inches. Internally in the ridge section, the H-plane dimension is 1.30 inches.

Model B is similar to Model A except that in the ridge section the H-plane dimension is 2.00 inches. Model C is a stripline array of four printed notch elements with a total E-plane dimension of 2.25 inches and a thickness of 0.625 inch.

Model D is a small conical helix. Model E is a cavity-backed spiral assembly of two elements.

Figure 3 shows a Model C stripline notch array. Figure 4 shows a Model A ridge loaded horn.

The observation to be made for all candidates is that the gain roll-off characteristic with decreasing frequency is similar and very sharp.* For example for Models A through C the gain decreased 10 dB for a 10 percent frequency change. For Models D and E, roll-off is less. These latter models were not chosen because: (1) conical helices shadow each other during beam scanning; and (2) cavity-backed spirals require lossy loading for optimum patterns performance.

Returning to a consideration of Models A through C, the gain trends for B and C were nearly matched over the lower frequency interval. However. over the upper frequency (approximately two octaves higher), a gain deficiency was noted for Model C. Thus, Models A and B were chosen as representing the best candidates over the full band.

4.0 ARRAY ELEMENT BEHAVIOR APPROACHING FLOW

Figure 5 shows the finished dual-polarized array consisting of horn elements (similar to Model A) with stripline elements built into the horn walls (similar to Model C).

Figures 6A and 6B show the measured passive return loss (VSWR) for each type of embedded element. Observe that the return-loss curves are similar near F_{LOW} . If a criteria is adopted where 50 percent efficiency (i.e., 3 dB return loss) is acceptable, then a lower frequency can be set forth for each type of element. For the horn elements, this occurs near 5 GHz. For the stripline elements this occurs close to 4 GHz.

Figures 7A, 7B, 7C, 8A, 8B, and 8C show active VSWR plots constructed from measured complex passive reflection coefficients and element-to-element coupling factors. Better efficiency in the driven mode was realized than predicted from the earlier data (Figures 6A and 6B).

^{*}See Appendix A.

5.0 OVER-THE-BAND PERFORMANCE

Figures 9 through 13 show measured characteristics for the finished array.

In Figure 9, swept gain for two orthogonal polarizations is displayed over greater than two octaves.

Figure 10 shows swept gain response to incident rotating linear polarization from 6 to 18 GHz for a pair of center elements summed using a 90° hybrid.

Figures 11 and 12 show array element coverage in mid-band for the two principal polarizations. Similar array-coverage patterns were realized over the full two-octave band.

Figure 12 shows orthogonal-to-the-array half-power coverage over the band.

6.0 CONCLUDING REMARKS

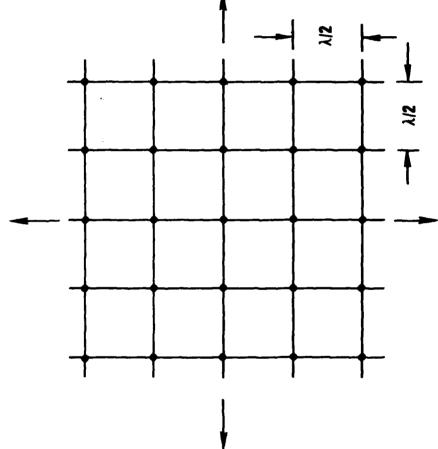
This paper has presented a summary of array-element characteristics for a wide-band, dual-polarized array where the extension in bandwidth was achieved by extending the lower frequency limit.

Array-element behavior over the lower part of the band was described in detail. Based on element mismatch loss and efficiency, a lower frequency limit of operation was advanced. It was then shown that low active VSWR and good efficiency could be achieved over a two octave band.

LIST OF FIGURES

- Figure 1 N x N Planar Array
- Figure 2 Isolated Element Gain vs Electrical Dimension (Candidate Elements)
- Figure 3 Stripline Notch Array
- Figure 4 Ridge-Loaded Horn
- Figure 5 Dual Polarized Array
- Figure 6A Horns, Passive Return Loss (VSWR)
- Figure 6B Strip-Line Notch Array, Passive Return Loss (VSWR)
- Figure 7A Active Element VSWR, Horn Element (0°, 0°)
- Figure 7B Active Element VSWR, Horn Element (30° Scan, 0°)
- Figure 7C Active Element VSWR, Horn Element (60° Scan, 0°)
- Figure 8A Active Element VSWR, Stripline Notch Array (9°, 0°)
- Figure 8B Active Element VSWR, Stripline Notch Array (30° Scan, 0°)
- Figure 8C Active Element VSWR, Stripline Notch Array (60° Scan, 0°)
- Figure 9 Swept Gain, Finished Array
- Figure 10 Swept Gain, Rotating Linear, Finished Array
- Figure 11 Array Coverage
- Figure 12 Orthogonal Coverage
- Figure 13 Orthogonal Plane BW
- Figure Al Normalized Gain(s)
- Figure A2 Normalized Gain(s)

184/45



N x N Planar Array Figure 1.



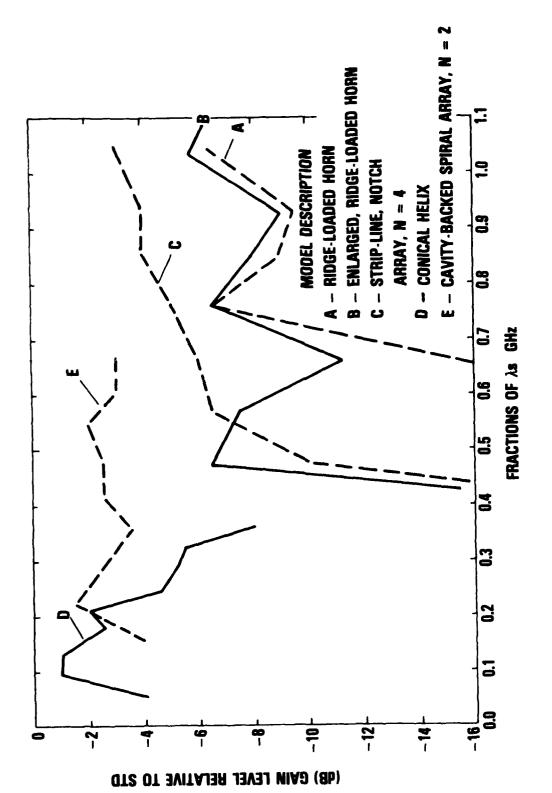
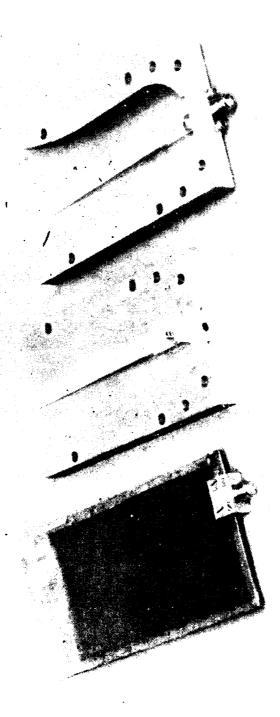


Figure 2. Isolated Element Gain vs Electrical Dimension (Candidate Elements)



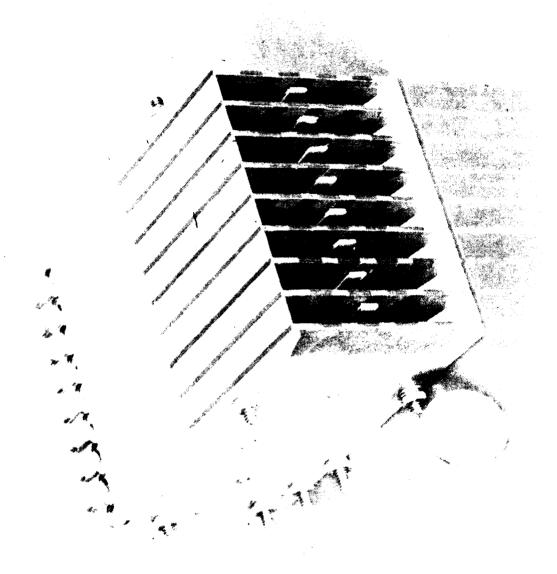
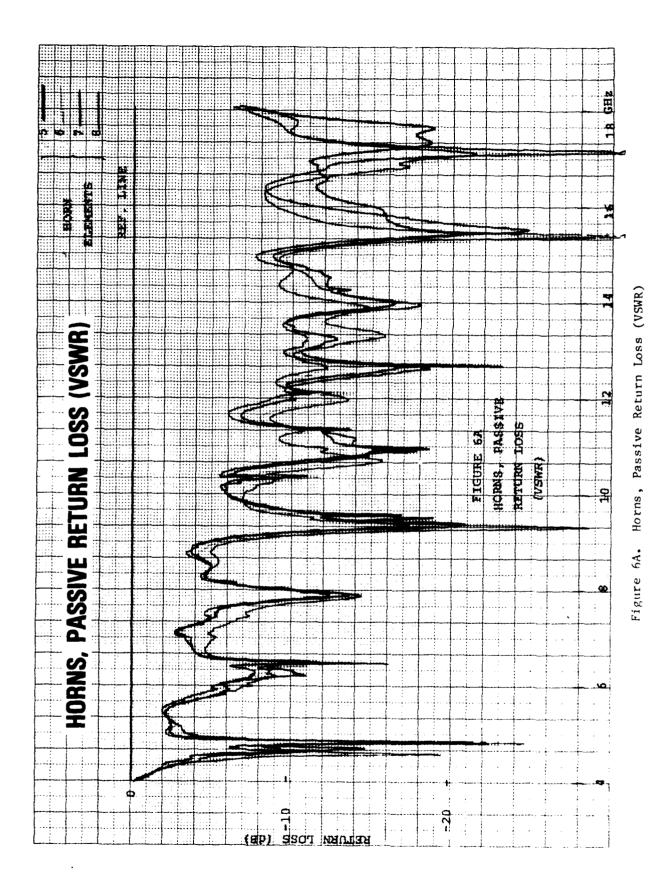


Figure 5. Dual Polarized Array



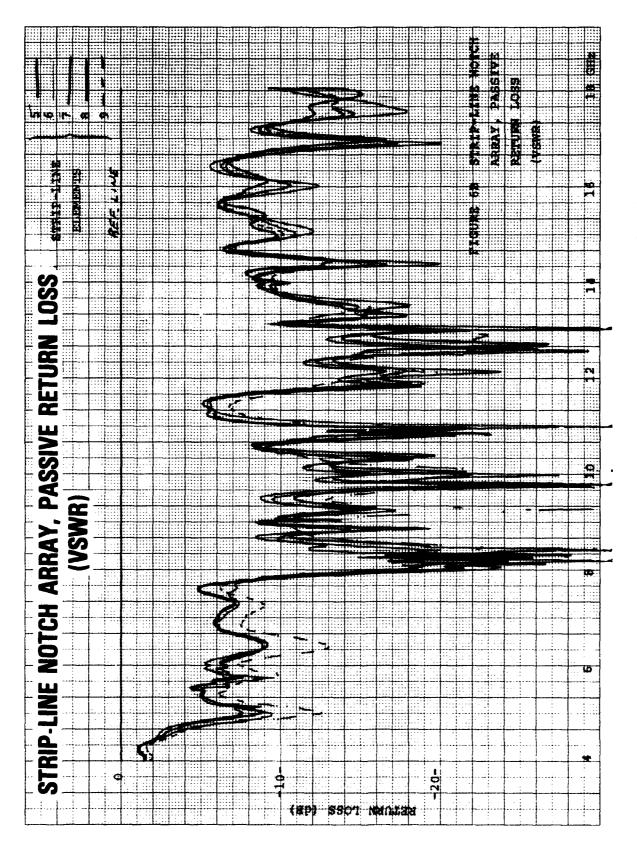


Figure 6B. Stripline Notch Array, Passive Retorn Loss (VSWR)



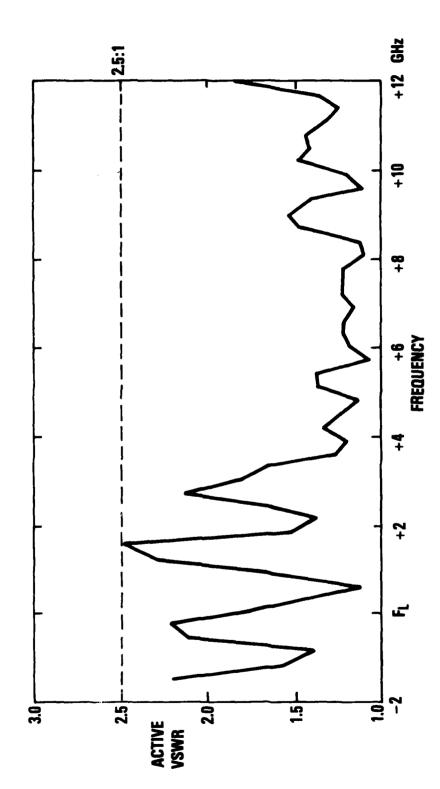


Figure 7A. Active Element VSWR, Horn Element (0°, 0°)

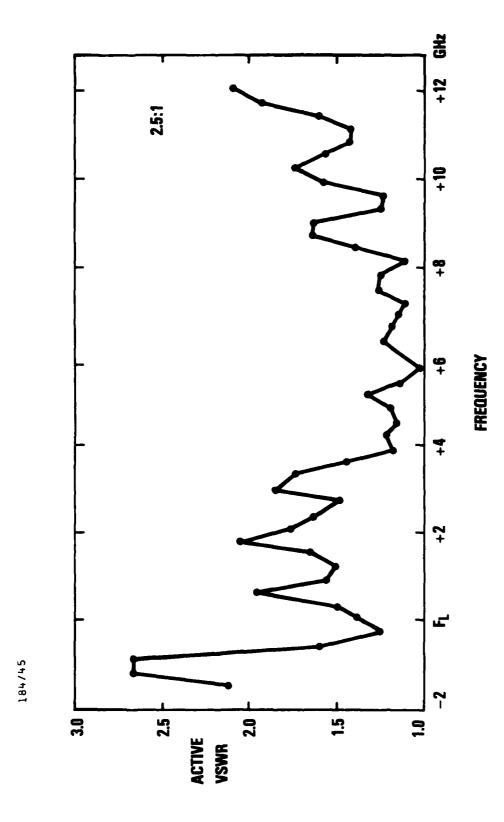


Figure 7B. Active Element VSWR, Horn Element (30° Scan, 0°)

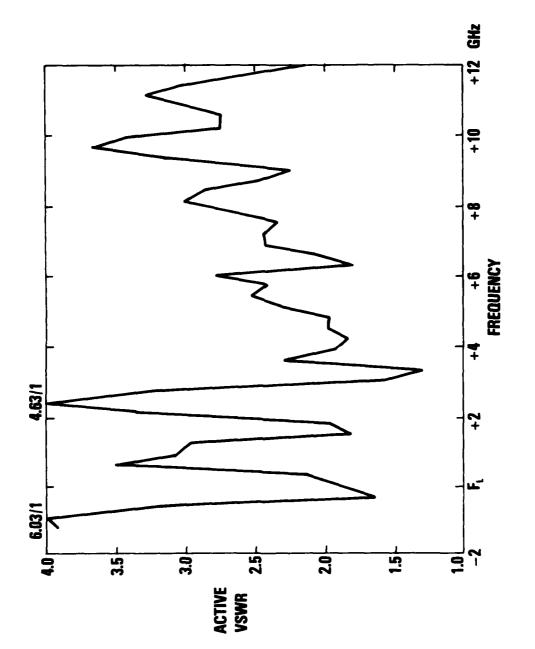


Figure 7C. Active Element VSWR, Horn Element (60° Scan, 0°)



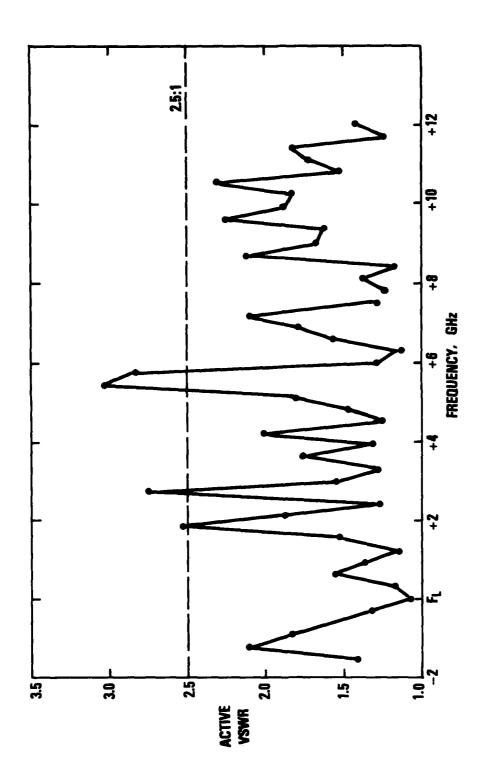


Figure 8A.. Active Element VSWR, Stripline Notch Array (9°, 0°)

Figure 8B. Active Element VSWR, St. Ipline Notch Array (30° Scan, 0°)

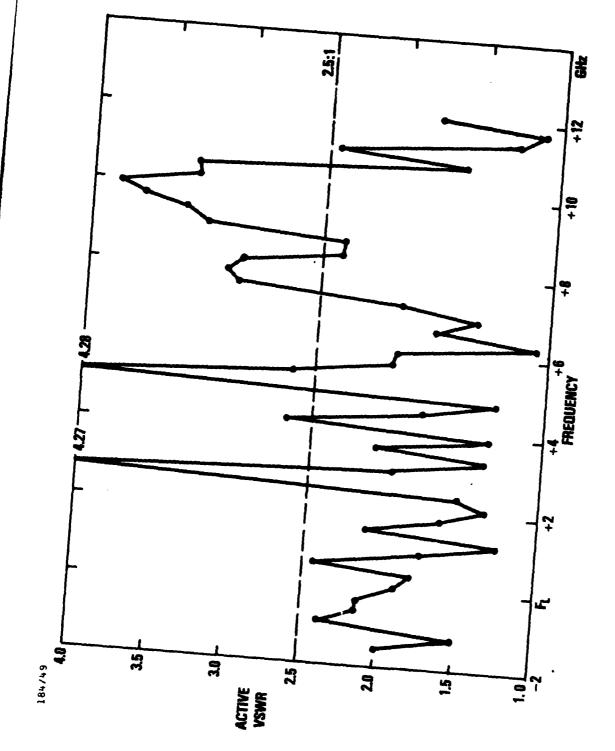


Figure 8C. Active Element VSWR, Stripline Notch Array (60° Scan, 0°)

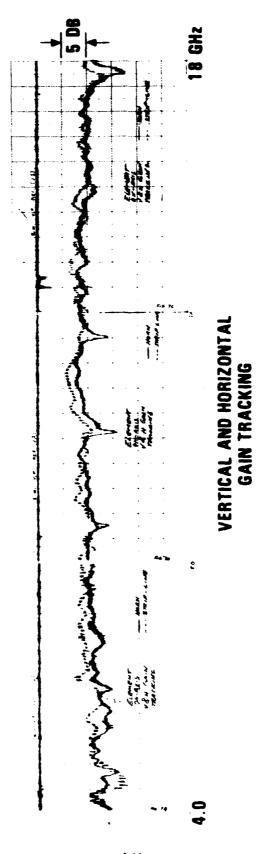
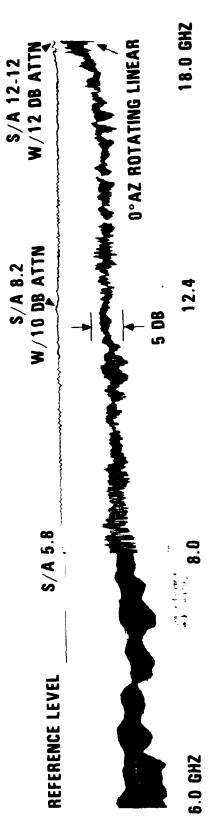


Figure 9. Swept Gain, Finished Array



DPA W/HYBRID AND PHASE SHIFTERS

Figure 10. Swept Gain, Rotating Linear, Finished Array

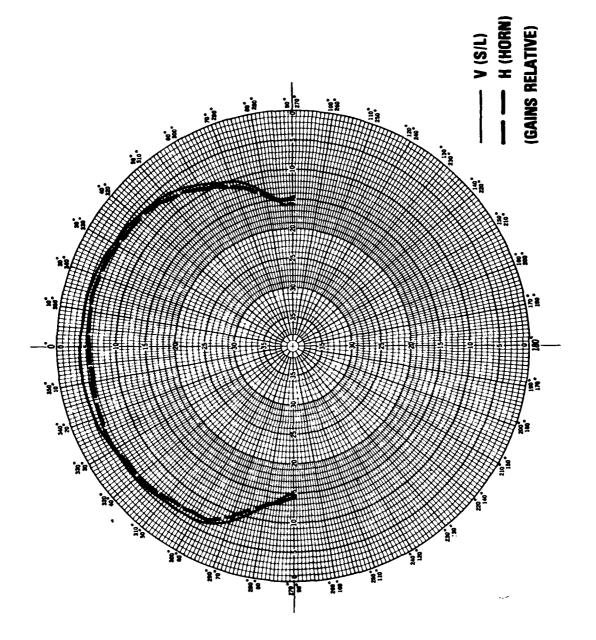


Figure 11. Array Coverage



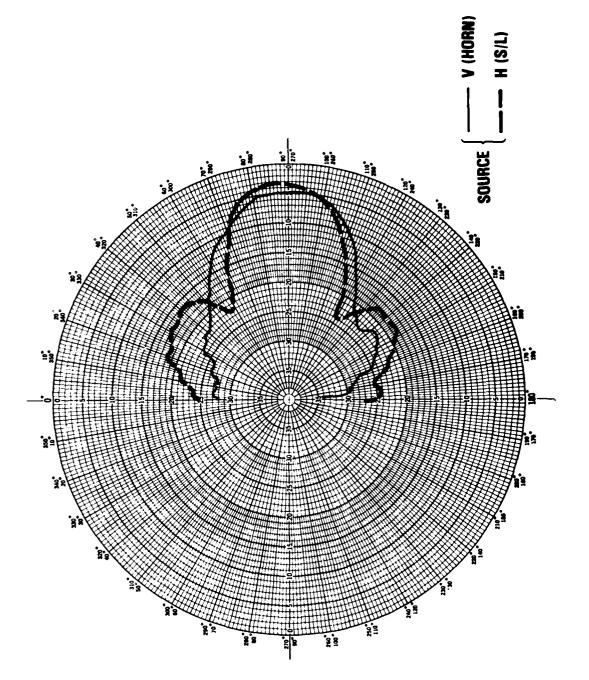


Figure 12. Orthogonal Coverage

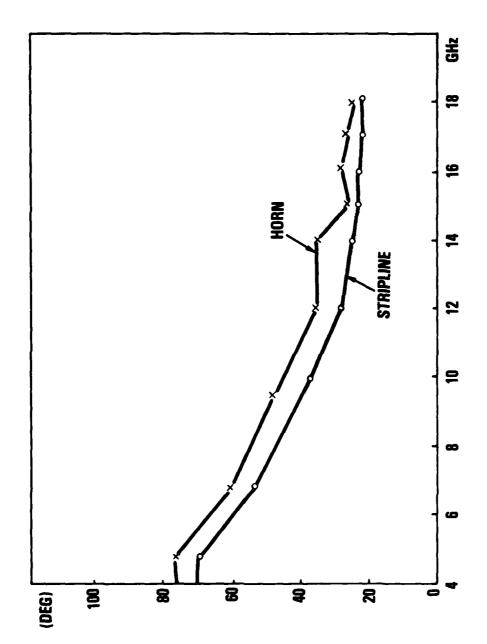


Figure 13. Orthogonal Plane BW

APPENDIX A

Further Considerations Affecting the Selection of Candidates

Figure Al shows the gain behavior for Models A through C and is of primary interest. Figure A2 shows the gain behavior of Models D and E. Grouping of data may be noted when displayed in this fashion. For example, in Figure Al Models A and B are similar and the normalizing dimension is the "A" dimension of the waveguide. In Figure A2 the normalization dimension is the length of one base side (square conical helix) and the outer dimension of the square, cavity-backed spiral C.

Returning to Figure A1, for a normalized dimension greater than 1.0 the gain trends tracked well above 2.0. However, the enlarged unit showed a higher order mode (gain drop-out). As a consequence, Models A and C were selected for use in the final design model, as reported. Provided the gain deficiency of Model B is correctible, even wider bandwidth may be achievable.

Returning to Figure A2, the cavity-backed spiral element is usable over wide bandwidths in receive applications. However, the spiral filaments tend to be thin with close feed-points and small baluns above 10 GHz. As a consequence, they are not well suited for handling power.

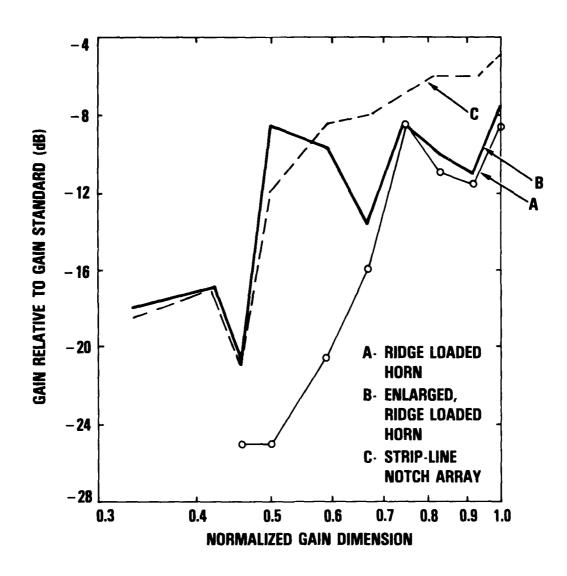


Figure Al. Normalized Gain(s)

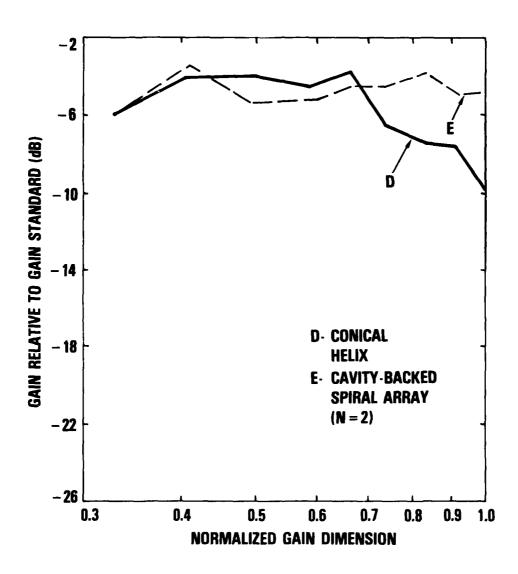


Figure A2. Normalized Gain(s)

MICROSTRIP MONOPULSE DIPOLE ARRAY

by

William Miccioli, John Toth, Norbert Sa, and Michael Lewis
Raytheon Company Missile Systems Division
Bedford, Massachusetts 01730

to be presented at

1984 Symposium on Antenna Applications Urbana, Illinois

September 19-21, 1984

MICROSTRIP MONOPULSE DIPOLE ARRAY

William Miccioli, John Toth, Norbert Sa, Michael Lewis Raytheon Company, Missile Systems Division Bedford, Massachusetts 01730

ABSTRACT

Typically, microstrip array antennas consist of microstrip patch radiating elements integrated with either a stripline or microstrip corporate feeding structure. This paper describes the development of a microstrip radiating aperture utilizing multiple microstrip dipole radiators fed by a resonant feed configuration. This array combines an efficient capacitively coupled radiator feeding mechanism with a planar power divider configuration to achieve an extremely thin ($<.05\,\lambda$), lightweight antenna aperture. Linear array dipole matching theory and radiator bandwidth improvement techniques are also described.

A quadrant based microstrip monopulse antenna was constructed and tested. Experimental data from this array, its subassemblies and individual components are presented and compared to analytical predictions.

1. INTRODUCTION

Since the late 1970s, experimental and theoretical investigations of printed circuit type antennas have become increasingly popular. The inherent advantages of microstrip antennas have been clearly stated in the past, and numerous antenna configurations of

different sizes and shapes have been suggested. Of even more prolonged interest has been the analysis of the performance properties of the printed microstrip dipole^{1,2,3}. Most of the early investigations dealt with examination of the radiator pattern, impedance, and coupling properties, with little concern for methods to excite the dipoles. Oltman^{4,5} has presented some novel feeding techniques involving electromagnetic coupling (EMC) of the dipole radiators to a microstrip transmission line in which no physical connection is required. The method provides a simple means to couple single or multiple dipole radiators to a standard open circuited microstrip feed line, thereby eliminating complicated interconnection schemes.

This paper presents the theory and experimental findings from the development of a quadrant monopulse array using EMC dipoles. The basic dipole/feed line structure is shown in Figure 1. Multiple dipole radiators on the upper dielectric surface are excited simultaneously by a single microstrip feed line located on the center layer forming a resonant linear array. Section 2 contains a brief description of the parameters involved in exciting multiple radiators and of methods for obtaining broader bandwidth structures based on the stacked element approach 6,7. Section 3 provides actual measured element and array performance data, while Section 4 summarizes the pertinent findings of the current development.

2. THEORY OF OPERATION

The resonant linear array of half wavelength dipoles shown in Figure 1 has been used in conjunction with a power division network

to develop each quadrant of a microstrip monopulse planar array. An exploded view of this array antenna is shown in Figure 2. When built and tested, the antenna yielded radiation patterns and gain data that were in close agreement with theoretical predictions over a three per cent bandwidth and an input VSWR of less than or equal to 2:1.

The microstrip feedline of each individual linear array may be modeled as an open circuited transmission line. The radiating elements are spaced at intervals of one wavelength at the center frequency and are positioned along the transmission line at the voltage standing wave maxima. For these conditions, the radiating elements may be modeled as conductances in parallel. For an ideal system in which the only losses are radiation losses, the model for the resonant linear array takes the form of the circuit shown in Figure 3. The total power radiated from the linear array may be expressed as follows:

$$P = v^2 G_t = v^2 \sum_i g_i$$

The value of a single conductance, g_i, can be controlled by varying the lateral distance ("d" in Figure 1a) between the feed line and the radiator. By controlling this spacing for each radiator, virtually any desired illumination taper may be achieved along a linear array.

For a given illumination taper, the proper level of coupling for each radiator or combinations of radiators can be calculated directly in terms of voltage standing wave ratios. By way of example, consider the case of a uniformly illuminated, three element linear array:

$$g_1 = g_2 = g_3 = 1/3;$$
 $G_t = 1.0$

where an impedance value of 50Ω has been normalized to 1.

With a single radiator coupled to the feed line, the conductance and VSWR will have the following values:

$$g_1 = 1/3;$$
 VSWR = 3.0

With two such radiators coupled to the feed line, the desired VSWR is:

$$g_1 + g_2 = 2/3;$$
 VSWR = 1.5

The addition of the final radiator will ideally yield a perfect match:

$$g_1 + g_2 + g_3 = 1.0$$
; VSWR = 1.0

A consequence of selecting uniform illumination for a given resonant array is that each radiator will have the same lateral displacement from the feed lines as all other radiators. A six element linear array satisfying this criterion was built and tested. An H-plane forward hemisphere far-field radiation pattern is shown in Figure 4. As indicated in the figure, the agreement with the theoretical pattern is within 1.0 dB for the region within ±45 degrees of broadside. This pattern is typical of those radiation patterns achieved over the 3% bandwidth.

To overcome the characteristically narrow bandwidth of operation, a "stacked" dipole radiator may be used in this array configuration. The stacked dipole radiator consists of two dipole radiators vertically separated by a layer of dielectric material. As with the single dipole radiators, the amount of power coupled to the stacked elements is a

function of the lateral separation between the feedline and the edge of the radiators. With a lower dipole that is approximately 5 percent shorter than the upper dipole, a bandwidth of 8 percent can be achieved.

The increase in operating bandwidth can be attributed to two effects. The first is the increase in the height of the upper dipole above the ground plane; the second is the introduction of a second resonant dipole tuned to a frequency slightly different from that of the first dipole. A return loss plot that illustrates the bandwidth enhancement for a three-element linear array is shown in Figure 5.

3. EXPERIMENTAL RESULTS

Linear arrays of microstrip dipoles were constructed of two bonded layers of Duroid 5880 having a relative dielectric constant of 2.2. The .015 inch thick lower board had a 50 ohm feed line etched to its upper surface and a full copper ground plane on its bottom surface. The individual dipole radiators were located on the top surface of a .031 inch thick upper board at intervals of one wavelength in the effective dielectric medium.

Figure 6 illustrates the H plane radiation pattern measured for a three element linear array operating at the design frequency. The cross-polarized response is more than 20 dB below the peak of the co-polarized pattern. Phase error effects are seen in the asymmetrical side lobe structure and shallow nulls. These phase error effects become more pronounced at the

edges of the band. Similar results were obtained for two and four element linear arrays.

To obtain a monopulse configuration, the full array was divided into quadrants. The overlay of the two layers of the full microstrip array artwork is shown in Figure 7. Each quadrant had two power dividers feeding three linear arrays with a total of eight dipole radiators. Each of the resonant linear array designs was fabricated on a separate test piece and measured for VSWR, radiation patterns, and gain before being incorporated into the full array. The power dividers used were of the single-section Wilkinson type. A small, removable dielectric plug was located on the upper board above each power divider to allow access for soldering a small chip resistor between the two power divider output branches.

The triangular lattice—chosen for the placement of the full array radiators resulted in identical diagonally opposite quadrants of the main array. Measured principal plane radiation patterns of a single quadrant are compared to the theoretical principal plane patterns of an uniformly illuminated quadrant of eight isotropic radiators in Figures 8 and 9. The correlation between measured and theoretical radiation patterns is quite good. The return loss measured for a single quadrant is provided in Figure 10. These data are representative of results obtained for all other quadrants.

A stripline monopulse network was used to form sum and difference patterns for the full microstrip array shown in Figure 11.

Measured principal plane radiation patterns of the antenna are shown in Figures 12 and 13. The pattern characteristics are consistent with those expected for this array configuration. Difference channel null depths greater than 30 dB below the sum channel peak were obtained.

The sum channel measured gain of the full five wavelengths diameter microstrip array is shown in Figure 14. The gain, when measured with a stripline arithmetic network (accounting for 1.1 dB loss at the antenna design frequency), peaks at 19.0 dB.

4. CONCLUSION

An efficient technique for feeding multiple microstrip dipole radiators has been presented. A microstrip monopulse antenna aperture utilizing EMC dipoles has been constructed and evaluated. Each quadrant consisted of a corporate power divider feeding three separate resonant linear arrays. The five wavelength diameter, uniformly illuminated aperture achieved greater than 19.5 dB gain, 17 dB sum sidelobes, and 30 dB difference null depth over a 3% frequency band. A method of stacking dipoles which can be used to increase the available bandwidth to 8-10% has also been presented.

REFERENCES

- Tsandoulas, G. N. (1969) Excitation of a Grounded Dielectric Slab by a Horizontal Dipole, <u>IEEE Trans. Antennas and Prop.</u>, Vol. AP-17, pp. 156-161.
- Uzunoglu, N. K., Alexopoulous, N. G., and Fikioris, J. G. (1979)
 Radiation Properties of Microstrip Dipoles, <u>IEEE Trans. Antennas</u>
 and Prop., Vol. AP-27, pp. 853-858.
- Rana, I. E. and Alexopoulous, N. G. (1981) Current Distribution and Input Impedance of Printed Dipoles, <u>IEEE Trans. Antennas and Prop.</u>, Vol. AP-29, pp. 99-105.
- Oltman, H. G. and Huebner, D. A. (1981) Electromagnetically Coupled Microstrip Dipoles, <u>IEEE Trans. Antennas and Prop.</u>, Vol. AP-29, pp. 151-157.
- 5. Oltman, H. G. U.S. Patent 4054874, October 18, 1977.
- 6. Dahele, J. S. and Lee, K. F. (1982) Experimental Study of the Effect of Substrate Thickness on Single and Stacked Circular-Disc Microstrip Antenna, 1982 APS Symposium Digest, pp. 66-69.
- Long, S. A. and Walton, M. D. (1979) A Dual-Frequency Stacked
 Circular-Disc Antenna, <u>IEEE Trans. Antennas and Prop.</u>, Vol. AP-27,
 pp. 270-273.

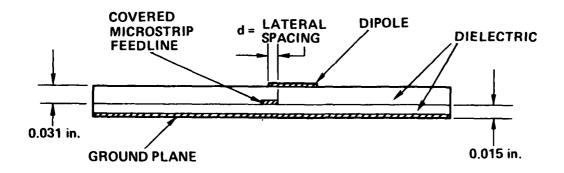


Figure la. EMC Linear Array, Cross-Sectional View

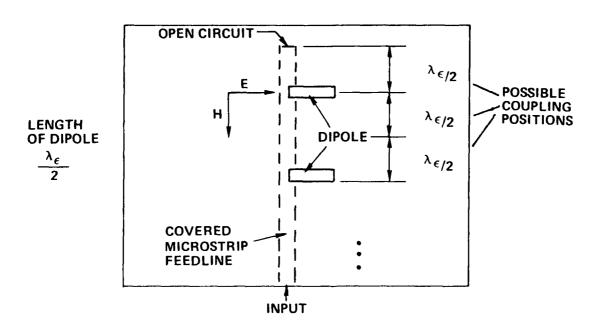


Figure 1b. EMC Linear Array, Top View

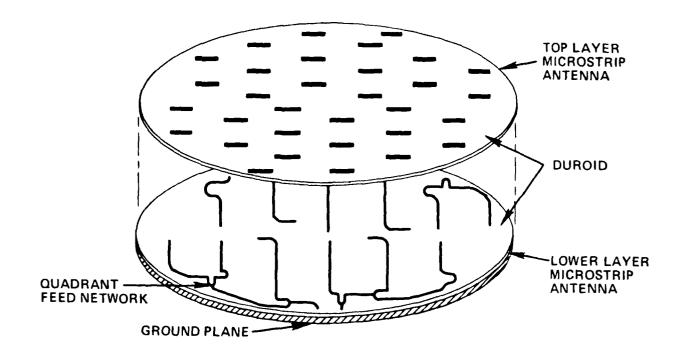


Figure 2. Microstrip Monopulse Array, Exploded View (Quadrants indicated)

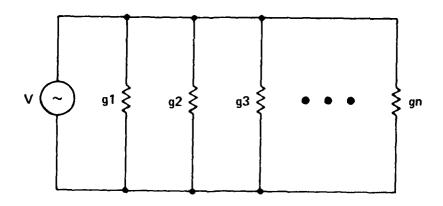


Figure 3. Resonant Circuit Model of Linear EMC Dipole Array

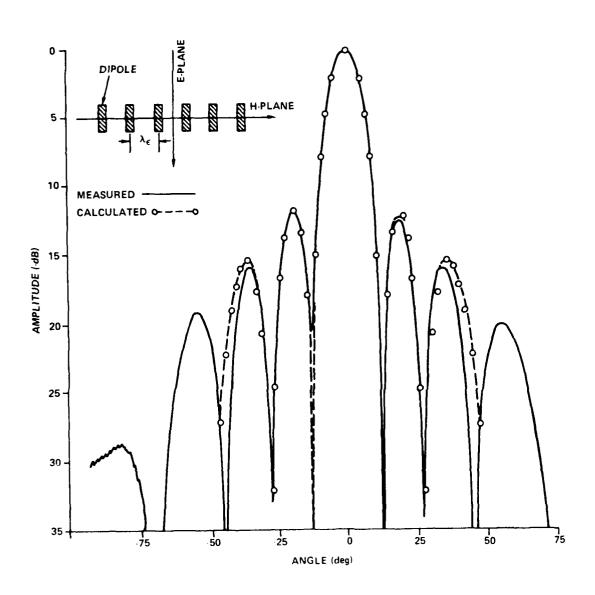


Figure 4. H-Plane Radiation Pattern of 6 Element Linnear Array

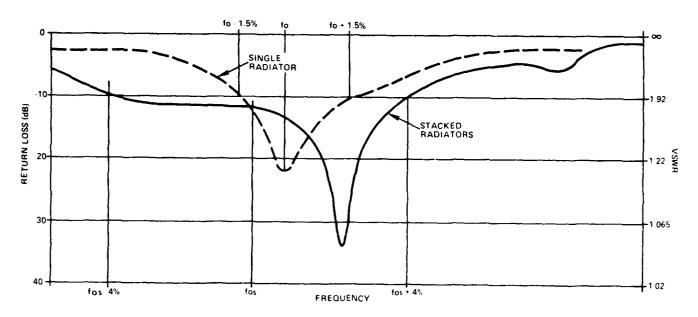


Figure 5. Input Impedance Match of Bonded 3 Element Arrays

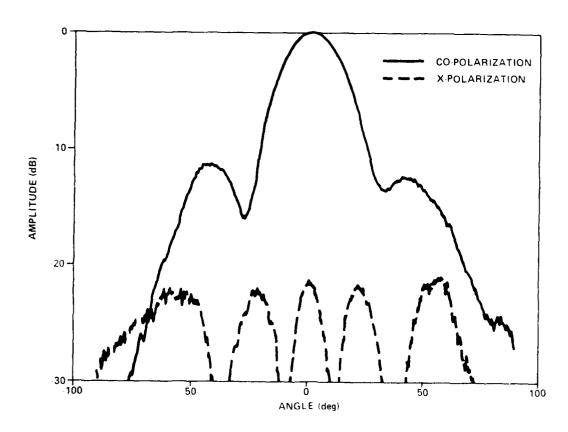


Figure 6. Three Element Dipole Array H-Plane Radiation Pattern

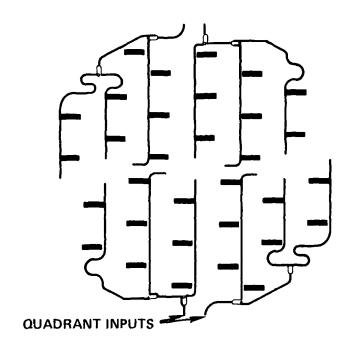


Figure 7. Full Microstrip Array Artwork

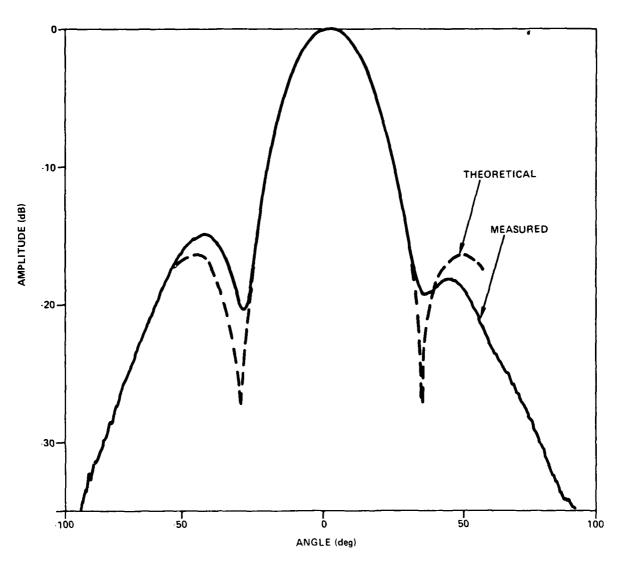


Figure 8. Single Quadrant Principal Plane Pattern (H-Plane Cut)

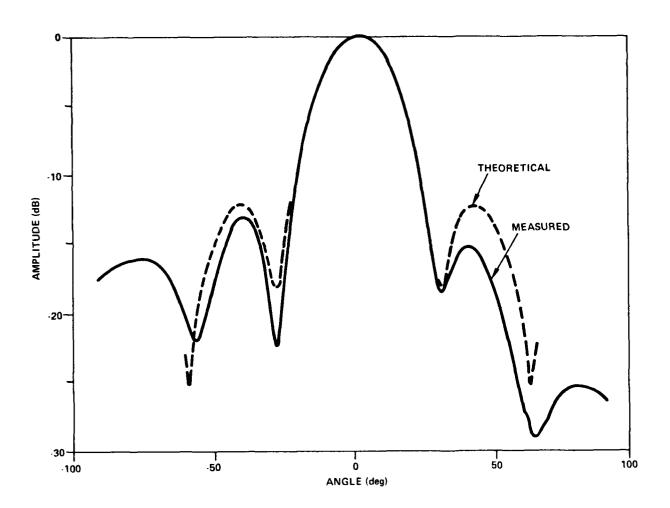


Figure 9. Single Quadrant Principal Plane Pattern (E-Plane Cut)

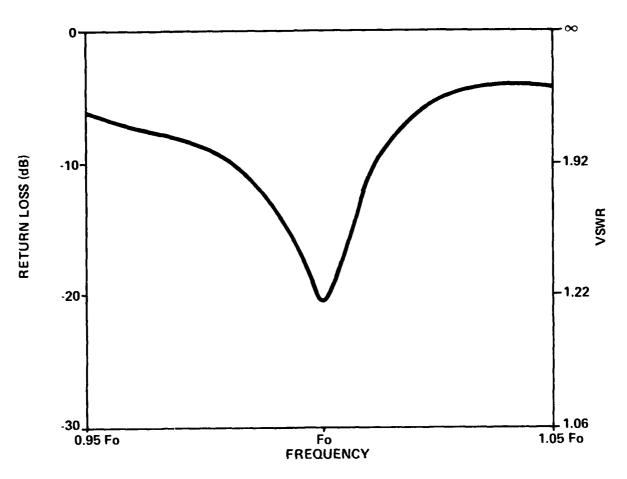


Figure 10. Single Quadrant Input Impedance Match

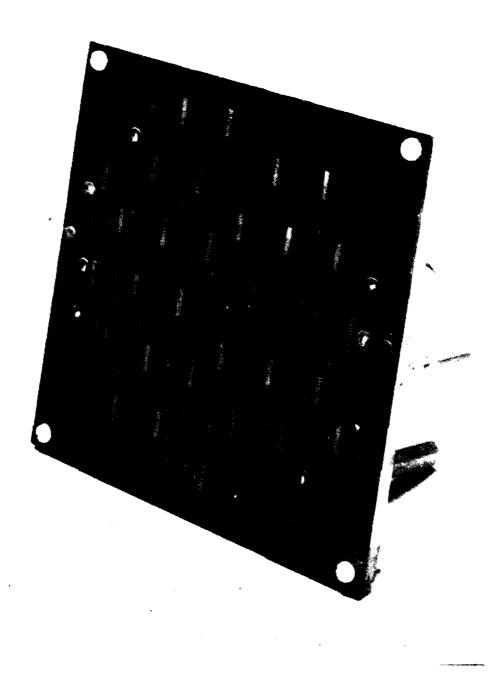


Figure 11. Microstrip Monopulse Dipole Array

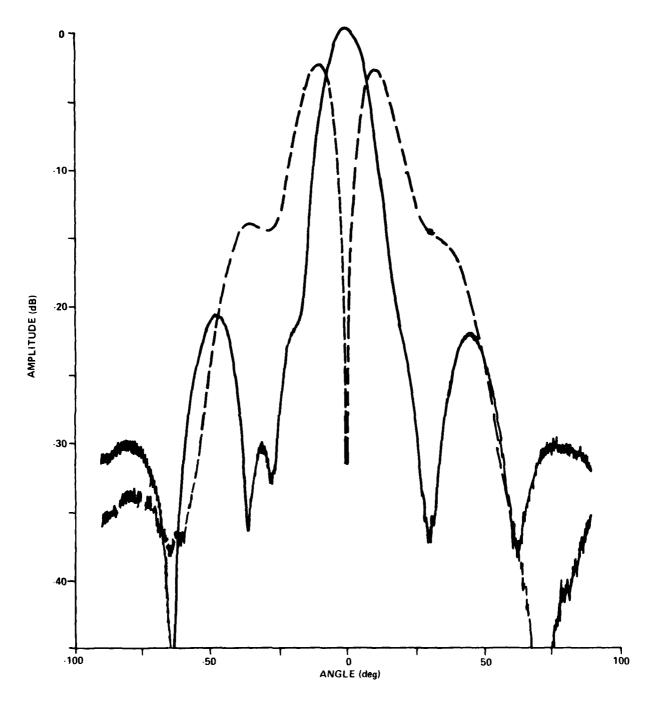


Figure 12. Microstrip Monopulse Dipole Array Principal Plane Radiation Patterns (E-Plane Cut)

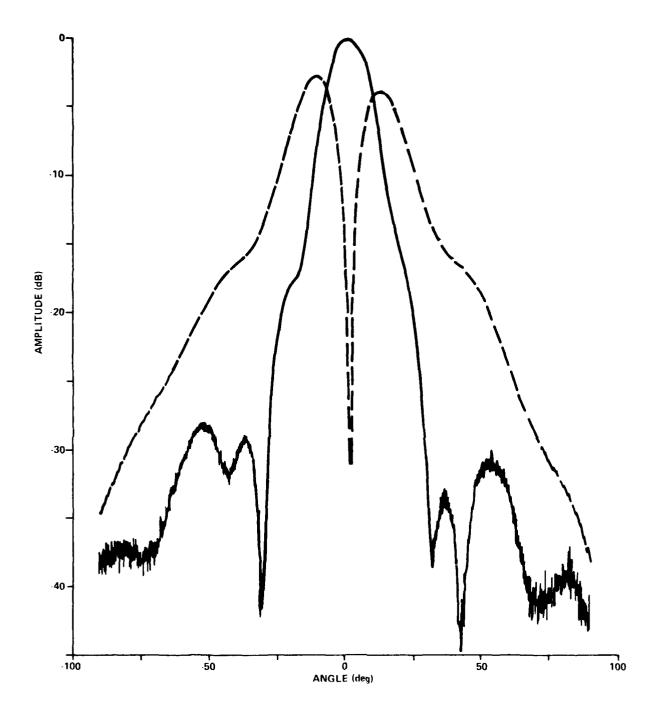


Figure 13. Microstrip Monopulse Dipole Array Principal Plane Radiation Patterns (H-Plane Cut)

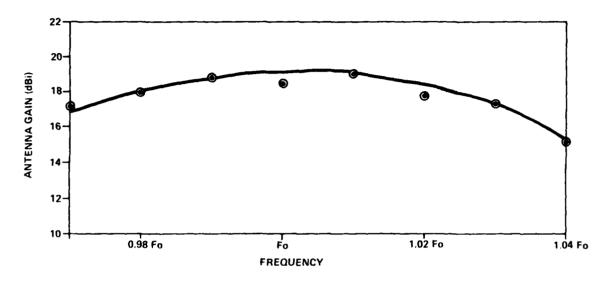


Figure 14. Microstrip Monopulse Dipole Array Σ -Channel Peak Gain

Theory and Experiment for Infinite Microstrip Arrays

Steven M. Wright
Dept. of Radiology and Medical Imaging
Saint Francis Medical Center
530 NE Glen Oak Drive
Peoria, Illinois 61637

and

Y. T. Lo
Dept. of Electrical Engineering
University of Illinois
1406 W. Green St.
Urbana, Illinois 61801

ABSTRACT

Because of their unique characteristics, microstrip antennas are particularly well suited for use in large scanning arrays. To obtain greater bandwidth, it is useful to use thicker substrates, which can increase the effects of mutual coupling and lead to significant mismatch or blindness for certain scan angles.

Using an infinite array formulation, the impedance of a single element in an infinite array environment has been solved with the method of moments. Mutual coupling is built into the solution, and the presence of surface waves is accounted for by using the periodic Green's function for the grounded dielectric substrate. An important feature of the solution is an acceleration technique which improves the efficiency by more than an order of magnitude as compared to the standard formulation.

Examples are presented demonstrating blindness in arrays of microstrip dipoles on various substrates, both with and without radomes. In addition, examples of the impedance of patch arrays are given. In order to check the validity of the theoretical results, several array configurations, both with and without radome layers, were tested in a simple waveguide simulator, with good results.

1.0 INTRODUCTION

Recently there has been a great deal of interest in arrays made of microstrip antennas, as their printed circuit construction makes them well-suited for use in large scanning arrays. One major disadvantage of the microstrip antenna is its narrow bandwidth. It is well known that increased bandwidth can be obtained by increasing the thickness of the substrate on which the microstrip antenna is

printed. Unfortunately, many analysis techniques employ approximations which are valid only for thin substrates. Other more general approaches suffer from a lack of computational efficiency, which in practice can restrict usefulness due to high computational costs. In addition, the analysis of antenna arrays requires one to include the effects of mutual impedances between antenna elements. One approach to this problem, the element-by-element approach [1], is to individually calculate the mutual impedance between elements. A more computationally efficient approach to the analysis of large periodic arrays is the infinite array approach. With this approach one need only determine the current on one patch, as Floquet's theorem assures the satisfaction of the boundary condition on all other patches. As is generally the case in the analysis of periodic problems, this approach requires the evaluation of slowly convergent infinite series. In this paper a general moment method [2] approach is used to analyze infinite arrays of microstrip dipoles and patches on thick substrates. A summation technique [3-5] is used to significantly improve the computational efficiency of the solution.

2.0 FORMULATION

To determine the currents on the antenna an integral equation for the total patch current is written which enforces the boundary condition that the total tangential electric field on the surface of the patch is zero. Using the infinite array approach, the integral equation for the patch current becomes dual algebraic equations

$$\sum_{\mathbf{m}\mathbf{n}} \widetilde{G}_{\mathbf{x}\mathbf{x}}(\vec{k}_{\mathbf{m}\mathbf{n}}) \ \widetilde{J}_{\mathbf{x}}(\vec{k}_{\mathbf{m}\mathbf{n}}) \ \frac{e^{\mathbf{j}\vec{k}_{\mathbf{m}\mathbf{n}} \cdot \hat{\rho}}}{A} + \sum_{\mathbf{m}\mathbf{n}} \widetilde{G}_{\mathbf{x}\mathbf{y}}(\vec{k}_{\mathbf{m}\mathbf{n}}) \ \widetilde{J}_{\mathbf{y}}(\vec{k}_{\mathbf{m}\mathbf{n}}) \ \frac{e^{\mathbf{j}\vec{k}_{\mathbf{m}\mathbf{n}} \cdot \hat{\rho}}}{A} = - \ \mathbf{E}_{\mathbf{x}}^{\mathbf{i}\mathbf{n}\mathbf{c}}(\hat{\rho})$$

 $\sum_{mn} \widetilde{G}_{yx}(\vec{k}_{mn}) \widetilde{J}_{x}(\vec{k}_{mn}) = \frac{e^{j\vec{k}_{mn} \cdot \hat{\rho}}}{A} + \sum_{mn} \widetilde{G}_{yy}(\vec{k}_{mn}) \widetilde{J}_{y}(\vec{k}_{mn}) = - E_{y}^{inc}(\hat{\rho})$

(1)

 \tilde{G} and \tilde{J} are the Fourier transforms of the Green's function for the grounded dielectric substrate and the unknown current distribution, and A is the area in one period, or unit cell of the array. Equation (1) expresses the field of the antenna as a sum of Floquet modes, dependent of the spectral variable \vec{K}_{mn} . Further details are available [6,7]. An approximate solution for the equation can be obtained using the method of moments. This technique reduces the coupled equations into a set of simultaneous equations which can be solved by matrix techniques. Using this method, the most difficult step in the solution is the computation of the matrix elements, which consist of infinite summations of Floquet modes, similar to those in Equation (1).

Recently, a general method was reported [3-5] which allows for efficient evaluation of these infinite summations. This technique has been used to efficiently analyze arrays of dipoles in free space [5] and arrays of microstrip dipoles [6].

3.0 INFINITE ARRAYS OF MICROSTRIP DIPOLES

Microstrip dipole arrays have been receiving increased attention in recent years. One important advantage that dipole arrays have over patch arrays is the small amount of space on the actual array plane consumed by the antenna element. This conserves room which may be needed for associated circuitry such as matching networks and phase shifters.

An array of dipoles on a single layer grounded dielectric slab (GDS) is pictured in Figure 1. The dipole is oriented along \hat{y} and the \hat{x} directed current is assumed to be zero. Only one basis function is used in the transverse direction, with the transverse current distribution chosen to satisfy the edge condition for the current flowing parallel to the edge of a perfectly conducting strip in free space. A basis function with this edge condition is referred to as an edge mode, and is given by

$$\hat{J}_{y}(x,y) = \hat{y}(1 - |y|/L_{y}) \cdot \frac{1}{\sqrt{1 - (x/w_{x})^{2}}} \qquad |x| \leq w_{x} \\ |y| \leq L_{y}$$
 (2)

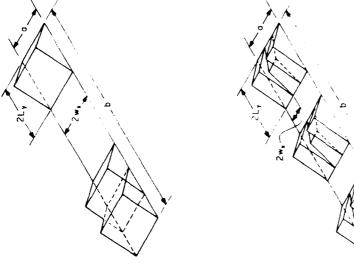
where $\mathbf{w}_{\mathbf{x}}$ and $\mathbf{L}_{\mathbf{v}}$ are the half-width and half-length of the basis function.

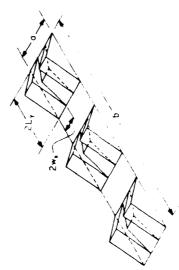
The validity of the assumed transverse current distribution was checked by placing multiple basis functions in the x direction, as shown in Figure 2, and solving for the transverse current distribution. In this case rooftop basis functions were used. A general rooftop basis function is given as

$$\vec{J}_{y}(x,y) = \hat{y}(1 - |y|/L_{y}) \qquad |x| \leq w_{x} |y| \leq L_{y}$$
 (3)

Good agreement was found between the assumed and the calculated transverse current distributions for dipole widths less than approximately 0.02 λ_0 .

Computed results were initially checked by comparing to Stark's results for the impedance of infinite dipole arrays over a ground plane [8]. Results using the present method agree very well with his results. In addition, Pozar and Schaubert have independently computed the impedance of microstrip dipoles in an infinite array [9,10]. The major difference between their method and the





Section of an infinite array array of microstrip dipoles. Figure 1.

Basis function layout on microstrip dipoles. Figure 2.

present method is the use of an acceleration technique to improve the efficiency of the present solution. Their results are in good agreement with results calculated here.

To demonstrate the effectiveness of the acceleration technique, the impedance of an array was computed both with and without using any acceleration to compute the matrix elements. The dimensions of the array considered in this example are given in Table 1. When computing the matrix elements required in the moment method solution, the upper limit on the infinite sums must be chosen appropriately. Most authors choose a suitable upper limit beyond which satisfactory convergence is obtained. For dipole arrays with approximately half wave spacing, an upper limit of $|\mathbf{m}| = |\mathbf{n}| \approx 60$ has been used by Pozar and Schaubert with sinusoidal basis functions, which have approximately the same convergence properties as a function of m and n as rooftop functions.

Results for the impedance of an element in the array using edge mode basis functions with no acceleration are shown in Table 1. It is seen that as the upper limit on m and n, denoted M and N, is increased the results approach the result obtained using the acceleration technique. However, even at M=N=90 the unaccelerated result is still changing. If one uses M=N=60, the unaccelerated result requires appoximately 11 seconds, or approximately 1 second per basis function, as compared to a result of 0.19 second total, or 0.016 second per basis function for the accelerated method. Similar results are obtained using rooftop basis functions. Again, as M and N are increased the results approach the accelerated result. For this case, if M=N=60 is chosen as the upper limit on the summations, the savings in computer time is roughly a factor of 20 by using the acceleration technique. This savings can become very important when analyzing arrays of patches, where hundreds of matrix elements must be computed.

TABLE 1

CONVERGENCE FOR UNACCELERATED COMPUTATION OF INNER PRODUCTS USING EDGE MODES

ACCELERATED RESULT: 53.709 - j 4.294 OHMS

Upper limit	R (ol	jX nms)	cpu time (sec.)	
	•	,	(====,	
10	64.763	14.857	0.41	
20	59.007	10.680	1.40	
30	57.186	7.450	2.99	
40	56.118	4.933	5.13	
50	55.497	3.055	8.03	
60	55.032	1.510	11.34	
70	54.705	0.264	15.71	
90	54.246	-1.669	25.23	

TABLE 2

CONVERGENCE FOR UNACCELERATED COMPUTATION OF INNER PRODUCTS USING ROOFTOP FUNCTIONS

ACCELERATED RESULT: 53.184 - j7.415 OHMS

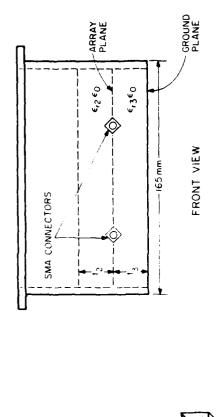
Upper limit on M,N	R jX (ohms)		cpu time (sec.)	
10	64.281	13.737	0.39	
20	58.636	9.122	1.31	
30	56.829	5.579	2.95	
40	55.770	2.856	5.10	
50	55.148	0.790	7.85	
60	54.682	-0.908	11.27	
7 0	54.350	-2.310	15.27	
90	53.876	-4.521	24.98	

3.1 Experimental verification

In order to test the moment method solution, several array configurations were tested in a waveguide simulator. The theory of the waveguide simulator has been described by Hannan [11], and will not be discussed here. The basic experimental setup is shown in Figure 3a, and a more detailed view of the array fixture is shown in Figure 3b. The array was scanned in the H-plane by varying the frequency, with the scan angle θ given by

$$\theta = \sin^{-1}(\lambda_0/2a)$$

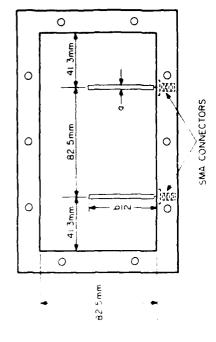
where a is the width of the wavequide in the H-plane, 165 millimeters. The frequency was varied from 0.92 GHz, just above the cutoff frequency, to 1.7 GHz, somewhat below the onset of the next propagating mode. The scan angle ranged from 81.2° at f = 0.92 GHz to 32.3° at f = 1.7 GHz. Two microstrip monopoles were fed through the waveguide wall using SMA connectors. From image theory, the impedance of each monopole is one half the impedance of the corresponding dipole. The elements were fed in phase and with equal amplitude by using a simple T connector. The balance of the T was tested and was found to be good. In order to simplify the construction of the array section and the array fixture, a very large cross section waveguide was used. Unfortunately a matched termination was not available, so a tapered resistive load was used as a The load was placed in the waveguide and adjusted for the best termination. match. However, the remaining mismatch caused fluctuations in the measured data, and was a major source of error. Other sources of error included the fitness of the dielectric substrate, losses in the waveguide walls, and very



Tapered Resistive Load ~

SMA Connectors

Automated Network Analyzer



TOP VIEW

Figure 3a. Waveguide simulator experimental set-up.

Figure 3b. Array fixture for waveguide simulator.

Dietectric

Array Fixture

Waveguide 82 5mm × 165mm × 2 53m importantly, the inability to calibrate the network analyzer over such a wide frequency range. The reflection coefficient measurement was referenced to the single end of the T connector, and the data was later referenced back to the feed point. To compare to measured data, the impedance of the corresponding dipole was calculated and divided by two to calculate the reflection coefficient of the monopole into a 50 ohm system.

Several array configurations were tested. Figures 4a and 4b give results for an array on 1 inch of rexolite, $\varepsilon_{\Gamma}=2.53$. The effect of the load mismatch is clearly seen in the magnitude plot, but in general agreement between measured and calculated results is good. Results for an array on a high dielectric constant substrate, $\varepsilon_{\Gamma}=6.0$, are shown in Figure 5a and 5b. The substrate was HI-K Styrene, with a nominal ε_{Γ} of 6.0. ε_{Γ} was approximately determined by measuring the resonant frequencies of a cavity filled with the material, and was in good agreement with the listed value, to within the margin of error caused by the eccentricities of the cavity. Again, the general agreement is good, and in particular the predicted blind angle is seen in the experimental results. The measured reflection coefficient does not reach 1 at the blind angle due primarily to losses in the guide and substrate, not included in the theory. The occurence of blind angles is discussed in the next section. Finally, Figures 6a through 6b present results for an array with a radome. This array was built on a 1 inch thick rexolite substrate with a 1 inch thick rexolite radome.

Overall, the agreement between experimental and theoretical results was good, considering the simple construction of the waveguide simulator. These results, along with the agreement with other computed results indicates that the solution accurately and efficiently predicts the input impedance of infinite arrays of microstrip dipoles.

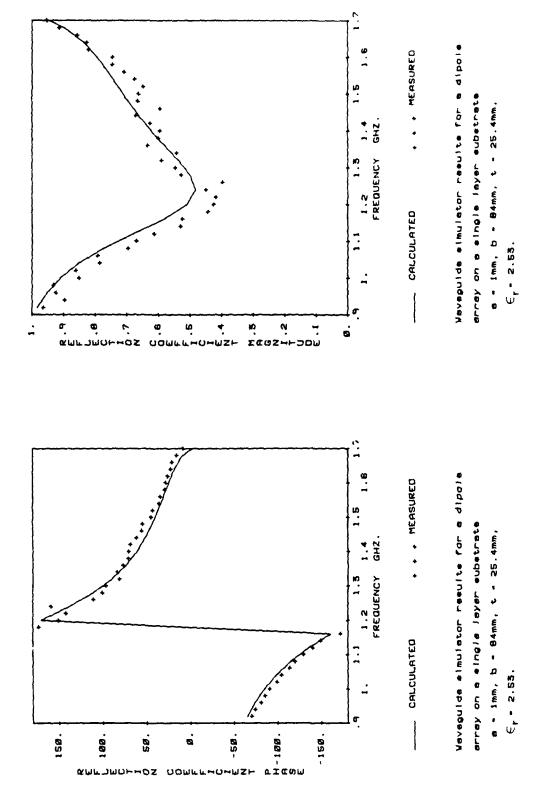


Figure 4a.

Figure 4b.

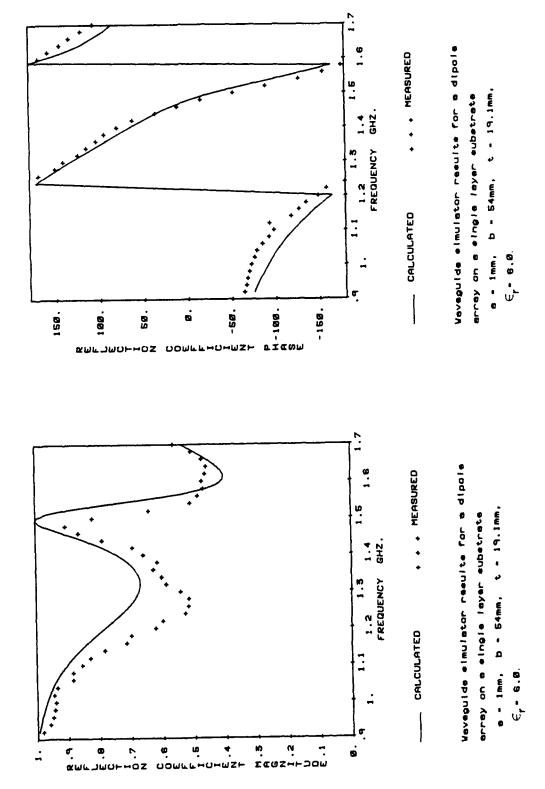
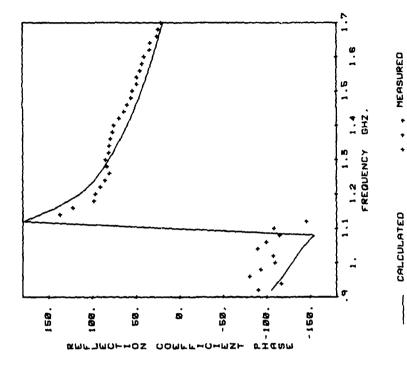
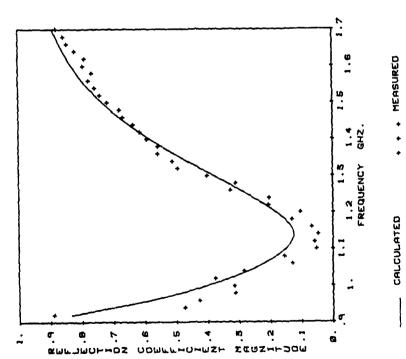


Figure 5a.

Figure 5b.







Veveguide elmulator resulte for a dipole array on a multi-layer substrate $a+1mm, \qquad b+95mm, \qquad t_3+25.4mm, \\ \in_{\Gamma_3}-1.055, t_5-25.4mm, \qquad \in_{\Gamma_2}-2.55.$

figure 6a.

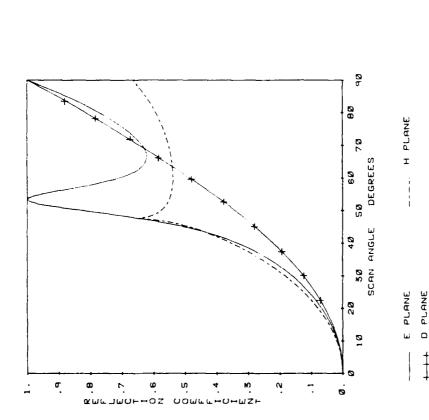
3.2 Numerical results

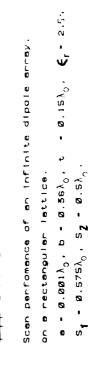
One of the most important characteristics of a phased array is its impedance or reflection coefficient as a function of scan angle. It has long been known that arrays which can support a slow wave can exhibit nulls at scan angle closer to broadside than the onset of a grating lobe [11,1]. In infinite arrays, these nulls become blind angles, with a reflection coefficient magnitude of 1. This behavior is thought to be due to a "forced" excitation of a surface wave on the array face [11]. For a microstrip array, the location of the blind angles can be predicted by the location of poles in the periodic Green's function which are not canceled by a zero in the numerator. Physically, these poles are the propagation constants of the surface waves of the grounded dielectric substrate (GDS). Through the use of the exact Green's funtion for the GDS the effect of the surface waves is built into the solution. However, a convenient construction for determining blind angles was suggested by Frazita [13], and used more recently by Pozar and Schaubert [10]. This construction, referred to as a surface wave circle diagram [13], is obtained by drawing grating lobe and surface wave circles around the lower order Floquet modes on a grating lobe (Floquet mode) diagram. When a surface wave circle intersects the visible region, blindness will occur at the corresponding scan angles unless cancellation occurs.

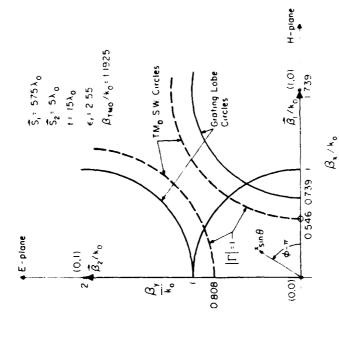
While the basic features of the array are easily predicted by the surface wave circle diagram or the grating lobe diagram, the moment method solution not only accounts for these features but accurately predicts the shapes and magnitudes of the peaks, and the reflection coefficient at all other points. As an example, consider a microstrip dipole array in a rectangular lattice, with $S_1 = 0.575\lambda_0$, $S_2 = 0.5\lambda_0$, $t = 0.15\lambda_0$, and $\varepsilon_r = 2.55$. No radome was present in this

example. For this GDS only the TM surface wave mode is above cutoff, and it has a normalized propagation constant β_{gw}/k_0 = 1.1925. The elements were of dimensions $a = 0.001 \lambda_0$ and $b = 0.36 \lambda_0$, giving a broadside impedance of 71.8 + j3.9 ohms, using 11 edge mode basis functions. The reflection coefficient versus scan angle in the E, H and D planes is shown in Figure 7. An examination of Figure 8 easily explains the coarse characteristics of the results in Figure 7. In the H-plane scan ($\phi = 0$), the intersection with the TM surface wave pole at sin $\theta = 0.739$, or $\theta = 33.1$ degrees does not cause blindness because the (1,0) Floquet mode has zero amplitude for an H-plane scan. In fact for H-plane scans the TM surface wave poles are not excited and for E-plane scans the TE surface wave poles are not excited, due to the polarization of the electric field in those planes. However, returning to Figure 7, a grating lobe (Floquet mode) enters visible space at θ = 47.6 degrees in the H-plane scan, resulting in the observed peak. The excitation of the TM surface wave at $\theta = 53.9$ degrees causes the observed blind angle in the E-plane. The D-plane (ϕ = 45 degrees) scan is smooth, as no surface wave or grating lobe cirles are intersected. At endfire scan ($\theta = 90$ degrees) in the E and D planes $|\Gamma| = 1$, as the array spacing is such that no Floquet modes are propagating (in free space.)

In the next example, the array of the previous example is covered with a dielectric layer (radome) of thickness $0.1\lambda_0$ and dielectric constant 2.55. The broadside impedance of this array was 50.1 + j 143.2 ohms. The results for this array are plotted in Figure 9. Because of the additional layer, a second surface wave is permitted, the TE₀ mode, as shown in Figure 10. In the H-plane scan, a blind angle occurs at $\theta = 42.0$ degrees due to the excitation of the TE₀ surface wave mode. In addition, a grating lobe enters visible space for $\theta = 47.7$ degrees. The result of these two factors is a broadly peaked blind angle.





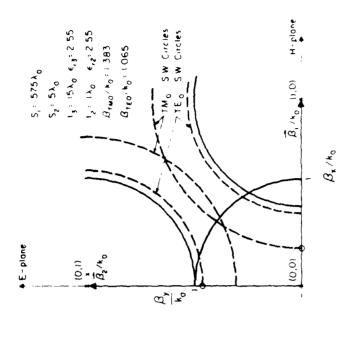


1

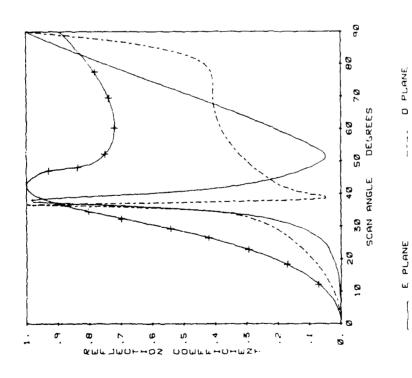
.

Figure 8. Surface wave circle diagram for array of Figure 7.

Figure 7.







Scan perfowence of an infinite dipole array. with a radome on a rectangular lattice. $\mathbf{e} = \mathbf{0.001} \lambda_0, \ \mathbf{b} = \mathbf{0.56} \lambda_1, \ \mathbf{t_3} = \mathbf{0.15} \lambda_1, \ \mathbf{f_{13}} = 2.5 \lambda_1, \ \mathbf{t_3} = \mathbf{0.15} \lambda_2, \ \mathbf{f_{13}} = \mathbf{0.55} \lambda_3, \ \mathbf{f_{13$

+++ H PLANE

Figure 9.

In contrast, the blind angle in the D-plane at θ = 36.7 degrees, and the blind angle in the E-plane at 38.1 degrees, both due to excitation of the TM surface wave mode, are very sharply peaked, resulting in a low reflection coefficient over a much broader range than in the H-plane.

4.0 INFINITE ARRAYS OF MICROSTRIP PATCHES

The solution for microstrip patches is considerably more involved than the dipole arrays of the previous section because one must include currents in both the \hat{x} and \hat{y} directions and because of the difficulty in adequately representing the complicated current distribution near the feed region. Rooftop basis and testing functions were used for all patch results. The general layout of the basis functions is illustrated in Figure 11.

Several feed current distributions were tried. Ideally a cylindrical probe would be used to model the coaxial feed probe. However, to facilitate the evaluation of the excitation matrix elements, a square current distribution was used. Because the feed currents are not included in the integral equation, the self impedance of the feed probe is added to the patch impedance as a correction factor. The self impedance per unit length of an infinite wire is given by [14,15]

$$X_{L} = \frac{\eta_{o}t}{\lambda_{o}} \ln \left[\frac{1}{2\pi E_{w}\sqrt{\varepsilon_{r}} \cdot 0.5902} \right]$$

where n_C is the intrinsic impedance of free space, and E_W is the half-width of the feed. The factor of 0.5902 is the equivalent radius of a square of side length 1, based on equal static capacitances [16]. This approximate correction, not strictly applicable here, is used in an attempt to compensate for the use of a square current distribution.

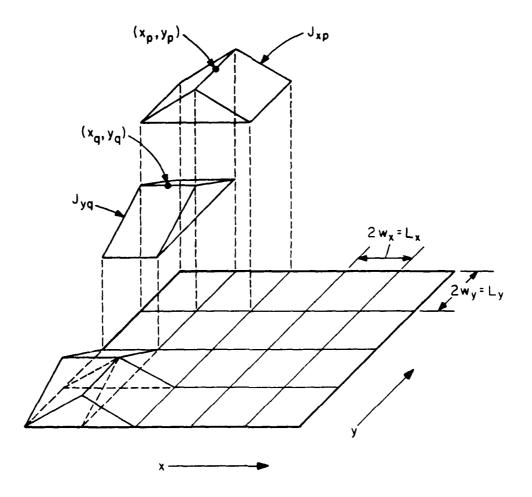
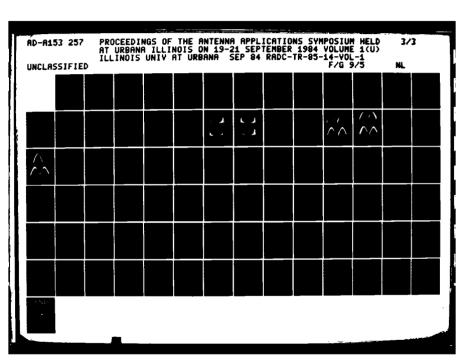


Figure 11. Basis function layout on microstrip patch.

Unfortunately no computed or measured results for the impedance of large microstrip arrays using individual probe feeds could be found in the literature. Instead, the patch results were checked by comparing to computed current distributions for single square plates in free space excited by a normally incident plane wave [17,18]. For patch spacings of approximately two wavelengths or more, and similar heights above the ground plane, the array results agreed well with the single square plate results.

Various theoretical results were computed for arrays of microstrip patches. As one example, consider a probe fed microstrip patch array on a rectangular lattice with $S_1 = S_2 = 0.5\lambda_0$, $t = 0.1\lambda_0$ and $\varepsilon_r = 2.53$. The patch was $0.3\lambda_0$ square, and was fed in the center of one side, 0.045 from the edge. The feed had a half-width of $0.025\lambda_0$. Such a large feed was used to get convergence in a reasonable number of basis functions. Thin feeds are handled just as easily, except that more basis functions are required to represent the resulting current distribution. Using ll subpatches in each direction, and including the excitation matrix, a total of 335 distinct matrix elements need to be evaluated for the zero phase shift case. Using the 64 point Gaussian quadrature, the average time to evaluate the matrix elements was 0.043 second. Table 2, without any accleration approximately one second per matrix element was required, using rooftop basis functions and linear triangle testing, only slightly less smooth than this case. The same problem would then require approximately 6.5 minutes of execution time on the CDC 6600. The current distribution on the patch is shown in Figures 12a and 12b. The imaginary component of the y directed current is very smooth, and probably can be adequately represented with one sinusoidal mode, assuming the effect of the edge condition can be neglected, as concluded by Deshpande and Bailey [15]. The real





MICROCOPY RESOLUTION TEST CHART
NATIONAL BUREAU OF STANDARDS-1963-A

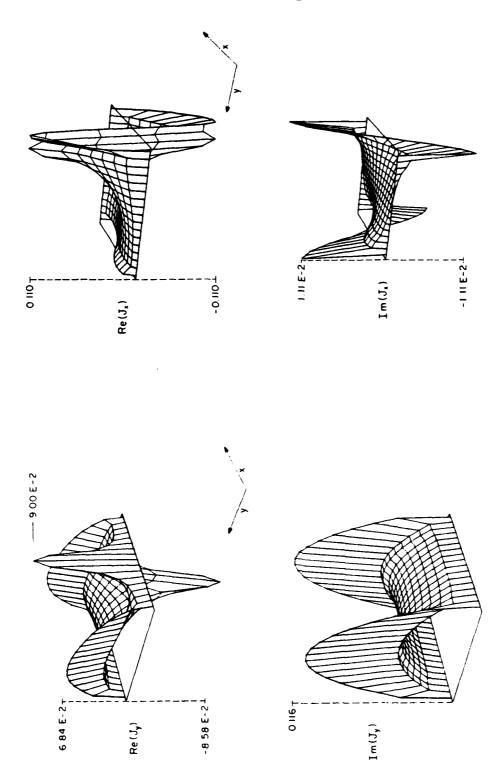


Figure 12. Current on a probe fed microstrip patch.

component, on the other hand is dominated by the peaked behavior in the feed region. Similarly, the real component of the x directed current is essentially zero everywhere but at the edges and near the feed point. These results clearly illustrate the major difficulty in analyzing probe fed patch arrays in thick substrates; in order to adequately model the current distribution a large number of basis functions is required. One possible alternative, extracting the feed region current with a seperate basis function, would leave a relatively smooth current which could be represented with relatively few basis functions. This would help alleviate the matrix storage problem which arises with the present technique.

Results for the impedance as a function of frequency for two probe-fed microstrip patch arrays are shown in Figures 13 and 14. The array dimensions are chosen such that at 0.9 GHz the dimensions are the same as in the previous example. Two substrate thicknesses were used, $t = 0.08 \, \lambda_0$ and $t = 0.1 \, \lambda_0$, at 0.9 GHz. In both Figures 13 and 14 the 10 plotted points are, proceeding clockwise, 0.7 to 1.0 Ghz by 0.05 GHz, and 1.1, 1.2 and 1.25 GHz. As expected for these patches on thick substrates, the impedance curves are on the inductive side of the Smith chart. Consistent with this, the array on the thicker substrate is more inductive.

5.0 CONCLUSIONS

A moment method solution for infinite arrays of microstrip dipoles and patches on thick substrates has been developed. By using the infinite array approach and the periodic Green's function for the grounded dielectric substrate, mutual coupling effects, including blind angles, are rigorously and efficiently included. A series of waveguide simulator experiments was performed, and good agreement was found between experimental and theoretical results.

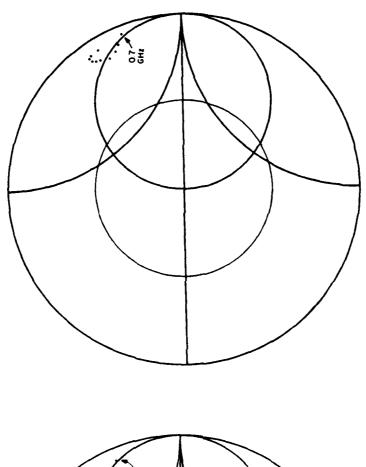


Figure 14. Impedance of a microstrip patch on a thick substrate. $(Z_0 = 50\Omega)$ t = 33.3mm, $\epsilon = 2.53$

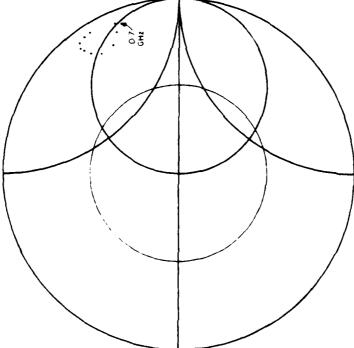


Figure 13. Impedance of a microstrip patch on a thick substrate. ($Z_0 = 50\Omega$) t = 26.7mm, ϵ = 2.53, $S_1 = S_2 = 167mm$, a = b = 100mm.

by using efficient summation techniques the solution is more than an order of magnitude more efficient than similar solutions using the infinite array approach. This improved efficiency should allow the analysis of more complicated microstrip antennas than was previously practical, such as antennas with slots, stubs or parasitic elements.

REFERENCES

- [1] R. C. Hansen (Ed.), Microwave Scanning Antennas, Vol. II: Array Theory and Practice. New York: Academic Press, 1966.
- [2] R. F. Harrington, Field Computation by Moment Methods. New York: MacMillan, 1968.
- [3] W. F. Richards, J. R. Zinecker, D. R. Wilton, S. Singh, Y. T. Lo and S. M. Wright, "Acceleration of periodic Green's Functions in Free Space," URSI Symposium Proceedings, Houston, TX, p. 81, May 23-26, 1983
- [4] S. M. Wright, Y. T. Lo, W. F. Richards and J. R. Zinecker, "Efficient evaluation of the periodic Green's function for a grounded dielectric substrate," <u>URSI Symposium Proceedings</u>, Houston TX, page 83, May 23-26, 1983.
- [5] D. R. Wilton, S. Singh and W. F. Richards, "Application of series acceleration techniques to problems involving periodic media," <u>URSI Symposium Proceedings</u>, Houston TX, page 82, May 23-26, 1983.
- [6] S. M. Wright and Y. T. Lo, "Efficient analysis for infinite microstrip dipole arrays," Electronic Letters, vol. 19, no. 24, pp. 1043-1045, November 24, 1983.
- [7] S. M. Wright, "Efficient analysis of infinite microstrip arrays on thick substrates", Ph.D. Thesis, Urbana, Il., 1984.
- [8] L. Stark, "Radiation impedance of a dipole in an infinite planar phased array," Radio Science, vol. 1, pp. 361-377,

- [9] D. M. Pozar and D. H. Schaubert, "Scan blindness in infinite phased arrays of printed dipoles," personal communication, September 21, 1983.
- [10] D. M. Pozar and D. H. Schaubert, "Analysis of infinite phased arrays of printed dipoles," <u>IEEE/AP-S Symposium Proceedings</u>, Boston MA, pp. 737-740, June 1984.
- [11] P. W. Hannan and M. A. Balfour, "Simulation of a phased-array antenna in a waveguide," IEEE Trans. Antennas Propagat., vol. AP-13, pp. 342-353, May 1965.
- [12] G. H. Knittel, A. Hessel and A. A. Oliner, "Element pattern nulls in phased arrays and their relation to guided waves," Proc. IEEE, vol. 56, no. 11, pp. 1822-1836, Nov. 1968.
- [13] R. F. Frazita, "Surface-wave behavior of a phased array analyzed by a grating-lobe series," <u>IEEE Trans. Antennas Propagat.</u>, vol. AP-15, pp. 823-824, Nov. 1967.
- [14] E. C. Jordan and K. G. Balmain, <u>Electromagnetic Waves and Radiating Systems</u>. New Jersey: Prentice Hall, 1968.
- [15] M. D. Deshpande and M. C. Bailey, "Input impedance of microstrip antennas," IEEE Trans. Antennas Propagat., vol. AP-30, no. 4, pp. 645-650, Nov. 1982.
- [16] Y. T. Lo, "A note on the cylindrical antenna of noncircular cross section," J. Appl. Phys., vol. 24, pp. 1338-1339, October, 1953.
- [17] A. W. Glisson and D. R. Wilton "Simple and efficient numerical methods for problems of electromagnetic radiation and scattering from surfaces," IEEE Trans. Antennas Propagat., vol AP-28, no. 5, pp. 593-603, Sept. 1980.
- [18] A. W. Glisson, "On the development of numerical techniques for treating arbitrarily shaped surfaces," Ph.D. Dissertation, University of Mississippi, 1978.

CIRCULARLY POLARIZED MICROSTRIP ANTENNAS

Y. T. Lo B. Engst

Electromagnetics Laboratory University of Illinois Urbana, IL

R. Q. H. Lee

Lewis Research Center NASA Cleveland, OH

I. Introduction

It is well known that a simple microstrip antenna can be made to radiate EM waves of any polarization, in particular, the circular polarization (CP) without any phasing network and power divider [1 - 5]. A simple but surprisingly accurate theory for this family of antennas has been developed and reported in the 1979 Antenna Applications Symposium. However, the CP bandwidth, (CPBW) namely the bandwidth in which the axial ratio (AR) is less than a certain specified value, say 3 dB, is very small. For example, for a nearly square patch made of 1/16" thick Rexolite 2200 and designed to operate at 800 MHz, the CP bandwidth is only about 0.3%. Most of those experimental designs were made for a feed placed along the diagonal of the patch. But the theory shows that there are practically infinitely many possible designs with different feed locations [3 - 5]. The purposes of this paper are: first to clear up the speculation that other designs might give a wider bandwidth, and second to show an effective method for broadening the bandwidth.

II. Theory

First we briefly review the theory for CP microstrip antennas [3]. For concreteness, let us consider a rectangular patch with effective dimensions a \times b, relative substrate dielectric constant ε_{r} , and effective loss tangent δ_{eff} which can be either computed or simply measured from the Q-factor of the antenna. In general, an infinite number of modes will be excited. However, as the excitation frequency ω is near the resonant frequency of one of the modes, say the mnth mode:

$$\omega = \omega_{mn} = \left\{ \frac{1}{\mu_0 \varepsilon_0 \varepsilon_r} \left[\left(\frac{m\pi}{a} \right)^2 + \left(\frac{n\pi}{b} \right)^2 \right] \right\}^{1/2} = \frac{1}{\sqrt{\mu_0 \varepsilon_0 \varepsilon_r}} k_{mn}$$
 (1)

the mnth modal field will overwhelmingly dominate over all others, particularly for thin microstrip antennas. The radiated field is then found to be inversely proportional to $(k-k_{mn})$ where $k=\omega/\mu_0\varepsilon_0\varepsilon_\Gamma(1-j\delta_{eff})\approx k_0/\varepsilon_\Gamma(1-j\delta_{eff}/2)=k_0/\varepsilon_\Gamma(1-j/2Q)\approx k'+jk''$. Now let us consider a nearly square patch, namely 0 < a-b=c < < a and b; then for the two dominant modes,

$$k_{01} = \pi/b = k_{10} = \pi/a$$
 (2)

If the excitation frequency is such that

$$k_{10} < k' < k_{01}$$
 , (3)

then the fields associated with both of these modes will be strongly excited.

Let the normal of the patch be the z-axis, the patch side having dimension a be along the x-axis and b along the y-axis. The radiated field along the z-axis will have two orthogonal components whose ratio is approximately given by

$$\frac{E_{\mathbf{y}}}{E_{\mathbf{x}}} \approx A \frac{k - k_{10}}{k - k_{01}} \tag{4}$$

where

$$A = \frac{\cos(\pi y^{t}/b)}{\cos(\pi x^{t}/a)}$$
 (5)

$$(x',y')$$
 = coordinates of the feed location . (6)

If a, b, x', and y' are such that

$$E_{y}/E_{x} = \pm j \quad , \tag{7}$$

then LH and RH CP will be obtained, respectively. To see how the design parameters a, b, x', and y' are related, it is not only the simplest but also the most illuminating method by examining (4) and (7) in the k-plane as shows in Figure 1.

For LHCP the phasor $(k-k_{10})$ must lead $(k-k_{01})$ by $\pi/2$ and the ratio of their lengths must be equal to 1/A. For given a and b, the solution for k' is given by the intersection of the circle whose diameter is $(k_{01}-k_{10})$ and center at $(0,(k_{01}+k_{10})/2)$ and the line k''/k'=-1/2Q. Clearly these are three possibilities: (1) no solution if $(k_{01}-k_{10})<2k''=k'/Q=k_{10}/Q$; (2) one solution if $(k_{01}-k_{10})=2k''=k_{10}/Q$; and (3) two solutions if $(k_{01}-k_{10})>2k''=k_{10}/Q$.

Let us consider the last case first. Using the similarity of triangles one readily obtains the following:

$$\frac{p}{|k-k_{10}|} = \frac{|k''|}{|k-k_{01}|} \implies p = |k''|/A$$
 (8)

$$\frac{q}{|k-k_{01}|} = \frac{|k''|}{|k-k_{10}|} \implies q = |k''|A \qquad (9)$$

where p and q are $(k' - k_{10})$ and $(k_{01} - k')$, respectively, as indicated in Figure 2, and

$$A = |k - k_{01}|/|k - k_{10}| \tag{10}$$

as from (4) and (7). One of the two possible solutions for k' is

$$k' = k_{10} + p = k_{10} + \frac{k'}{2QA}$$
 => $k' = k_{10} / \left(1 - \frac{1}{2QA}\right)$. (11)

Furthermore,

$$k_{01} - k_{10} = p + q = |k''| \left[A + \frac{1}{A} \right] \simeq \frac{k_1}{2Q} \left[A + \frac{1}{A} \right] .$$
 (12)

From (11) and (12), one obtains an equation for A:

$$A^2 - \frac{2Qc}{b}A + \left(1 + \frac{c}{b}\right) = 0 \tag{13}$$

Thus there are, in general, two possible solutions for A which will be denoted by A_1 and A_2 . From (13)

$$A_1 A_2 = 1 + \frac{c}{b} = 1 . {14}$$

Thus, when $c \ll b$ if A_1 is a solution, so is $1/A_1$. The latter when substituted into (11) gives the corresponding second solution of k':

$$\mathbf{k}^{\dagger} = \mathbf{k}_{10} / \left(1 - \frac{\mathbf{A}}{2\mathbf{Q}} \right) . \tag{15}$$

Equations (13) and (11) are the two basic design formulas. For example, for a given material and given dimensions a and b, Q can be either computed or measured [3]. Then (13) is solved for the two solutions of A, each of which determines the feed locus and its corresponding frequency from (11). Since for $c \ll b$, $A_1A_2 = 1$, the two loci for the two frequencies are approximately symmetrical with respect to the line x = y.

For RHCP, the lower sign of (7) should be used. Then by defining

$$A = -\frac{\cos(\pi y^{\dagger}/b)}{\cos(\pi x^{\dagger}/a)} \tag{16}$$

all the above derivations and, therefore, all the above results remain unchanged. In other words the feed loci for RHCP are simply the reflections of those for LHCP with respect to the line x = a/2, or y = b/2. These will be demonstrated later in some examples.

For the special case $A_1 = A_2 = 1$, i.e., the feed is along the diagonal line y'/x' = b/a, (13) reduces to

$$\frac{a}{b} = \frac{2Q+1}{2Q-1} = 1 + \frac{1}{Q} + \frac{1}{2Q^2} . \tag{17}$$

and the circle in Figure 1 becomes tangent to the line k''/k' = -1/2Q.

IV. Numerical and Experimental Results

Several experimental patch antennas were designed and tested. All of them were made of Rexolite 2200 with ϵ_r = 2.62 and dielectric loss tangent 0.001. One of them has the following physical dimensions:

a = 16.1 cm, b = 15.9 cm, t = 0.32 cm.

Past results show that the effective values of a and b are about 1.5t larger than the actual physical dimensions. The Q of this patch is found to be about 100. Using (13) the four feed loci, two at f_1 and f_2 for LHCP and two others also at f_1 and f_2 for RHCP were computed and plotted in Figure 2. The patterns measured with a rotating dipole for feed points 1 and 2 at 597 MHz and 590.4 MHz, respectively, are shown in Figures 3(a) and 3(b). These patterns are about the same as those reported earlier for the patches designed for A = 1. For the feed at point 2, the AR vs. f is listed in Table 1. The CP bandwidth is about 0.5%. An attempt to broaden the bandwidth by feeding the patch at a compromise point between points 1 and 2 was found ineffective and sometimes resulting in worse AR. The input impedance characteristic for feed at 1 and 2 are shown in Figures 4(a) and 4(b).

V. Broadbanding of CP Microstrip Antennas

Assuming that the dimensions of a CP patch antenna have been determined by using the design formula given above, one can then compute the CP bandwidth by using (4) as the frequency, or k', departs from the designed value until the AR becomes 3 dB. Using this method we have previously shown that the CP bandwidth is approximately (35/Q) percent for Rexolite 2200 [3]. Thus to broaden the

bandwidth, Q must be lowered. This can only be achieved effectively by using thick substrate [6]. Unfortunately, so far there is no theory available for thick CP microstrip antennas, nor a precise knowledge about the upper limit of the substrate thickness beyond which the cavity-model theory breaks down. Under this circumstance we simply used the latter theory to design several patch antennas with thickness as much as $0.053 \lambda_0$, (λ_0 = free space wavelength) or 0.084λ , (λ = substrate dielectric wavelength). To our surprise excellent results could still be obtained. This is discussed below with several examples.

(a) The first patch, designed to operate in the 10 GHz range, has the following physical dimensions:

$$a = 0.946$$
 cm, $b = 0.911$ cm, $t = 0.08$ cm

and its Q-factor is found to be about 20. Using (13) one finds that the proper feed location is along the diagonal of the patch. For a good match to the 50 Ω line, the feed coordinates are chosen to be

$$x' = 0.21$$
 cm, $y' = 0.2$ cm.

The measured patterns at 10.22 GHz in the two planes $\phi = 0^{\circ}$ and 90° are shown in Figures 5a. Excellent AR is observed over a wide angular region. Figures 5b – 5c show the patterns in the $\phi = 0^{\circ}$ plane at the two edge frequencies, 10.306 and 10.16 GHz, of the CP bandwidth, which is about 1.44%, substantially larger than that obtained earlier for the thin substrate. But in this case t $\approx 0.044 \ \lambda$.

(b) The second patch has the following physical dimensions:

$$a = 0.964$$
 cm, $b = 0.859$ cm, $t = 0.16$ cm

Its Q is found to be 8 and $(x^*,y^*) = (0.3, 0.28)$ cm. The patterns for 9.74 GHz in the two principal planes and for the two edge frequencies, 9.9 and 9.577 GHz,

of the CP band in the ϕ = 0° plane are shown in Figures 6a - 6c. For this thick substrate, the CPBW is about 3.3%.

All of these results as well as a few others are summarized in Table 2. The CP bandwidth vs. t in λ or λ_0 is plotted in Figure 7. It is interesting to note that their relationship is nearly linear and can be given approximately by

CPBW(%) =
$$36.7t(\lambda) + 0.16$$
 for t > 0.005λ .

Earlier we showed that the CPBW (in %) is approximately equal to 35/Q. This is plotted in Figure 8 where the experiment results are also marked. The agreement is surprisingly good.

- (c) The last example has the physical dimensions
- a = 1.088 cm, b = 0.90 cm, t = 0.08 cm.

These dimensions result a feed point at x' = 0.2 cm, y' = 0.39 cm which is not on the diagonal line. The patterns are shown in Figures 9a - 9c for f = 10.27, 10.18, and 10.36 GHz, the latter two being the edge frequencies of the CPBW of about 1.75%. The small improvement of this BW over that of the design (a) with the feed along the diagonal line is probably within our experimental error and should not be taken seriously.

VI. Conclusions

- (1) Despite the fact that our CP microstrip antenna theory is based on the cavity model, valid only for thin substrate, this investigation shows that it is still applicable for substrate as thick as 0.084 of a dielectric wavelength.
- (2) The CP bandwidth of a microstrip antenna depends mainly on its Q-factor, thus its thickness. A CPBW of 3% can be obtained if the substrate is about 8% of a dielectric wavelength thick. For this case Q \approx 8, indicating a very good radiation efficiency.

(3) For a fixed thickness, the CPBW cannot be broadened significantly by using other designs. However, other designs do provide a means for moving the feed from one point to some other point which may be necessary, due to some packaging problem.

VII. References

- [1] H. D. Weinschel, "A cylindrical array of circularly polarized microstrip antennas," IEEE AP-S International Symposium Digest, pp. 175-180, June 1975. Urbana, IL.
- [2] J. L. Kerr, "Microstrip polarization techniques" Proc. of the 1978 Antenna Applications Symposium at Allerton Park, University of Illinois, Urbana, IL.
- [3] Y. T. Lo, W. F. Richards, and D. D. Harrison, "An improved theory for microstrip antennas and applications Part I," Interim Report,

 RADC-TR-79-111, May 1979; also W. F. Richards, Y. T. Lo and D. D. Harrison,

 "An improved theory for microstrip antennas and applications," <u>IEEE Trans.</u>,

 AP-29, pp. 38-46, Jan. 1981.
- [4] W. F. Richards, Y. T. Lo, and P. Simon, "Design and theory of circularly polarized microstrip antennas," IEEE AP-S International Symposium Digest, pp. 117-120, June 1979.
- [5] Y. T. Lo and W. F. Richards, "A perturbation approach to the design of circularly polarized microstrip antennas," IEEE AP-S Inernational Symposium, pp. 339-342, June 1981.
- [6] Y. T. Lo, et al., "Study of microstrip antenna elements, arrays, feeds, losses, and applications," Final Technical Report, RADC-TR-81-98, June 1981.

Acknowledgement

This work is supported by Lewis Research Center, NASA, Cleveland, OH and RADC Hanscom AFB, MA.

TABLE 1.

AR vs. frequency of the microstrip antenna shown in Figure 2 and fed at point 2: x' = 6.75 cm, y' = 5.1 cm

f (MHz)	AR (dB)		
588.96	3		
589.3	2.5		
589.8	1.5		
590.4	1		
591.2	1.4		
591.8	2.7		
592	3		

TABLE 2.

Measured CP bandwidths for various substrate thicknesses t

f (GHz)	λ _o (cm)	t(cm)	t(\(\lambda_0\)	t(λ)	CPBW(%)	Q
0.59	50.85	0.16	0.0032	0.0051	0.35	130
0.59	50.85	0.32	0.0063	0.01	0.5	100
1.200	25	0.32	0.0128	0.021	0.84	58
10.22	2.935	0.08	0.0273	0.044	1.44	20
9.74	3.093	0.16	0.053	0.084	3.3	8

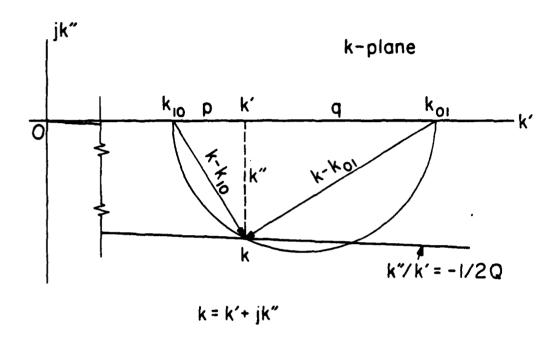


Figure 1. Geometric relations of phasors $\mathbf{k}_{10},\ \mathbf{k}_{01}$ and \mathbf{k} in k-plane for CP operation.

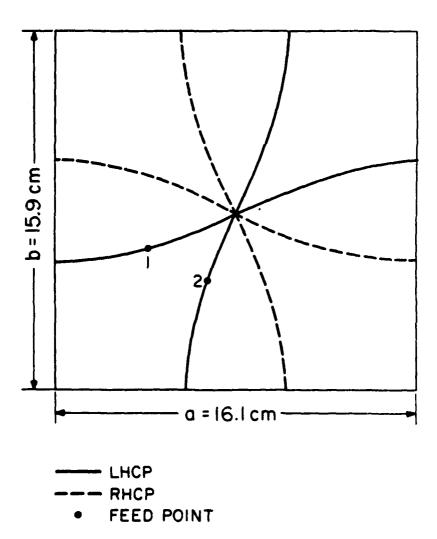


Figure 2. Feed loci for a rectangular CP microstrip antenna with substrate thickness 0.32 cm and relative dielectric constant 2.62.

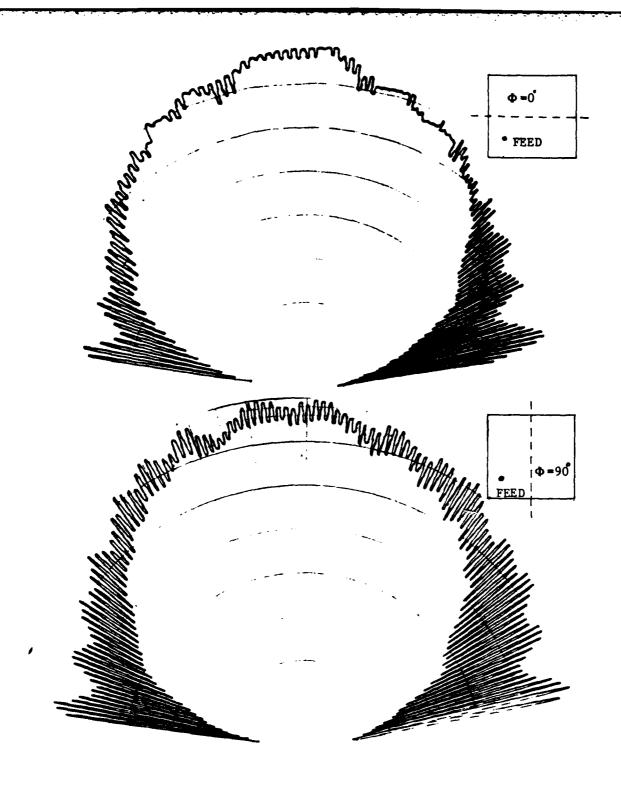


Figure 3(a). Field patterns in principal planes of the microstrip antenna shown in Figure 2, at point 1: x' = 4.55 cm, y' = 6.37 cm, and f = 597 MHz.

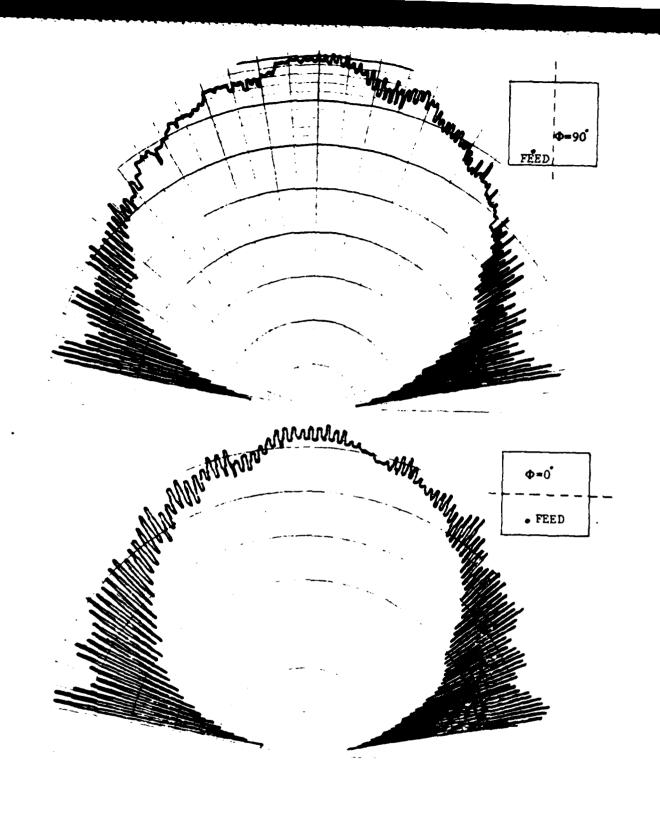
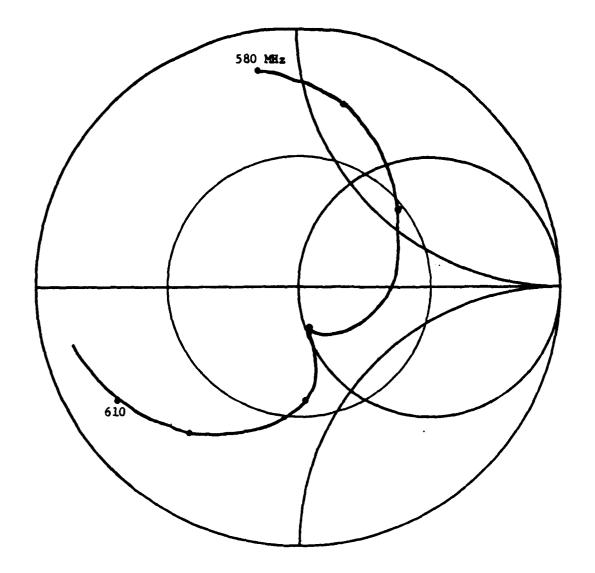
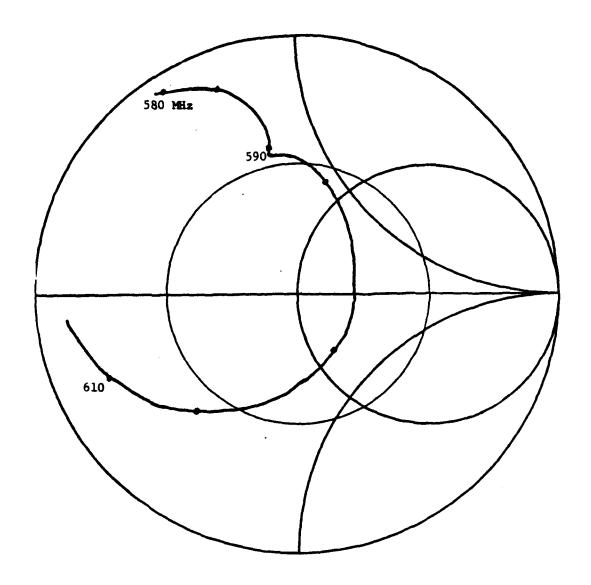


Figure 3(b). Field patterns in principal planes of the microstrip antenna shown in Figure 2, at point 2: x' = 6.75 cm, y' = 5.1 cm, and f = 590.4 MHz.

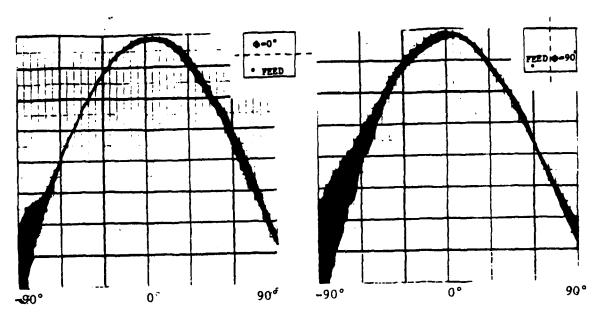


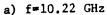
a) Impedance locus, frequency increment = 5 MHz.

Figure 4. Input impedance of the antenna shown in Figure 2 and fed at point (a) 1 and (b) 2.



b) Impedance locus, frequency increment = 5 MHz.





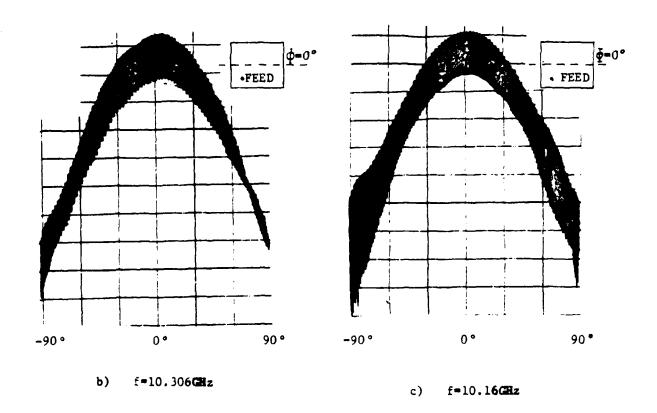
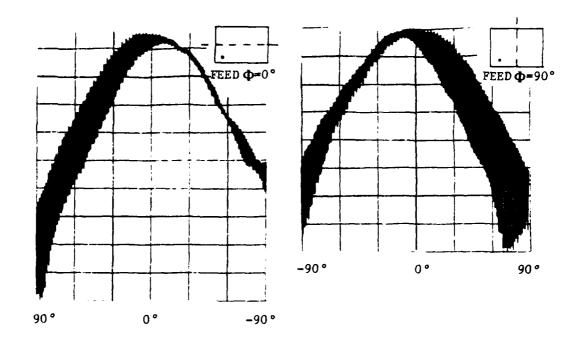


Figure 5. Field patterns in principal planes shown of the micrstrop antenna with dimension a=0.946 cm, b=0.911 cm, t=0.08 cm, and feed point at x'=0.21 cm, y'=0.2 cm.



a) f=9.74GHz

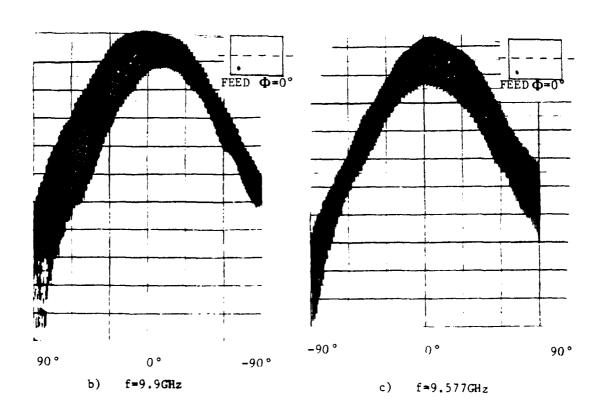


Figure 6. Field patterns in principal planes shown of the microstrip antenna with dimension a=0.964 cm, b=0.859 cm, t=0.16 cm, and feed point x'=0.3 cm, y'=0.28 cm.

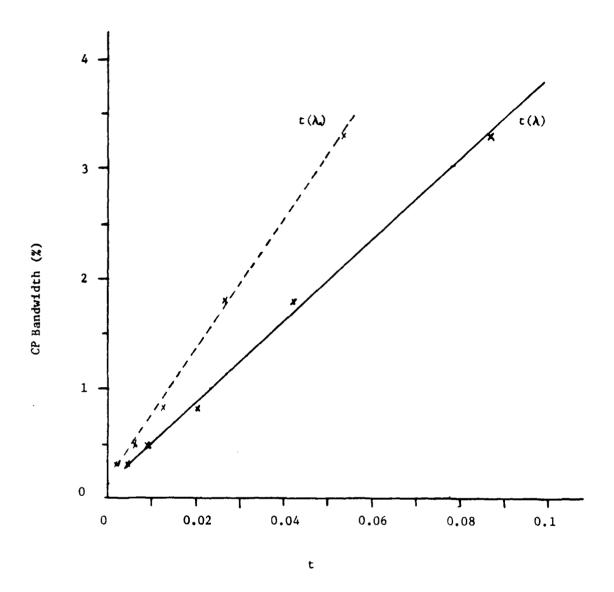


Figure 7. Bandwidth vs. the substrate thickness t, expressed in terms of free space wavelength, λ_0 , or substrate dielectric wavelength λ .

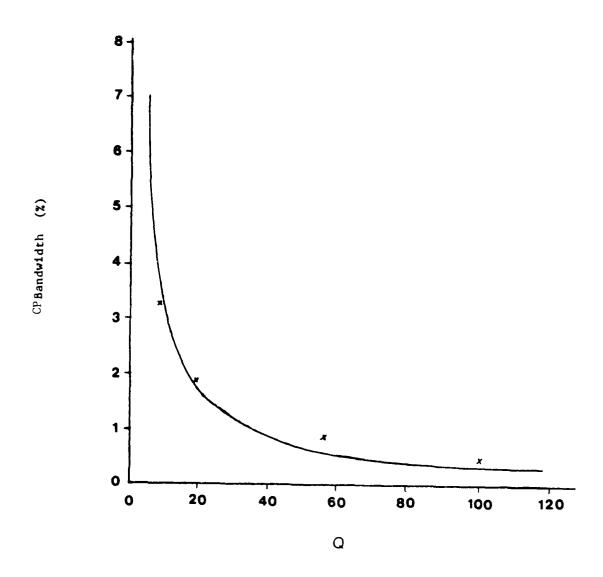
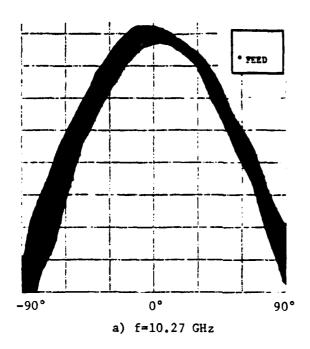


Figure 8. CP bandwidth vs. the quality factor Q.

Theory
xxx Experiment



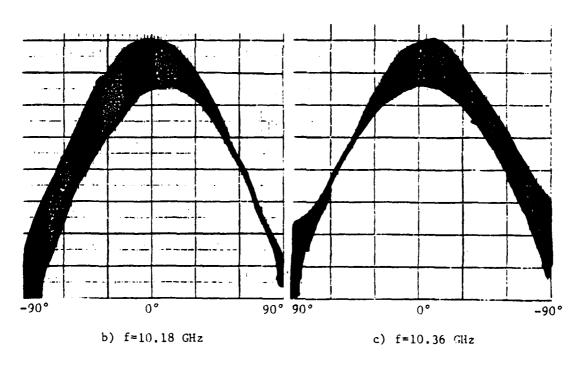


Figure 9. Field patterns of the microstrip antenna with dimension a = 1.088 cm, b = 0.90 cm, t = 0.08 cm, and feed point at x' = 0.2 cm, y' = 0.39 cm. All patterns were taken for ϕ = 0°.

Radiation and Scattering Performance of Microstrip Antennas Using Exotic Substrates*

J. J. H. Wang Engineering Experiment Station Georgia Institute of Technology Atlanta, Georgia 30332

ABSTRACT

Both the scattering and radiation properties are considered in microstrip antenna designs for airborne applications. The use of exotic substrates, instead of simple dielectric substrates, opens up a new dimension, making it much easier to meet both the radiation and scattering requirements. Two types of substrates, the ferromagnetic and the anisotropic dielectric, are being studied because of their commercial availability. It has been observed that the radiation mode and the scattering mode of the microstrip antenna are often distinctly different. Thus, permittivity and permeability tensor of the substrate can be selected to decouple the radiation and scattering modes to achieve simultaneously radiation and scattering performance goals. Analysis techniques used in the design study are also discussed.

1. Introduction

Recently, the use of "exotic" substrates in microstrip

^{*}This research was supported by the Electromagnetic Sciences Division of Rome Air Development Center, Hanscom AFB, USAF Systems Command under Contract F19628-84-K-0010.

antennas has gained recognitionn as a new way to improve their performances [1,2]. In this paper, we will concentrate in substrates that can act on both the radiation (antenna) and scattering modes of the antenna in different manners so that both the radiation and the scattering performances of the antenna can be simultaneously improved. That this is possible is due to the fact that the radiation and scattering modes of the microstrip antenna are substantially decoupled from each other.

It is conceivable that many possibilities exist in the use of exotic substrates in microstrip antennas. We will, however, focus on the use of uniaxial anisotropic substrates which are suitable for the improvement of radiation and scattering characteristics.

2. Microstrip Antennas Using Uniaxial Anisotropic Substrates

Figure 1 depicts a microstrip antenna covered with a radome.

Both the radome and the substrate are, in general, bianisotropic or anisotropic, but is assumed to uniaxial anisotropic with

$$\underline{\underline{\varepsilon}} = \begin{bmatrix} \varepsilon_{t} & 0 & 0 \\ & \varepsilon_{t} \\ 0 & 0 & \varepsilon_{z} \end{bmatrix}$$
and $\mu = \mu_{0}$. (1)

Since practical microstrip structures are invariably thin, the electric field in the substrate and the radome has only a z component, that is,

The radiation (antenna) mode of the microstrip antenna can be supported by choosing $\epsilon_{\rm Z}$ to be low loss. The scattering mode of the microstrip antenna can be examined by assuming an incident field

$$\underline{\mathbf{E}}^{\mathbf{i}} = \mathbf{E}^{\mathbf{i}} \left[\mathbf{p} \ \hat{\mathbf{t}} + (1-\mathbf{p}) \ \hat{\mathbf{z}} \right]$$
 (3)

(2)

where $l > p > \cos\theta_i$,

and t is a unit vector perpendicular to $\hat{\mathbf{z}}$. θ_i is the incident angle between $\hat{\mathbf{z}}$ and the direction of incident wave propagation. P is a polarization factor, being 1 for TE wave and $\cos\theta_i$ for TM wave. When θ_i is small, $\underline{\mathbf{E}}^i$ is primarily $\hat{\mathbf{t}}$ polarized. Thus, $\varepsilon_{\hat{\mathbf{t}}}$ can be chosen to yield the favored scattering properties without affecting much the radiation property of the microstrip antenna.

3. Analysis of the Radiation Mode

Analysis of a rectangular patch microstrip antenna on a uniaxial anisotropic substrate can be carried out by a combination of the techniques for the case of an isotropic substrate [3,4] and the numerical technique of Kobayashi [5]. Analytical results support the basis of the present design approach; namely the anisotropy of the substrate does not substantially affect the

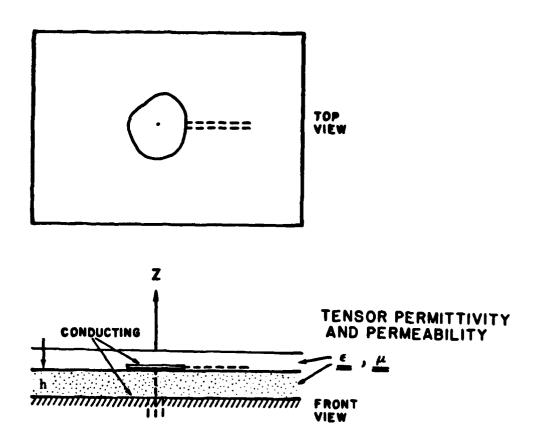


Figure 1. A microstrip antenna with exotic substrate and radome.

antenna characteristics. Of course, the greater the extent of anisotropy the larger the antenna properties deviate from the case of isotropic substrates.

Although not yet established experimentally, the effects of the anisotropy can probably be handled by using the concept of effective permittivity ϵ_e [6]. By doing so, we can use the familiar formula developed for isotropic substrates. For example, the resonant frequency can then be related to the patch parameters in the following equations

$$f_r = \frac{c}{2(L + 2 \Delta l) \sqrt{\epsilon_e}}$$
 (4)

where

$$\Delta \ell = 0.412 \frac{(\epsilon_e + 0.3)(W/h + 0.264)}{(\epsilon_e - 0.258)(W/h + 0.8)}$$
 (5)

c = velocity of light in free space,

and L, W and h are dimensions in meters as shown in Figures 1 and 2.

The only unknown in Equation (4) is ϵ_e , which can be solved numerically by computing the line capacitance C and noting that

$$\varepsilon_{\mathbf{e}} = \frac{\mathbf{c}}{\mathbf{c}_{\mathbf{o}}}$$
 (6)

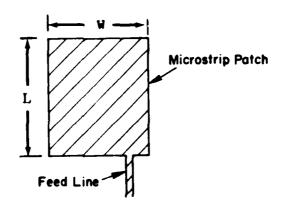


Figure 2. Dimensions of the rectangular patch of a microstrip antenna.

where C_0 is the well-known capacitance of the strip patch in the absence of the dielectric substrate; that is, when $\varepsilon = \varepsilon_0$.

The effect of substrate anisotropy can be evaluated by examining the capacitance per unit length for the case of a simple microstrip line. Table 1 shows a comparison of line capacitance per unit length, C/ε_0 , between isotropic and anisotropic substrates with the same ε_Z . The differences are small, no more than 5%. In fact, a considerable amount of these differences are due to computational errors inherent in each case (the anisotropic cases by Kobayashi [5], and isotropic cases by Wheeler's method [7]).

In order to reveal the extent of the effects due to substrate anisotropy, the strip line as shown in Figure 3 is examined by the method developed by Shibata, et al [8]. Some of the results are shown in Figures 4-7, in which C denotes the line capacitance per unit for the anisotropic substrate and Cl is the capacitance when $\epsilon_2 = \epsilon_1$, the case of isotropic substrate. The ratio C/Cl is plotted versus ϵ_2 for three normalized line widths (W/B) of 0.01, 0.1 and 1.0. As can be seen, the effect of substrate anisotropy is rather smooth and orderly and does not appear to present serious design difficulties.

It may be desirable to examine the situation when ϵ_2 is complex. However, there appears to be no reported study for microstrip problems of this nature, especially for the case of a large loss tangent.

Table 1. Comparison of C/c between isotropic and anisotropic substrates

.ε W/h	anisotropic $9.4 \hat{z} + 11.6 \hat{t}$	isotropic 9.4	anisotropic $11.6 \hat{z} + 9.4 \hat{t}$	isotropic 11.6
0.1	8.784	8.33	9.260	9.706
1.0	19.689	19.60	22.016	23.24
10.0	105.506	110.31	127.628	130.34

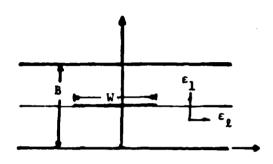
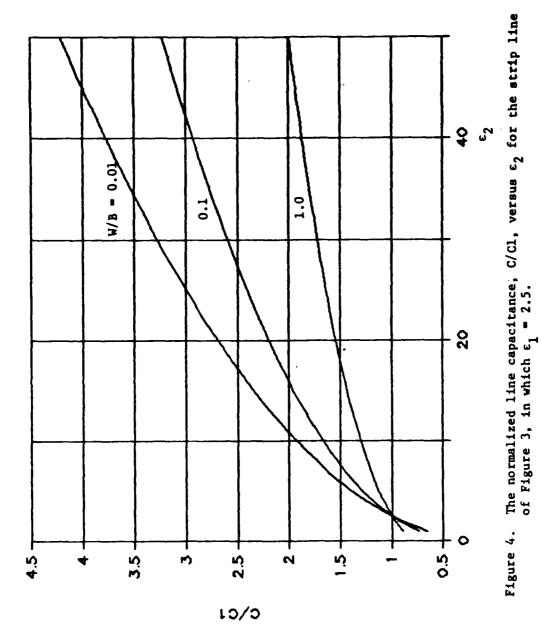
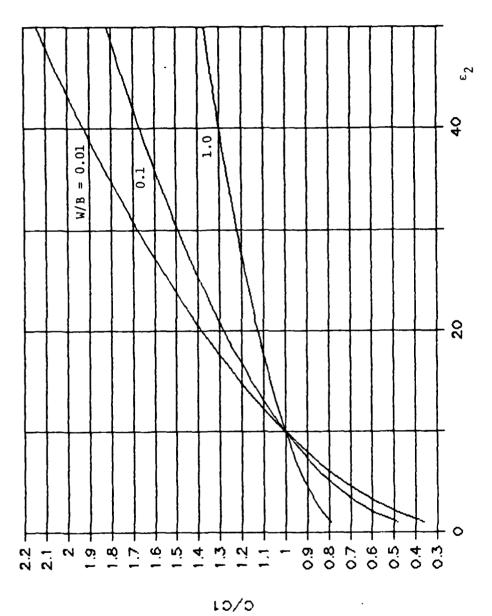
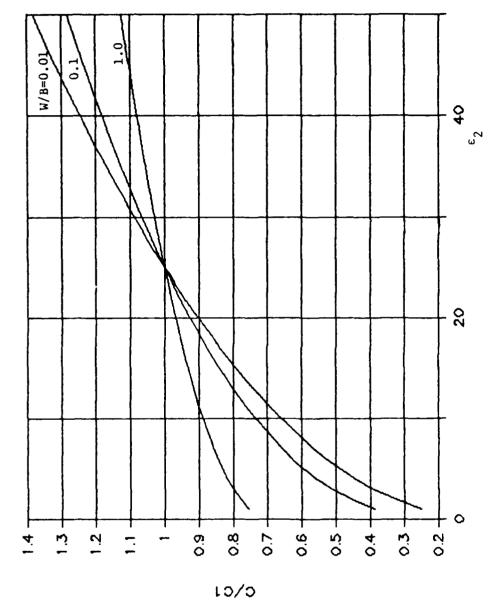


Figure 3. A strip line with anisotropic dielectric.

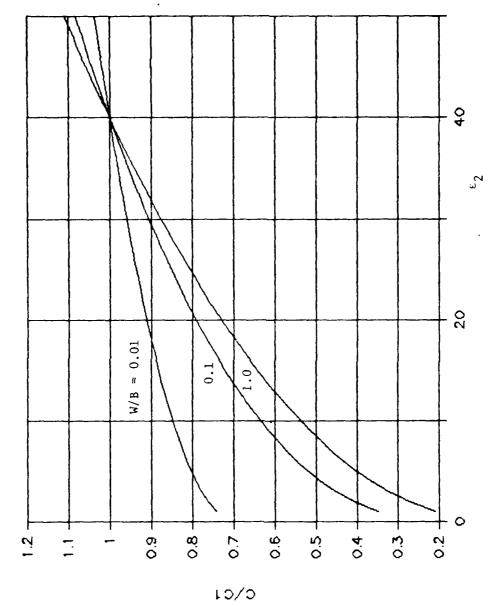




The normalized line capacitance, C/Cl, versus ϵ_2 for the strip line of Figure 3, in which ϵ_1 = 10. Figure 5.



The normalized line capacitance, C/Cl, versus ϵ_2 for the strip line of Figure 3, in which ϵ_1 = 25. Figure 6.



The normalized line capacitance, C/Cl, for the strip line of Figure 3, in which ϵ_1 = 40. Figure 7.

4. Analysis of the Scattering Mode

The scattering mode, in which the microstrip antenna is illuminated by an incident plane wave, can be computed with first-order accuracy by neglecting the presence of the microstrip patch and feed line. The problem is then reduced to the case of reflection from an anisotropic dielectric sheet on a conducting plane, for which direct solution for the half-space problem is available, and the edge effect can often be neglected.

5. Conclusions and Recommendations

We have demonstrated the potential usefulness of microstrip antennas with exotic substrates in applications to advanced aircraft. These exotic substrates are becoming more and more realistic as manufacturing technology progresses. Some experimental work is needed to guide the development of design and analysis techniques.

References

- Damaskos, N. J., Mack, R. B., Maffett, A. L., Parmon, W., and Uslenghi, P. L. E. (1984), The Inverse Problem for Biaxial Materials, IEEE Trans. Microw. Theo. Tech., 32 (No. 4), pp. 400-404.
- Das, S. N. and Chowdhury, S. K. (1982), Rectangular Microstrip Antenna on a Ferrite Substrate, <u>IEEE Trans. Ant. Prop.</u>, 30 (No. 3), pp. 499-502.
- 3. Lo, Y. T., Solomon, D., and Richards, W. F. (1979), Theory and Experiment on Microstrip Antennas, <u>IEEE Trans. Ant. Prop.</u>, 27 (No. 2), pp. 137-145.
- Carver, K. R. and Mink, J. W. (1981), Microstrip Antenna Technology, <u>IEEE Trans. Ant. Prop.</u>, 29 (No. 1), pp. 2-24.
- 5. Kobayashi, M. (1978), Analysis of the Microstrip and the Electro-optic Light Modulator, IEEE Trans. Microw. Theo. Tech., 26 (No. 2), pp. 119-126.
- 6. Schneider, M. V. (1969), Microstrip Lines for Microwave Integrated Circuits, <u>Bell Syst. Tech. J.</u>, 48, pp. 1421-1444.
- 7. Wheeler, H. A. (1977), Transmission-line Properties of a Strip on a Dielectric Sheet on a Plane, <u>IEEE Trans. Microw. Theo. Tech.</u>, 25 (8), pp. 631-647.
- 8. Shibata, H., Minakawa, S. and Terakado, R. (1982), Analysis of the Shielded-strip Transmission Line with an Anisotropic Medium, IEEE Trans. Microw. Theo. Tech., 30 (8), pp. 1264-1267.

A HIGH-EFFICIENCY, LOW-PHASE ERROR WAVEGUIDE LENS FOR A TRANSFORM FEED ANTENNA

Daniel T. McGrath
Electromagnetic Sciences Division
Rome Air Development Center
Hanscom AFB, MA 01731

ABSTRACT

A parallel-plate waveguide microwave lens, constructed as part of the concept development of completely overlapped subarray antennas, was modified and tested. The lens' function is comparable to that of a Rotman lens with 16 inputs (beam ports) and 60 outputs (antenna ports). However, the input face is linear with uniformly spaced monopole elements, and the output face is circular, with monopole elements spaced uniformly in angle.

Using a four-way power divider at the center four inputs and the outputs connected to a line-source array, low sidelobe patterns were measured over a 22% bandwidth. Over the same 8.0 to 10.0 GHz band, total power loss in the lens was less than 2.3 dB including mismatch, spillover and reflection losses.

Achieving those results required two major modifications to the antenna: First, although image theory predicts the phase center of a ground plane-backed monopole is at the ground-plane, measurements show that when placed in an array, the phase center is closer to the monopole. Its exact location depends on the element spacing in wavelengths, and will therefore change with frequency. The focal array was moved farther from the circular lens face to give good focusing at the center frequency. Second, the mismatch and coupling properties of unequally spaced elements along the circular face varied enough to distort the amplitude taper, causing higher sidelobes. An optimum uniform spacing eliminated that problem, and it is shown that it is possible, in general, to find such a spacing that will not degrade the len's performance either as a beamformer or as a transform feed.

1. INTRODUCTION

To verify the properties of transform feed antennas, Rome Air Development Center built an experimental model that uses a small Rotman lens to feed a large cylindrical lens. 1,2

Both of these lenses, shown in Fig. 1 are parallel plate waveguides with coaxial monopole elements. Poor initial

results were due to the characteristics of those elements in the array environment: the coupling properties of unequally spaced elements along the circular lens face varied enough to distort the amplitude taper; and their phase centers were not at the vertical waveguide wall as image theory suggests.

To correct for those effects we first found an optimum uniform spacing of elements that gave a good impedance match without appreciably degrading the lens' function as a space feed. Second, we moved the focal array back, away from the circular face, so that the probes themselves were in the "focal plane", rather than the wall (ground plane) behind them. With these modifications amplitude and phase errors were reduced to .5 dB and 5° r.m.s. Total power loss in the lens is less than 2.2 dB over a 20% bandwidth. When fed from a four-way power divider rather than the Rotman lens, the antenna produced low-sidelobe patterns over the same 8.0 to 10.0 GHz frequency range.

2. MODIFICATIONS

2.1 Uniform Element Spacing

In the original array lens design the 60 elements along the circular face were projected straight back from their corresponding aperture elements. Hence, the spacing between adjacent elements in the waveguide was $.5\lambda_0$ in the center but became progressively larger going toward the outside edges, where it was $.7\lambda_0$. Because each element "sees" a different array environment, the mutual coupling properties varied along the face and the result was the measured VSWRs shown in Fig. 2. With the higher mismatch loss in the center there was an "inverse taper" applied to the array. Fig. 3 is the measured pattern of a central

focal element, which ideally should be a "sinc" pattern with first sidelobes at -12.5 dB. The inverse taper accounts for the higher sidelobes while the filled-in nulls are the result of poor focusing.

Given any spacing of monopole elements in an array it is possible to find a probe length (1) and ground plane spacing (g) for a good match over a wide bandwidth. We could have chosen to match each element by allowing those parameters to vary along the curved lens face. But there is a phase delay between the fields in the coax and the propagating wave between the parallel plates which must depend on g and 2. The result of impedance matching in that manner would be to replace a varying insertion loss with a varying insertion phase, which is equally unacceptable in a lens.

For that reason we chose to modify the lens by spacing the probes of the circular array uniformly, thus guaranteeing that they would each see the same environment. That change introduces path length errors that might be intolerable in a wide-angle beamformer, but which do not seriously degrade this lens' function as a space feed. That function is to synthesize an amplitude taper and linear phase shift across the aperture. The amplitude taper creates a low-sidelobe pattern, while the linear phase shift corrects for the frequency-dependent squint of the phase-shifter-steered aperture array. An overlapped subarray antenna does that by amplitude-weighting and time-delay-phasing the beams of the transform feed (in this case the Rotman lens).

In a sense, the elements at the cylindrical face "sample" the field produced by the Rotman lens and apply it to the aperture with the interconnecting cables. Originally, that sampling was at equal intervals in sin 0, while we want to sample at equal intervals in 0, as shown in Figs. 4 a & b, respectively. The distortion thus introduced in the aperture amplitude and phase distributions is shown in Figs. 5 a & b. Amplitude distortion is of little concern since we could correct it by using different weights on the subarray beams. Conversely, the phase distortion amounts to a quadratic error across the aperture, which not only raises near-in sidelobes, but might introduce a squint by changing the average phase slope.

We want to choose a spacing of elements in θ that will minimize those effects. Letting $\Phi(x)$ and $\Phi'(x)$ be the original and the distorted phase distributions in the aperture (assumed continuous):

$$\Phi(\mathbf{x}) = \alpha \mathbf{x} \tag{1}$$

$$\Phi'(x) = \alpha F \sin [\delta x/d] \qquad (2)$$

where α is the constant phase slope, F is the radius of the lens face (i.e. the focal length), d is the distance between aperture elements and δ is the angular spacing (in degrees) of lens elements.

For there to be no squint, the average error between Φ and Φ' must be zero:

$$\overline{\varepsilon} = 0 = \alpha \int_{0}^{L} \left(x - F \sin \left[\delta x / d \right] \right) dx$$
 (3)

$$= \alpha \left[L^2/2 + dF/\delta \left(\cos \left[\delta L/d \right] - 1 \right) \right]$$
 (4)

which is true when $\delta=1.55^{\circ}$ for our parameters $d=.5\lambda_{\circ}$; $F=19.44\lambda_{\circ}$ and $L=15\lambda_{\circ}$. It is nearly the same value of δ that minimizes the total squared error over the aperture

$$\varepsilon_2 = \alpha^2 \int_0^L \left[\phi(x) - \phi'(x) \right]^2 dx \qquad (5)$$

and therefore was our choice for the new probe spacing.

Fig. 6a shows the measured VSWR of the 60 active, uniformly spaced elements of the circular lens face. All probes are the same length (.213 λ_0) and the same distance from the ground plane (.200 λ_0). Typical VSWR versus frequency is Fig. 6b.

2.2 Phase Center Correction

Fig. 7 shows the measured phase at the 60 ports of the cylindrical lens when a single port on the opposite side is driven, using a network analyzer. Since the excited port is near the lens' focal point, the measured phase should be almost linear, as shown by the solid line, which assumes that the probe appears to radiate from its projection onto the ground plane behind it. The data fits the dashed line better, which is the predicted phase assuming it radiates from its center conductor. This measurement indicates that the phase center of the monopole (i.e. that point from which it appears to radiate) is not at the

image plane, but is in fact closer to the monopole, which is due to mutual coupling with the other elements of its array.

We compensated for that effect by moving the linear array (connected to the Rotman lens) back away from the cylindrical lens face, so that its elements, rather than their ground plane, were in the "focal plane." This resulted in the improved phase response of Fig. 8 and the beam pattern of Fig. 9. Clearly, the center probes are almost perfectly focused at the center frequency. (Figs. 8 & 9 are for element 1-left of the small linear array.) At 8.0 GHz on the other hand, we measure the phase shown in Fig. 10. Again there is a quadratic error, but it is in the opposite direction of the error in Fig. 7, indicating that at that frequency the phase center is closer to ground. We have used these measurements, taken at several frequencies to compute the apparent phase center location and show the results in Fig. ll for the two probes nearest the focal point. (The horizontal axis of Fig. lla is scaled to the actual probe/waveguide geometry of Fig. 11b.) Since the spacing of these elements is .556 λ at 90 GHz, we conclude that when the spacing is near or less than $.5\lambda$, phase centers are at or near the ground plane, but move progressively closer to the monopole as frequency (and hence spacing in wavelengths) increases.

An explanation of this effect follows from Fig. 12, showing the computed element pattern phase from a moment method analysis by Tomasic³. There is a discontinuity near the end-fire grating lobe angle:

$$\theta_{EFGL} = \sin^{-1} \left[\lambda / d - 1 \right]$$
 (6)

For a fixed probe spacing, d, this discontinuity moves inward in angle as frequency increases. As it moves into the \pm 45° region subtended by our circular array, the effect is an apparent shift of the phase center.

3. MEASUREMENTS

3.1 Synthesized Low-Sidelobe Patterns

To test the array lens' ability to form low-sidelobe patterns, we disconnected the small linear array from the Rotman lens and connected a four-way power divider to its center four elements.

The outer two ports were weighted -10 dB relative to the inner two to produce the ideal, truncated Rotman lens outputs.

The measured phase and amplitudes at the circular array are shown in Figs. 13a & b, respectively, using the network analyzer transmitting into the power divider. The rms errors between the desired (solid lines) and the measured responses are 0.29 dB and 2.9° .

Measured H-plane patterns are Figs. 14, 15 and 16 at 8.0, 9.0 and 10.0 GHz, respectively. Low sidelobe (i.e. peak sidelobe below -30 dB relative to main beam) patterns were measured from 8.5 GHz to 10.0 GHz. Below 8.5 the peak sidelobe level goes slightly above -30 dB because of the defocusing due to phase center location error.

3.2 Instantaneous Bandwidth

Our primary goal in building this antenna was to demonstrate the wide signal bandwidth properties of completely overlapped subarrays as predicted by ${\rm Tang}^4$. To verify that the equal-angle lens element spacing does not affect the instantaneous bandwidth,

we connected the Rotman lens to the linear face of the array lens, and used phase-trimmed cables to steer the aperture to 550 from broadside. With appropriate time delays (again, trimmed cables) applied at the Rotman lens beam ports, there should be no squinting of the main beam as frequency changes.

In Fig. 17, the main beam was recorded at .25 GHz steps from 8.0 to 10.0 GHz, with the gain offset used to separate the traces. There appears to be a slight squint toward broadside at the highest frequencies, but that is due to the element pattern attenuating the side of the beam farthest from broadside more than the near side. (Without time-delay correction the beam would squint to 62.7° and 47.5° at 8.0 and 10.0GHz, respectively.) Based on Fig. 17 we conclude that the antenna has at least 22% signal bandwidth at 55° scan angle and that our recent modifications have not affected it in that regard. 3.3 Random Errors and Power Loss

array lens using the network analyzer. Transmitting into a single port of the small linear array we measured amplitude and phase at each port of the large circular array. The r.m.s. amplitude error is calculated as the deviation from a uniform illumination. The r.m.s. phase error is the deviation from a linear phase tilt. The power loss is calculated from the measured

We have measured the random errors and power losses in the

Figs. 18a & b show the r.m.s. amplitude and phase error, respectively, versus frequency. Because the element patterns were not accounted for in this analysis there is a gradual

insertion loss over the 60 active ports of the circular array.

rise in amplitude error at the higher frequencies due to the sharp pattern rolloff at the end-fire grating lobe angle. The phase error is typically around 50 r.m.s., but is greater at the lowest frequencies because of the quadratic error due to the change in phase center location.

Power loss in the lens as a function of frequency is shown in Fig. 18c. With a single port of the linear array transmitting, the total insertion loss is calculated from the measured insertion loss at each active port, n, of the

$$IL_{total} = 10 \log_{10} \sum_{n} 10^{-IL_{n}/10}$$
 (7)

Hence Fig. 18c. accounts for mismatch, spillover and conductor losses.

A good portion of that loss is due to the active reflection coefficient, Γ_a of the circular array. We have calculated $|\Gamma(0)|$, the coefficient for a broadside array, from reflection and coupling measurements (using coupling data from the nearest three probes on either side of the reference) as:

$$r = \frac{3}{100} s_{n=3} s_{on}$$
 (8)

Those points are shown in Fig. 19, along with two theoretical curves computed by a moment-method program by Boris Tomasic. The calculated curve using the actual parameters of probe length, ground plane spacing and inter-element spacing shows excellent agreement with the measurements. The second curve shows what is possible simply by using .025" longer probes, which would reduce the mismatch loss by about .6 dB at 8 GHz.

4. CONCLUSIONS

We have achieved low-sidelobe performance over a wide bandwidth with a parallel-plate waveguide lens antenna. major changes to its original design were necessary: First, we repositioned the beam port array to place the monopole elements' phase center in the lens focal plane. The exact location of that phase center depends on element spacing in wavelengths and thus varies with frequency. Second, we relocated the cylindrical array elements for uniform spacing and hence uniform low VSWR match and uniform mutual coupling. This change removed the "inverse taper" associated with the nonuniform spacing without altering the antenna's wide instantaneous bandwidth when fed with a time-delay steered Rotman lens. further improvements are possible by reducing the linear array spacing to avoid frequency-varying phase center location, and using longer probes to reduce the active array reflection coefficient.

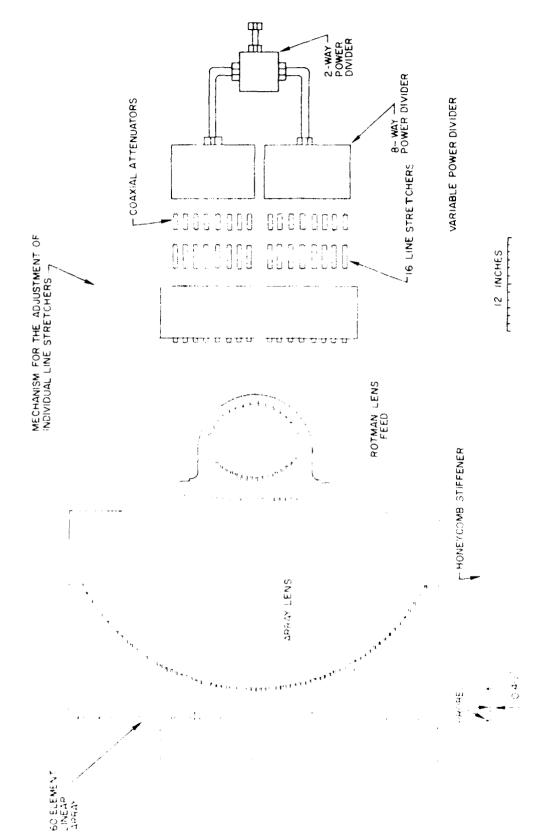
As a result of these experiments we conclude that low-loss, low-error lens antennas are possible using coaxial probes in parallel-plate waveguides. Although similar results have been reported using printed circuit lenses 5 the waveguide lens has the advantage of being able to handle high power.

References

- Fante, Ronald L., Systems Study of Overlapped, Subarrayed Scanning Antennas, 1979 Antenna Applications Symposium, Monticello. IL.
- 2. Southall, Hugh L., Completely-Overlapped-Subarray-Fed Antenna for Broadband, Wide Scan Angle, Low Sidelobe Radar Application, 1980 Antenna Applications Symposium, Monticello, IL.

- 3. Tomasic, Boris and Hessel, Alexander, Linear Phased Array of Coaxially-Fed Monopole Elements in a Parallel Plate Guide, 1982 APS Symposium Digest, pp. 144-147, Albuquerque, NM.
- 4. Tang, Raymond, Survey of Time-Delay Beam Steering Techniques in Phased Array Antennas, pg. 254, ed. Oliner and Knittel, Artech House, 1970.
- 5. Maybell, Michael J., Printed Rotman Lens-Fed Array Having Wide Bandwidth, Low Sidelobes, Constant Beamwidth and Synthesized Radiation Pattern, 1983 APS Symposium Digest, pp. 373-376, Houston, TX.

COMPLETELY OVERLAPPED SUBARRAY ANTENNA



ins the strong their werdayed Charray Antenna

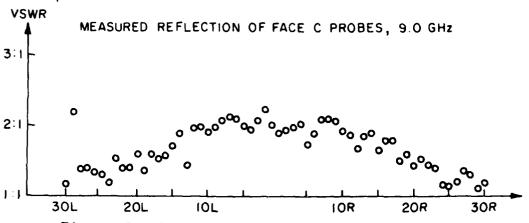


Figure 2. Measured VSWR of Nonuniformly Spaced Concave Circular Array Elements

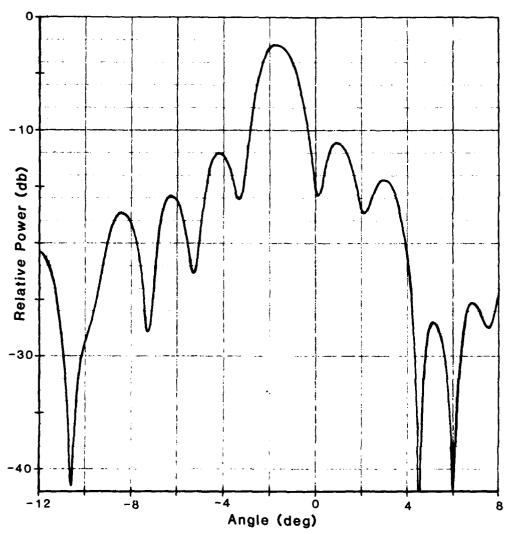
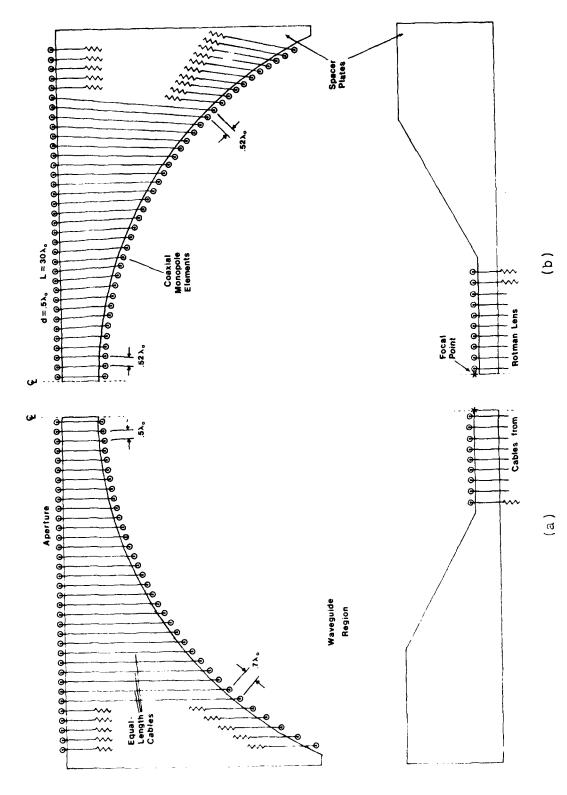


Figure 3. Pattern of Array Lens Beam Port 1L



Comparison of Original (a) and New (b) Array Lens Designs Figure

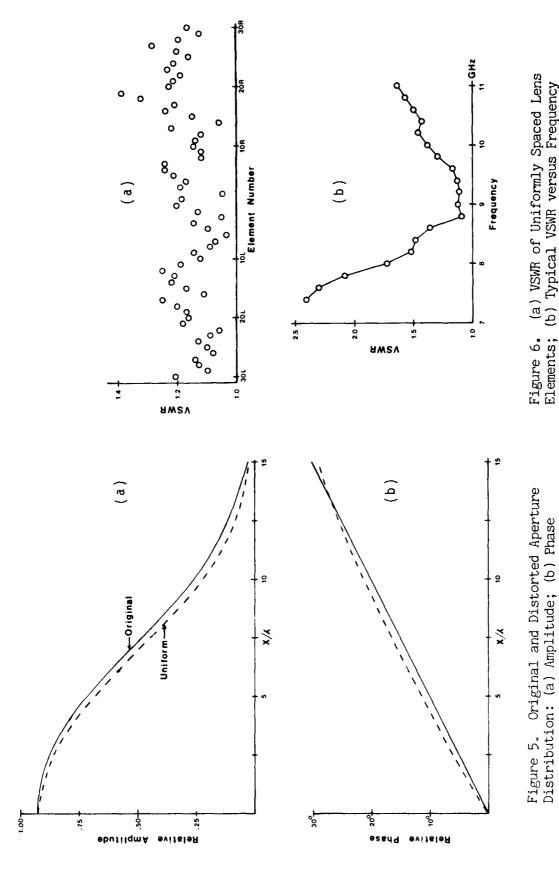
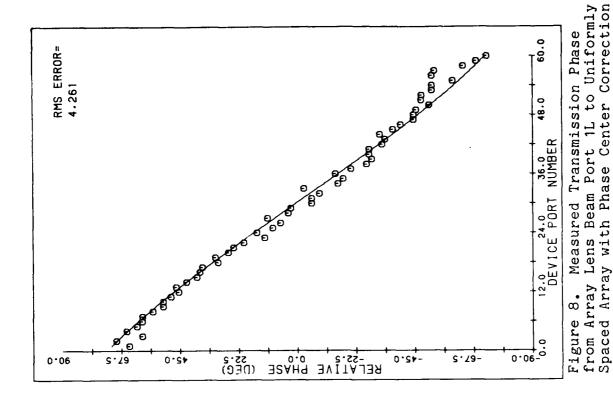


Figure 6. (a) VSWR of Uniformly Spaced Lens Elements; (b) Typical VSWR versus Frequency



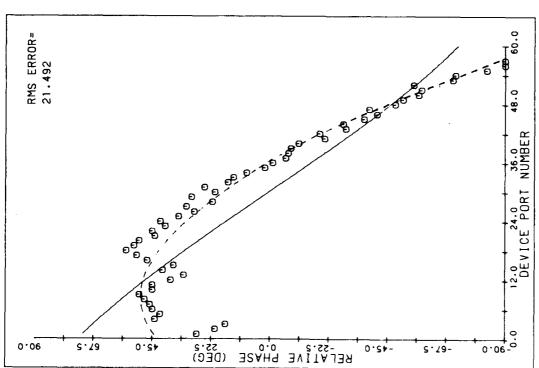
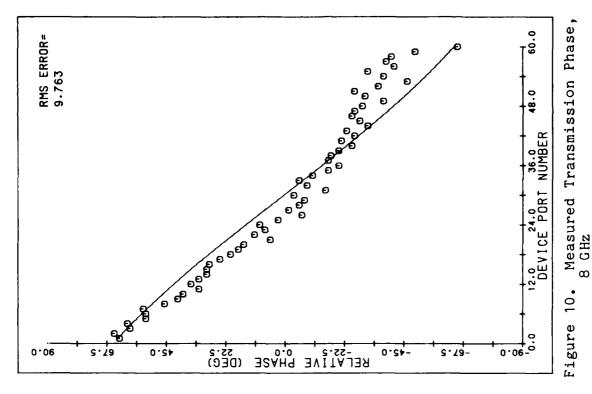


Figure 7. Measured Transmission Phase from Array Lens Beam Port 1L to Non-uniformly Spaced Circular Array, 9GHz



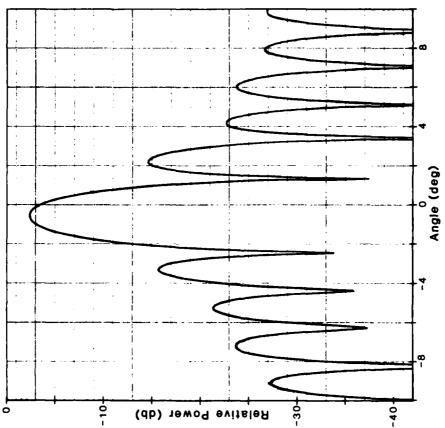


Figure 9. Measured Pattern of Array Lens Beam Port 1L After Modifications, 9GHz

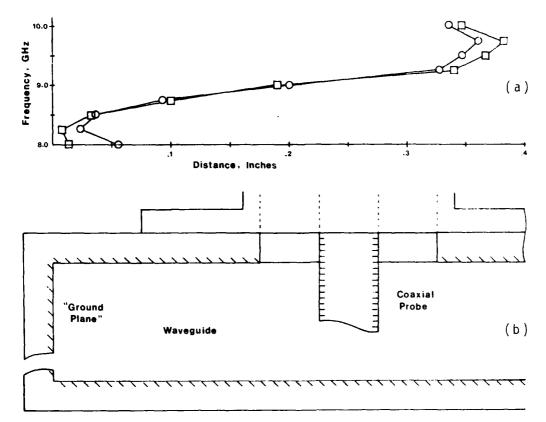


Figure 11. (a) Apparent Phase Center Location versus Frequency relative to (b) Probe/Waveguide Geometry

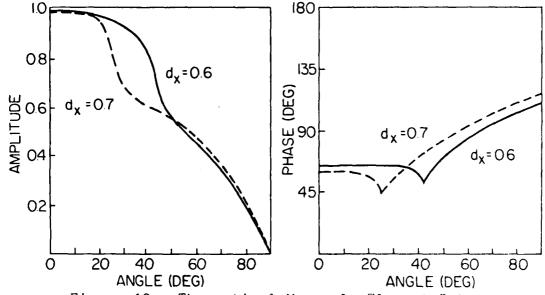
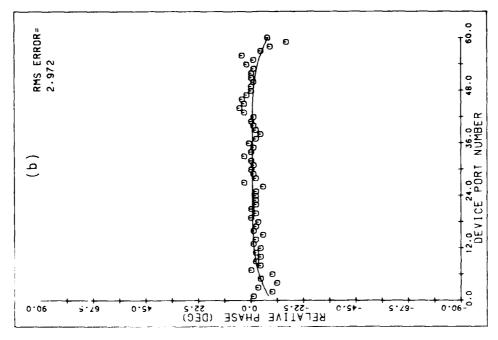
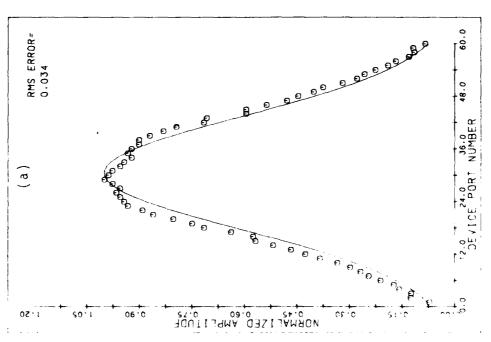
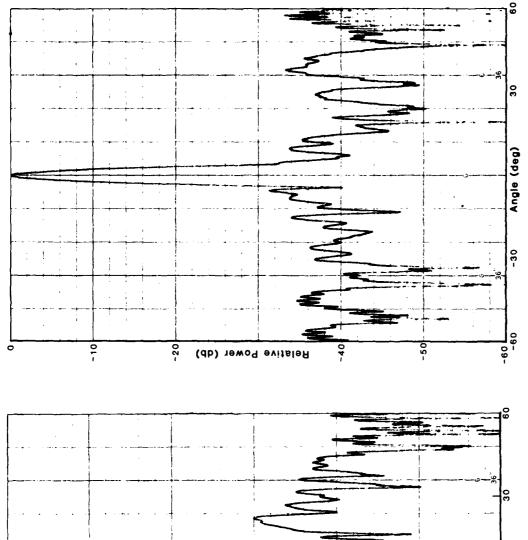


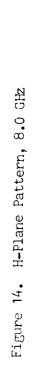
Figure 12. Theoretical Monopole Element Patterns (Tomasic and Hessel)

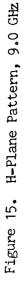




Measured Aperture Distribution with 4-Way Corporate Feed at 9.0 GHz: (a) Amplitude, (b) Phase







(db) 19woq evitsleA

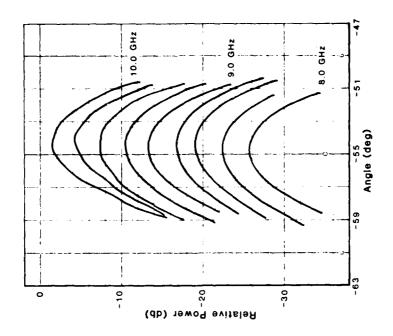


Figure 17. Position of Main Beam vs. Frequency with Main Beam Steered to 55°

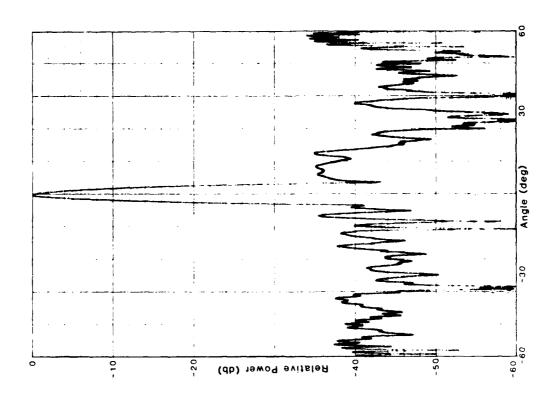
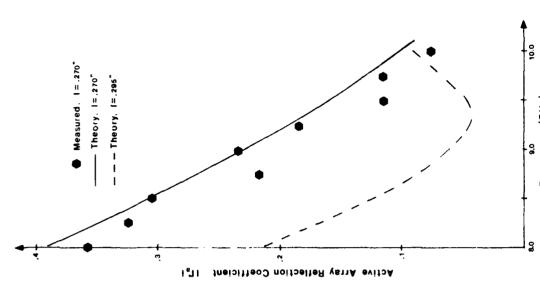
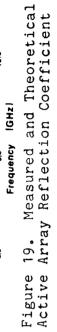


Figure 16. H-Plane Pattern, 10.0 GHz





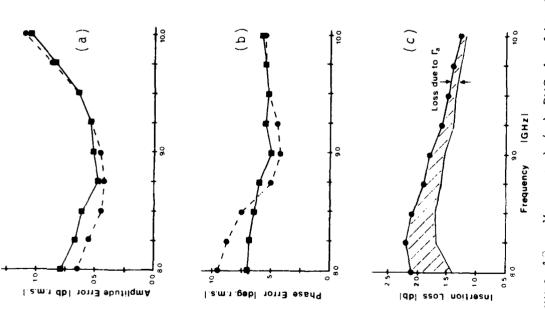


Figure 18. Measured (a) RMS Amplitude Error; (b) RMS Phase Error; and (c) Insertion Loss

Computer-Aided Bifocal Dielectric Lens Antenna Design for MM Wave Application

Sheng Y. Peng Teledyne Micronetics, San Diego, CA 92120

I. INTRODUCTION

A Bifocal Dielectric Lens Computer Model has been developed for the aid in the design analysis and performance evaluation for multiple-beam application. This type of lens antenna is very attractive at MM wave region where the feed network loss and size become problems. The model calculates and plots lens contour, the aperture distributions, and the corresponding radiation patterns and gain, with the feed located at any point on the focal arc.

Several different approaches in lens contour design were reported in the past. However an exact analytical solution is yet to come. Despite the lack of a closed-form solution, the "Ray Lattice" numerical method proposed by Holt and Mayer is very simple and attractive. The two surfaces of lens contour are determined through the ray path length constraints and Snell's refraction law. The design equations given in Holt's paper were partially in error and were rederived in this paper. Governing equations for computing the aperture phase distribution at each inter-beam location were also derived. Sample calculations for lens contour design, aperture phase distributions, and radiation patterns of 8-multiple beams at 94 GHz are included and discussed.

II. FORMULATION

A. Lens Contour Design Equations

There are several different approaches in lens contour design as reported in the past (1-3). In this paper, however, the computer model is based on a "Ray Lattice" method proposed by Holt and Mayer (3). Figure 1 shows a coordinate system for lens contour design formulation. The basic principle of the "Ray Lattice" method is using ray optics theory to determine lens surface contour through ray path length constraint and Snell's refraction law. outer and inner lens surfaces are determined by ray tracing the out-going and in-coming rays, alternately. The out-going rays are located at the upper half of the lens, while the in-coming rays are at the lower half of the lens, as shown in Figure 1. The first ray (out-going) starts from the lower focal point to the center of the lens' inner surface. After the corresponding point at the outer surface is determined, the location of the second ray (in-coming) at the outer surface is also determined through lens' symmetry property. After determining the locus point on the lens' inner surface for the second ray, the location at the inner surface of the third ray (out-going) is again determined, using lens' symmetry property. Repeating the above process, both inner and outer lens surfaces are obtained. It should be noted that each point on the lens surface is defined by (x, y, ψ) where ψ is the lens surface angle with respect to its surface normal (n). The ray directions are controlled

by angles α , β , and Θ_0 . The definition and signs of all these angles are defined in Figure 1.

Figure 2 defines lens parameters used in the formulation. For points on the inner surface, they are denoted by P_{2n} and \bar{P}_{2n} . While as on the outer surface, they are denoted by P_{2n+1} and \bar{P}_{2n+1} . In addition, the pairs (P_{2n}, \bar{P}_{2n}) and $(P_{2n+1}, \bar{P}_{2n+1})$ are points of symmetry with respect to lens axis (X-axis), and the bars represent the points on the lower half of the lens surfaces. Since lens design equations given in Holt's paper (3) are partially in error, the complete lens design equations are rederived and given in Table I.

B. Lens Aperture Relative Phase Distribution

In performing pattern analysis, the relative aperture phase distribution at any beam position has to be known. Figure 3 shows the ray geometry used in formulation for any beam position along a focal arc. The focal arc is defined here as an arc with its radius R centered at a point of (T_o, 0) as shown in the figure. It should be pointed out that the aperture relative phase distribution is determined from the difference between each ray path length and the reference path length of d_o which is defined in equation 3f in Table I. For two focal beams, all ray paths at the aperture are defined and are equal in length. The equations for calculating aperture phase error distribution were derived and are given in Table II. By definition, the phase error at these beam positions is zero.

TABLE I GOVERNING EQUATIONS FOR

A BIFOCAL DIELECTRIC LENS

I. Lens Bifocal Points:

$$X_{f} = -c \tag{1}$$

$$Y_{f} = + \sqrt{f^{2} \tan^{2} \theta_{o} + b^{2} \sin \theta_{o}}$$
 (2)

II. Out-going Rays:

$$x_1 = x_0 + \frac{c_1}{c_2} \tag{3}$$

$$c_1 = d_o + (c-f) \cos (c_o + X_o \cos_o + Y_o \sin c_o) - \sqrt{(X_o - X_f)^2 + (Y_o - Y_f)^2}$$
(3a)

$$c_2 = n_r \sec z_o - \cos z_o - \sin z_o \tan \beta_o \tag{3b}$$

$$F_0 = F_0 + \arcsin\left(\frac{\sin\left(\frac{1}{0} - \frac{1}{1} + 0\right)}{n_r}\right)$$
 (5c)

$$x_{o} = \arctan\left(\frac{Y_{o} - Y_{f}}{X_{o} - X_{f}}\right)$$
 (3d)

$$r_{ij} = 0 ag{5e}$$

$$d_0 = \sqrt{(a+b)^2 + f^2} + b \sin_0$$
 (3f)

$$Y_1 = Y_0 + (\lambda_1 - \lambda_0) \tan \lambda_0 \tag{4}$$

$$T_{1} = \arctan\left(\frac{n_{r}}{n_{r}}\frac{\sin r_{o} - \sin r_{o}}{\cos r_{o} - \cos r_{o}}\right) \tag{5}$$

$$\tilde{X}_{1} = X_{1}$$

$$\hat{Y}_{1} = \hat{Y}_{1}$$

III. In-coming Rays:
$$\bar{X}_2 = \bar{X}_1 + \frac{-D_2 + \sqrt{D_2 - D_1 \cdot D_3}}{D_1}$$
 (9)

$$D_{1} = (n_{r}^{2} - 1) \sec^{2} \bar{\beta}_{1}$$
 (9a)

$$D_2 = \left[d_0 - (c - f) \cos \theta_0 + \bar{X}_1 \cos \theta_0 + \hat{Y}_1 \sin \theta_0 \right]$$

$$n_r \sec \bar{b}_1 - (\bar{x}_1 - x_f) - (\bar{y}_1 - y_f) \tan \beta_1$$
 (9b)

$$D_3 = \left[d_o + (c + f) \cos \theta_o + \bar{\chi}_1 \cos \theta_o + \bar{\chi}_1 \sin \theta_o \right]^2$$

$$-(\bar{X}_{1} - X_{f})^{2} - (\bar{Y}_{1} + Y_{f})^{2}$$
 (9c)

$$\bar{Y}_2 = \bar{Y}_1 + (\bar{X}_2 - \bar{X}_1) \tan \bar{\beta}_1 \tag{10}$$

$$\bar{\beta}_1 = \bar{\psi}_1 + \arcsin\left(\frac{\sin\left(\frac{\Theta_0 - \bar{\psi}_1}{n_r}\right)}{n_r}\right)$$
 (11)

$$\bar{\psi}_2 = \arctan\left(\frac{n_r \sin \bar{\beta}_1 - \sin \bar{\alpha}_2}{n_r \cos \beta_1 - \cos \bar{\alpha}_2}\right)$$
 (12)

$$\tilde{u}_2 = \arctan\left(\frac{\bar{Y}_2 - Y_f}{\bar{X}_2 - X_f}\right) \tag{13}$$

$$\bar{x}_2 = \bar{x}_2 \tag{14}$$

$$Y_2 = -\overline{Y}_2$$

$$\Psi_{p} = -\tilde{\Psi}_{p}. \tag{16}$$

TABLE II EQUATIONS FOR CALCULATING RELATIVE APERTURE PHASE DISTRIBUTION

$$\phi_{K} = \frac{360}{\lambda} (\ell_{K} - d_{o}), \text{ in degrees}$$
 (1)

$$\ell_{K} = a_{1} + n_{r} a_{2} - a_{3}$$
 (2)

$$a_1 = \sqrt{(X_{2n} - X_f)^2 + (Y_{2n} - Y_f)^2}$$
 (3)

$$a_2 = \sqrt{(X_{2n+1} - X_{2n})^2 + (Y_{2n+1} - Y_{2n})^2}$$
 (4)

$$a_3 = (c-f) \cos \theta_0 + X_{2n+1} \cos \theta_0 + Y_{2n+1} \sin \theta_0$$
 (5)

$$S_{K} = \sqrt{X_{2n+1}^{2} + Y_{2n+1}^{2}} \quad \left[\sin (\psi_{2n+1} - \Theta_{0}) \right] - (c-f) \sin \Theta_{0}$$
 (6)

$$\psi_{2n+1} = \arctan\left(\frac{Y_{2n+1}}{X_{2n+1}}\right) \tag{7}$$

For any inter-beam positions, however, each ray intercepting point at the lens outer surface is unknown and needs to be determined, such as the point, P'_{2n+1} , as shown in Figure 3. Once the point, P'_{2n+1} , is determined, each ray path length is then defined. Therefore, equations listed in Table II can be used to calculate aperture phase error distribution for any inter-beam position, by substituting θ_0 , X_{2n+1} , Y_{2n+1} , X_f , Y_f , with θ_0 , X_{2n+1} , Y_{2n+1} , X_f , Y_f only.

In the determination of the point P'_{2n+1} location on the lens outer surface, a dual-slope technique is used. These slopes are the slope of the ray path within the lens (between the inner and outer surfaces) and the slope of a small section of lens outer surface (between two points of P'_{2n+1} and P'_{2n+1}) as shown in Figure 3. These slopes can be written as:

shown in Figure 3. These slopes can be written as:
$$m_1 = \frac{\frac{Y!}{2n+1} - \frac{Y}{2n}}{\frac{X!}{2n+1} - \frac{X}{2n}}$$
(1)

$$m_2 = \frac{Y_{2n+1}^{\dagger} - Y_{2n+1}}{X_{2n+1}^{\dagger} - X_{2n+1}}$$
 (2)

From equations 1 and 2, the point P_{2n+1}^{\prime} can be determined. Final equations for the determination of P_{2n+1}^{\prime} are given in Table III.

In summary, the design equations given in Tables I, II, and III provide the analysis tool to predict the designed lens performance. Although the equations are for designing a two-dimensional lens, they can be applied for designing a three-dimensional lens simply by using lens' symmetry property with its rotational axis (X-axis) as shown in Figure 3.

TABLE III EQUATIONS FOR CALCULATING LOCUS POINTS ON THE LENS OUTER SURFACE FOR

INTER-BEAM LOCATIONS

$$x'_{2n+1} = \frac{1}{m_1 - m_2} \left[(Y_{2n+1} - Y_{2n}) - (m_2 X_{2n+1} - m_1 X_{2n}) \right]$$
 (1)

$$Y'_{2n+1} = \frac{1}{m_1 - m_2} \left[(m_1 Y_{2n+1} - m_2 Y_{2n}) - m_1 m_2 (X_{2n+1} - X_{2n}) \right]$$
 (2)

$$m_1 = \tan \beta_{2n}$$
 (3)

$$\beta'_{2n} = \arcsin\left(\frac{\sin\frac{\alpha'_{2n}}{n_r}}{n_r}\right) + \psi_{2n}$$
 (4)

$$\alpha_{2n}' = \arctan\left(\frac{Y_{2n} - Y_{f}'}{X_{2n} - X_{f}}\right) - \psi_{2n}$$
 (5)

$$m_2 = \frac{Y_{2n-1} - Y_{2n+1}}{X_{2n-1} - X_{2n+1}} \tag{6}$$

$$X_{f}' = R \cos \theta_{o}' - T_{o}$$
 (7)

$$Y_{f}^{\prime} = -R \sin \theta_{o}^{\prime}$$
 (8)

$$R = \sqrt{(T_0 - X_f)^2 + Y_f^2}$$
 (9)

$$T_{o} = T/n_{r}$$
 (10)

III. NUMERICAL RESULTS

A. Lens Contour Design

A sample of computer-designed bifocal lens is shown in Figure 4. The value of input design parameters is also shown in the figure. These input parameters are defined in the following:

Freq = Frequency, in GHz

 Θ_{Max} (or Θ_{O}) = Bifocal beam angle, in degrees

- f = Distance between two parallel lines containing two
 focal points and two lens apices, respectively,
 (Figure 1), in inches
- c = Distance between the center of lens inner surface
 and a line containing two focal points, in inches
- b = Half size of lens aperture (Figure 1), in inches
- n_r =Dielectric lens refractive index

It should be noted that the frequency used in the calculation is 94 GHz, aimed for MM wave applications.

B. Aperture Relative Phase Distribution

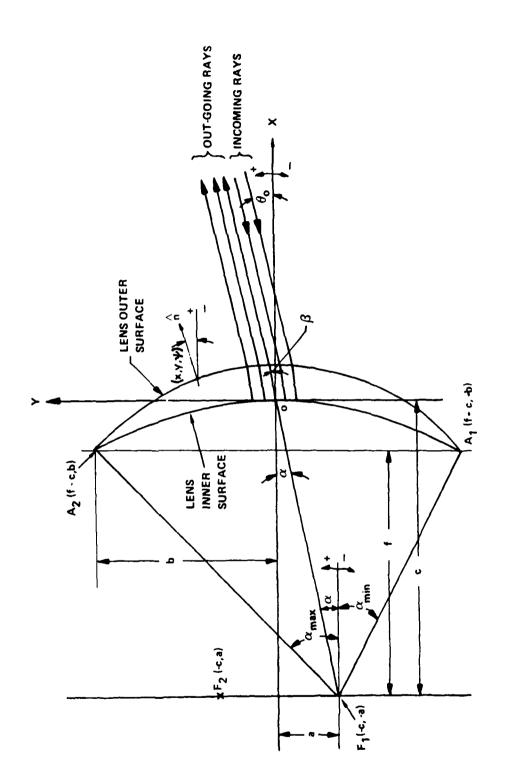
A sample of the computed aperture relative phase distribution is shown in Figure 5. There are eight inter-beam locations used in the calculation. Due to the lens symmetry, only four beams' aperture phase errors are shown in the figure. For focal beams, the phase error is zero. Note that the maximum phase errors are about 60 degrees.

C. Computed Radiation Patterns

Figure 6 shows a sample of the computed eight multiple beam patterns, using above aperture phase distributions and an assumed 12 dB edge taper of cosine type aperture relative amplitude distribution. The calculated beamwidth is ranging from 2.25 to 2.30 degrees, and the predicted directivity is ranging from 34.5 to 35.5 dBi.

IV. CONCLUSIONS

A computer-aided bifocal lens design model has been developed. The model designs and plots lens contour, calculates aperture relative phase distribution, and radiation patterns and gain for any given aperture amplitude distribution and beam position along a focal arc. The design parameters used in the numerical samples are for illustrative purposes only. This computer model provides a useful tool for design analysis of a bifocal lens for any suitable MM wave application, where the conventional phased array has potential weight, size, loss, and cost problems.



Lens Coordinate System and Geometry - Ray Lattice Method Figure 1

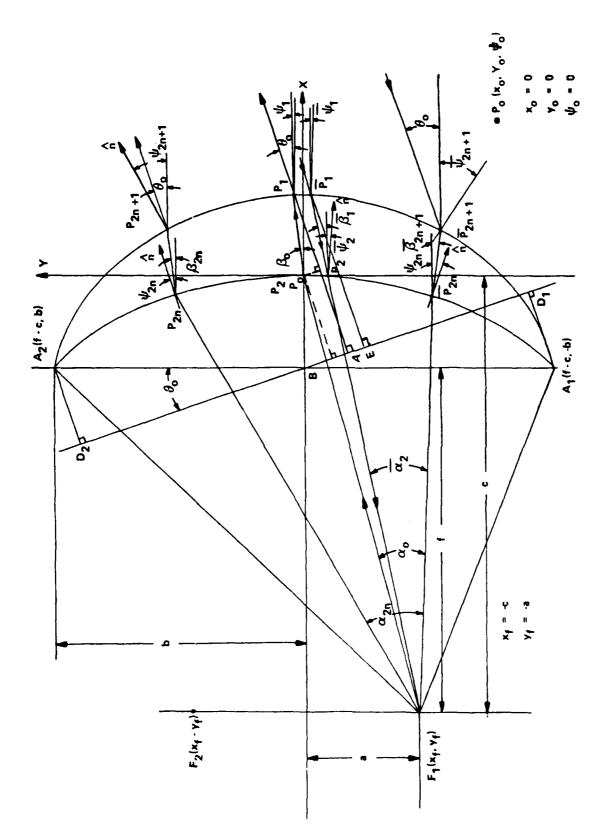
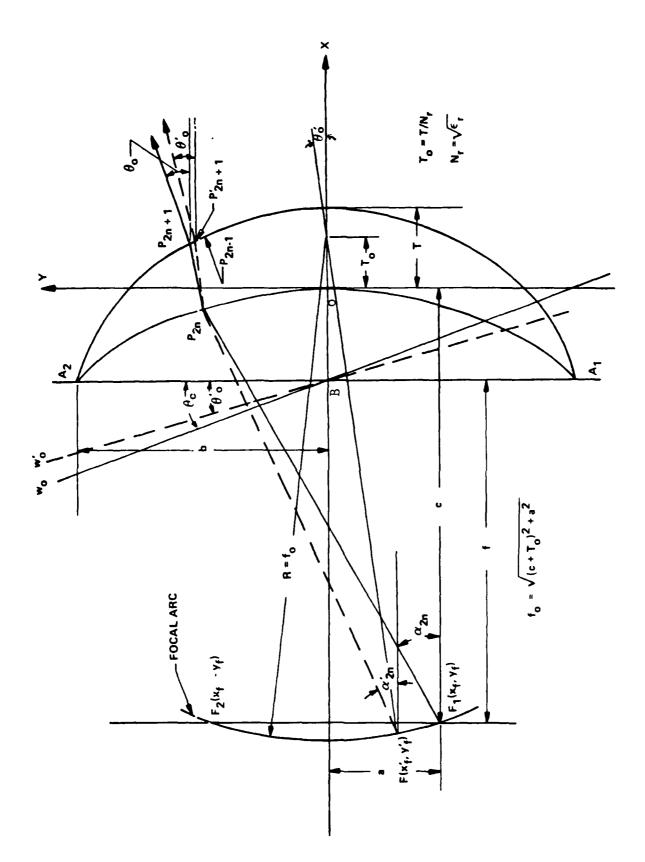
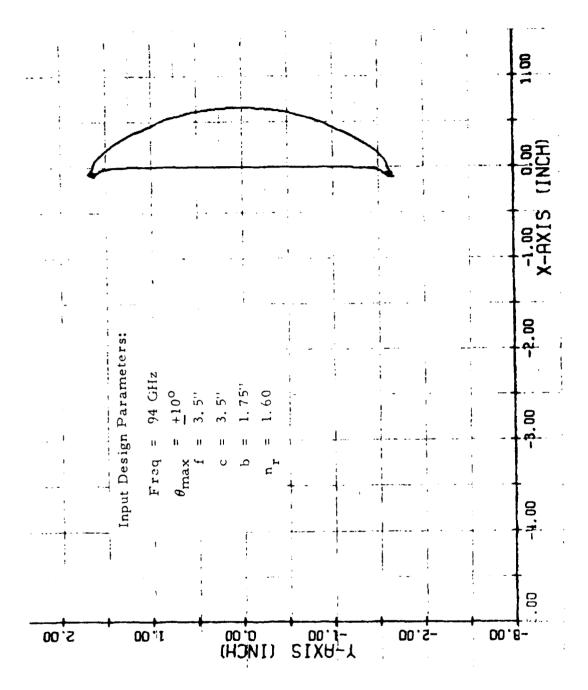


Figure 2 Designation of Lens Parameters Used in the Formulation

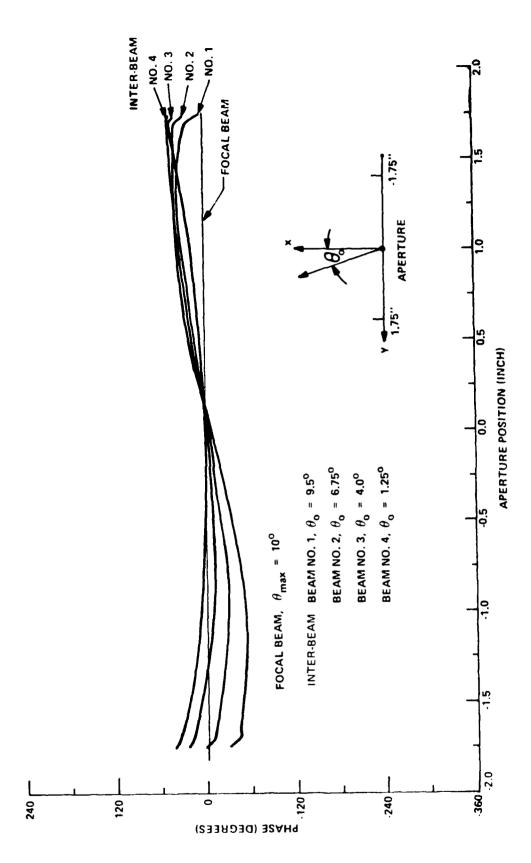


ŗ,

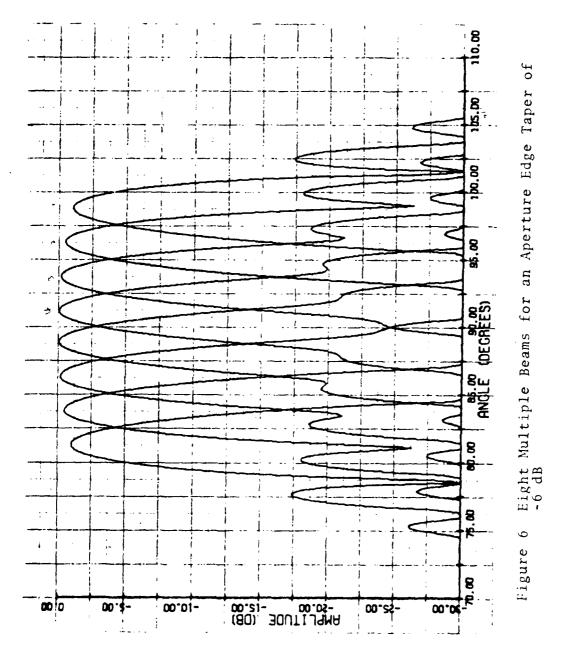
Geometry for the Determination of an Inter-Beam Aperture Phase Distribution 8 Figure



A Bifocal Dielectric Lens Designed by the Computer Model ($\epsilon_{\rm r}$ = 1.6) Figure 4



Relative Aperture Phase Distribution for Beam Angles, θ_0 = 9.5°, 6.75°, 4.0°, 1.25°, and $\theta_{max}=10^\circ$ at $f_r=94$ GHz Figure 5



ACKNOWLEDGMENTS

The author is grateful to Mr. Les Lemke, President, and Mr. Thomas Witkowski, Director of Engineering at Teledyne Micronetics, for their support and encouragement. Thanks are also due to Ms. Laura Peck for her help in preparing this paper.

REFERENCES

- Sternberg, R. L., "Successive Approximation and Expansion Methods in the Numerical Design of Microwave Dielectric Lenses," <u>J. of Math. and Phys.</u>, Vol. 34, pp. 209-235, Jan. 1956.
- 2. Brown, R. M., "Dielectric Bifocal Lenses," <u>IRE Convention</u>
 Record, pp. 180-187, March 1956.
- 3. Holt, F. S., and A. Mayer, "A Design Procedure for Dielectric Microwave Lenses of Large Aperture Ratio and Large Scanning Angle," <u>IRE Trans. on Antennas and Prop.</u>, pp. 23-30, Jan. 1957.

MISSION of Rome Air Development Center

HORLARUA CORLORCORLORCORLORCARCARCARCARCARCA

RADC plans and executes research, development, test and selected acquisition programs in support of Command, Control, Communications and Intelligence (C³I) activities. Technical and engineering support within areas of competence is provided to ESD Program Offices (POs) and other ESD elements to perform effective acquisition of C³I systems. The areas of technical competence include communications, command and control, battle management, information processing, surveillance sensors, intelligence data collection and handling, solid state sciences, electromagnetics, and propagation, and electronic, maintainability, and compatibility.

?&&C&GC&GC&GC&GC&GC&GC&GC

END

FILMED

5-85

DTIC